UNIVERSITÀ DI TRENTO

National PhD in Space Science and Technology

Ciclo / Cycle: 38th

Curriculum 6F

5G Satellite Transceiver Technologies for Non-Terrestrial Networks

Nome / Name: Francesco Cognome / Surname: Adamo

Supervisor/Tutor: Prof. Sergio Carrato

Co-supervisor/Co-tutor: Prof. Anna Gregorio, Ing. Mario Fraciacomo

Coordinatore / Coordinator: Prof. Roberto Battiston

ANNO ACCADEMICO / ACADEMIC YEAR 2024/2025

Finanziato dall'Unione europea NextGenerationEU | Ministero dell'Università e della Ricerca | Italiadomani | UNIVERSITÀ DI TRENTO

University of Trento

National PhD in Space Science and Technology

Cycle 38th

~ · ~

Operation Site

University of Trieste, Picosats s.r.l.

5G Satellite Transceiver Technologies for Non-Terrestrial Networks

Supervisor
Prof. Sergio Carrato

Co-Supervisors
Prof. Anna Gregorio
Ing. Mario Fragiacomo

Graduate Student
Francesco Adamo

Issued: October the 28th, 2025

Acknowledgments

This PhD activity was conducted in collaboration with the University of Trieste and Picosats, to whom special thanks are due. Regarding live in-orbit demonstration (LIDE) mission the author would like to thank European space agency (ESA) as the project founder; Tyvak International as the prime contractor and for the design of the hosting satellite platform; Rame S.r.l. for the ground segment design and the integration of 5G software radio stack in the system. This thesis was produced while attending the PhD program in Space Science and Technology at the University of Trento, Cycle XXXVIII, with the support of a scholarship co-financed by the Ministerial Decree no. 352 of 9th April 2022, based on the NRRP - funded by the European Union - NextGenerationEU - Mission 4 "Education and Research", Component 2 "From Research to Business", Investment 3.3 - CUP E63C22001350008, and by the company Picosats S.r.l.

Abstract

This work is carried out in the context of transceiver technologies for 5G non-terrestrial networks (NTN), with a focus on the live in-orbit demonstration (LIDE) mission and related activities spanning hardware design, system analysis, and testbed implementation. LIDE is a European space agency (ESA)-founded project which aims to validate a 5G-compliant link between a user equipment (UE) and 5G node B (gNB) on ground, through a transparent satellite payload in K/Ka band. After introducing the fundamentals of satellite communications and the 5G new radio (5G NR) protocol stack, the study addresses NTN-specific design challenges, including Doppler shift, latency, constrained terminal capabilities, and higher-layer issues such as hybrid automatic repeat request (HARQ) under long propagation delays. The research is focused on the development and validation of K/Ka-band transceivers, presenting in-orbit demonstrations (IODs) with transparent payloads. A commercial-off-the-shelf (COTS)-based upconverter architecture for low earth orbit (LEO) fixed-satellite service (FSS) applications was proposed, covering 17.3 GHz to 21.2 GHz with variable intermediate frequency (IF), and characterized in terms of spurious emissions, spurious-free dynamic range (SFDR), and error vector magnitude (EVM), achieving compliance with ITU recommendations. The payload design, integration with ground equipment, and qualification campaign are presented, along with 5G-specific testing in laboratory and in-orbit scenarios. The in-lab results confirm the feasibility of transparent payloads for NTN, with achieved data rates exceeding $1\,\mathrm{Mbit\,s^{-1}}$ uplink and $10\,\mathrm{Mbit\,s^{-1}}$ downlink at the user terminal. Two in-orbit demonstrations, by Picosats and the LIDE consortium, are presented. In the first IOD the transceiver capabilities are validated in orbit, showing also the transmission of a photo of the Earth taken from the relative satellite. LIDE IOD is presented as well; however, since the full ITU filing procedure was completed in September, only promising preliminary results are shown.

Contents

Acronyms

3GPP third generation partnership project. 1, 5, 11, 12, 22, 23, 28, 75

5G NR 5G new radio. 1, 5, 11, 12, 16, 19–21, 23, 25, 70, 71, 73, 74

5GC 5G core network. 12, 13, 15, 24, 75

ACI adjacent channel interference. 16

ADC analog-to-digital converter. 9, 10

AESA active electronically steerable antenna. 10, 11

AGC automatic gain control. 39, 66–68

AM acknowledged mode. 14

AMAM amplitude-to-amplitude distortion. 30–33

AMF access and mobility management function. 13, 15, 59

AMPM amplitude-to-phase distortion. 30

ARQ automatic repeat request. 13, 14

AWGN additive white gaussian noise. 31, 32, 36

BDC block down-converter. 28, 34, 35, 56, 58–61

BER bit error rate. 31–33

BF beam-forming. 10

BUC block up-converter. 28, 34, 35, 56, 59–61

CDF cumulative distribution function. 36, 37

CFO carrier frequency offset. 34–37, 41, 69

COTS commercial-off-the-shelf. 2, 3, 5–7, 73, 74

CP cyclic prefix. 16, 18

CSI channel state information. 19

CSI-RS channel state information reference signal. 19

CW continous wave. 2, 40, 48, 65, 66, 68, 69, 74

DAC digital-to-analog converter. 9, 10

DCI downlink control information. 18

DL downlink. 12

DM-RS demodulation reference signal. 19, 20

DN data network. 12, 13, 75

DRB data radio bearers. 14

ECI earth-centered inertial. 9

EIRP effective isotropic radiated power. 10, 24, 29

eMBB enhanced mobile broadband. 12

EQM engineering qualification model. 54, 56, 59

ESA European space agency. 1, 3, 5, 28, 74, 75

EVB evaluation board. 44–47

EVM error vector magnitude. 5, 46, 49, 50, 52, 70, 74

EVT environmental test campaign. 53–56

FBW fractional bandwidth. 8

FDD frequency division duplexing. 16, 28

FDL feeder downlink. 56, 58

FEC forward error correction. 13

FFT fast fourier transform. 16, 30, 31

FSS fixed-satellite service. 2, 5, 27, 46–48, 53, 73

FUL feeder uplink. 56, 57

GEO geostationary orbit. 6, 22, 24

gNB 5G node B. 1, 5, 12, 13, 15, 18–25, 28, 29, 34–36, 56, 57, 59–62, 73, 75

gNB-CU gNB - centralized unit. 12, 23

gNB-DU gNB - distributed unit. 12, 23

GNSS global navigation satellite system. 6, 24, 75

GPS global positioning system. 6

GSM global system for mobile communications 2G. 5, 11

GW gateway. 28, 29, 56, 58, 70, 75

HARQ hybrid automatic repeat request. 5, 13, 24, 25, 73

I/Q in-phase/quadrature. 46

ICI inter-carrier interference. 34, 36

IF intermediate frequency. 2, 5, 9, 10, 29, 39, 40, 42, 43, 45–49, 51, 52, 73, 74

IFFT inverse fast fourier transform. 16, 30

IOD in-orbit demonstration. 1, 2, 5, 27, 29, 30, 39, 40, 42, 53, 65, 67, 68, 73–75

IRM image rejection mixer. 47

ISI inter-symbol interference. 16

ISL inter satellite link. 22, 39

LEO low earth orbit. 1, 2, 5, 6, 22–25, 46, 65, 73, 74

LHCP left-hand circular polarization. 40

LIDE live in-orbit demonstration. 1–3, 5, 27–29, 31, 34, 35, 40, 41, 53, 54, 56, 59, 64, 65, 69, 70, 73–75

LNA low-noise amplifier. 9, 40, 42–44

LO local oscillator. 9, 34, 43, 46–49, 51, 73

LSB lower side-band. 46, 47, 49–51, 73

LTE long term evolution. 5, 11, 15

MAC medium access control. 13–15, 18, 19, 61

MEO medium earth orbit. 6, 22

MIB master information block. 20

mIoT massive internet of things. 12

NAS non access stratum. 15

NF noise figure. 9

NFV network function virtualization. 12

NG-RAN new generation - radio access network. 12, 13, 23

NTN non-terrestrial networks. 1–3, 5, 11, 17, 22–24, 26, 28, 53, 56, 59, 60, 64, 73–75

NTP network time protocol. 59

OBC on-board computer. 39–41, 59, 65, 66

OBO output back-off. 30, 32, 33, 50

OFDMA orthogonal frequency-division multiple access. 16, 17, 27, 30, 31, 33, 34, 36, 37

OMT orthogonal mode transducer. 40

OSI open systems interconnection protocols. 15

PA power amplifier. 10, 33, 46, 49, 50, 52, 57

PAPR peak-to-average power ratio. 30, 61, 73

PBCH physical broadcast channel. 18, 20

PCB printed circuit board. 42–45, 73

PDCCH primary downlink control channel. 18, 19

PDCP packet data convergence protocol. 14, 15

PDSCH primary downlink shared channel. 18–21

PFM proto flight model. 54

PHY physical layer. 13–16, 18

PLL phase-locked loop. 9, 34, 43, 45, 47, 49, 51, 73

PRACH physical random access channel. 19, 20, 22, 35–37, 75

PRB physical resource block. 17

PRS positioning reference signal. 19

PSS primary synchronization signal. 19, 20

PT-RS phase-tracking reference signal. 19

PUCCH primary uplink control channel. 19, 21

PUSCH primary uplink shared channel. 18, 19, 21

QoS quality of service. 15

QPSK quadrature phase shift keying. 18

RACH random access channel. 19, 20, 22, 35, 61

RAR random access response. 21, 22, 24, 61

RF radio frequency. 2, 9, 10, 34, 40, 41, 43–50, 52, 67, 73, 74

RHCP right-hand circular polarization. 40

RLC radio link control. 14, 15, 18

RRC radio resource control. 15, 20, 21, 24

RTT round-trip time. 24, 25, 61, 62

SATCOM satellite communication. 1, 5, 7, 8, 74

SCS subcarrier spacing. 16–18, 20, 23, 24, 28, 36, 37

SDAP service data adaptation protocol. 15

SDL service downlink. 56, 58

SDN software-defined networking. 12, 26

SDR software defined radio. 25, 28, 29, 34, 35, 56–61

SER symbol error rate. 31

SFDR spurious-free dynamic range. 2, 5, 46–51, 73, 74

SIB system information block. 18, 20, 23

SINR signal-to-noise-plus-interference ratio. 36, 37

SNR signal-to-noise ratio. 9, 24, 29, 30, 33, 56–58, 61, 68

SPDT single-pole-double-throw. 47

SPM spare model. 54

SRB signalling radio bearers. 14

SRS sounding reference signal. 19, 21

SSB synchronization signal block. 19–21

SSPA solid-state power amplifier. 10, 29, 30, 40, 75

SSS secondary synchronization signal. 19, 20

SUL service uplink. 56, 57

TA timing advance. 21, 22, 24, 62

TCXO temperature-compensated crystal oscillator. 9, 34, 40

TDD time division duplexing. 16, 18

TLE two-line element. 9, 60–64, 69, 75

TM transparent mode. 14

TRL technology readiness level. 1, 27

TT&C telemetry and command. 65, 66

TVAC thermo-vacuum chamber. 54

UCI uplink control information. 19

UE user equipment. 1, 2, 5, 12, 13, 15, 18–25, 28, 29, 34, 35, 56–62, 70, 73–75

UL uplink. 12

UM unacknowledged mode. 14

UMTS universal mobile telecommunications system. 5, 11

UPF user plane function. 13, 15, 59, 61

USB upper side-band. 46, 47, 49–51, 59, 60, 73

USRP universal software radio peripheral. 60

VoIP voice-over-ip. 26

VSAT very small aperture terminal. 22

Introduction

The satellite communication (SATCOM) industry has been rapidly evolving in recent years. 5G new radio (5G NR) is emerging as a promising common platform for the terrestrial and non-terrestrial network infrastructures. The European space agency (ESA) IRIS2 mission has adopted 5G as the baseline protocol for the new low earth orbit (LEO) telecommunication constellation. This PhD activity is carried out within this context, focusing on the challenges of 5G non-terrestrial networks (NTN) at physical layer and on satellite telecommunication payload design. Picosats srl, spin-off of University of Trieste, is the main operational site of the PhD. The scenario of the research activity is the live in-orbit demonstration (LIDE) mission, funded by ESA, with Tyvak International as prime contractor and Picosats srl as the provider of a 5G K/Ka band satellite communication payload. The work presented is oriented towards solutions at high technology readiness level (TRL), up to TRL 8–9, including the analysis of in-orbit demonstrations (IODs).

The main objective of the PhD activity is the study of 5G NTN challenges and solutions at physical layer, oriented to the design of satellite transceivers in the context of the NTN mission. 5G NR is standardized by the third generation partnership project (3GPP) consortium. The enhancements proposed by 3GPP in Release 17 have enabled the evolution of NTN. The integration of the terrestrial ecosystem with satellites has always been of interest, but only recently it has been reflected into 3GPP technical specifications. Typical 5G NTN use cases include coverage of under-served and rural areas, disaster communications in case of land communication damages, and broadcasting over large areas. The main system blocks of a 5G NTN are one or more user equipment (UE), a 5G node B (gNB) acting as interface between UE and data network, and a space platform. The satellite platform can integrate a transparent payload performing frequency conversion, filtering and signal amplification. If the payload integrates higher layers functionalities, it can be considered as a regenerative payload.

The main challenges of 5G NTN are well known in the literature. However, testbeds or in-orbit demonstrations integrating the 3GPP protocol adaptations for NTN are still quite few and recent to the date of this report. Frequency and time alignment are critical in 5G. Frequency shift due to Doppler effect and time delay variation induced by satellite movement can impact significantly 5G link performance. Compared to a terrestrial application,

radio link distances are much greater, resulting in higher free space attenuation. Furthermore, satellite antennas and transmitters, as well as UEs radio capabilities, are typically constrained, making the scenario even more challenging. Much of this work focuses on the design of satellite transceivers. During the time at Picosats, several projects were dedicated to developing K/Ka-band transceivers, resulting in three design iterations carried out over the course of the PhD. Each iteration addressed a different use case, requiring specific modifications that ultimately led to a new version of the design. The three relative projects, in chronological order, are the IOD of a K/Ka band transponder and horn antenna, the 5G LIDE mission, and the design of an improved version of the 5G transceiver for covering the complete K/Ka band fixed-satellite service (FSS).

During the first months of the PhD, the main outcomes were connected to the previous work carried out in Picosats. In that period, a Ku band version of the transponder reached the testing phase, leading to the publication [1]. This paper presented a new way to create a continous wave (CW) beacon signal using a conventional super-heterodyne transponder architecture. The IOD of a K/Ka band transponder and a dual-band horn antenna was presented in [2]. In the test results, primary bent-pipe transponder functionality was successfully validated, along with other minor tests. As a final test, two images of Earth were captured and successfully transmitted in multiple packets over several satellite passes, with one image clearly depicting Italy.

The LIDE mission description was presented in [3], demonstrating the feasibility of providing direct 5G broadband access from LEO satellites to small terminals. The satellite payload designed in Picosats, on the other hand, was described in [4]. This work presented key performance metrics and the payload qualification campaign. The results confirm that the system is in line with the scenario even after qualification. Its compatibility with a 5G environment was further validated through a dedicated testbed, which incorporated channel emulators to simulate satellite impairments.

After the LIDE payload design, the improved transponder transmitter was proposed in [5]. The system can cover the 17.3 GHz to 21.2 GHz FSS radio frequency (RF) bandwidth with a variable intermediate frequency (IF) frequency from 2.5 GHz to 4.0 GHz. Combined frequency conversion modes are used to achieve a state-of-art spurious-free dynamic range (SFDR) across the wide RF-IF bandwidth.

The work presented in this thesis aims to answer the following questions, by describiong the work carried out in Picosats: is it feasable to integrate commercial-off-the-shelf (COTS) devices in a complex satellite communication payload in Ka band? In the context of 5G NTN can the above mentioned systems be compliant with 5G frequency, timing constraints and other challenges regarding the integration of 5G in a satellite network? What are the main focus points to be considered in the design and testing of a system to be integrated in a 5G NTN mission? In the following, these questions will be answered as far as the author could during the PhD activity conducted from 2022 to 2025 in Picosats and University of

Trieste.

The work presented in this thesis aims to answer some research questions regarding the evolution of satellite transceivers. The presented study investigates: is it feasible to integrate COTS devices into complex satellite communication payloads operating in the Ka-band? Furthermore, in the context of 5G NTN, can these systems be fully compliant with 5G frequency and timing constraints, as well as all the other challenges of integrating 5G into a satellite network? Finally, what are the primary design guidelines to consider for a system intended for a 5G NTN mission? In the following chapters, these questions are addressed through the analysis and results obtained during the PhD activity conducted from 2022 to 2025 at Picosats and the University of Trieste.

Chapter 1

State of art on 5G NTN

In this chapter, the state of the art for 5G new radio (5G NR) in the context of non-terrestrial networks (NTN) is presented. The current satellite communication (SATCOM) scenario is first described, with a focus on satellite telecommunication payloads. Then, the third generation partnership project (3GPP) 5G standardization path is discussed, along with the main protocol features; particularly the physical layer and the challenges and solutions related to 5G NTN will be addressed. The enhancements proposed by 3GPP in Release 17 enabled the evolution of NTN, increasing the interest for 5G SATCOM. The internet connectivity environment has been dominated by the 3GPP solutions for many years, in the evolution path from universal mobile telecommunications system (UMTS) passing through global system for mobile communications 2G (GSM), long term evolution (LTE) to the actual 5G NR. In this path, the integration of the ground ecosystem with satellites has always been of interest, but did not reflect into 3GPP technical specifications like nowadays. Typical 5G NTN use cases are the coverage of under-served and rural areas, disaster communications in case of land communication damages and broadcasting over large areas. Another key aspect in assessing the feasibility of a 5G infrastructure is laboratory testing. A review of the state of the art in 5G NR testing is also provided.

1.1 Satellite telecommunications

The SATCOM industry has been rapidly evolving in the recent years. The four SATCOM market areas drivers are: *consumer* such as home internet users or private maritime users; *enterprise* such as industries that need satellite-to-ground communication or for data centres infrastructures; *government* in aviation, ground, maritime for civilian or military purposes; and *commercial mobility*, which involves companies which business is aerial, ground or maritime transportation.

The presented work mostly refers to the satellite environment in the proximity of Earth,

Orbit	Range	Coverage	Satellite passage	Antenna speed
LEO	500 - 1200 km	Narrow	10 minutes	Fast
MEO	5000 - 20000 km	Large	1 hour	Slow
GEO	36000 km	Largest	/	Stationary

Table 1.1: High-level comparison of the three main satellite orbit classes.

System	Kuiper	OneWeb	Starlink	Telsat
Band	Ka	Ku	Ku	Ka
Satellites (in orbit)	2	660	8050	0
Satellites (planned)	3232	7088	20 000	300
Altitude (km)	590 to 630	1200	540 to 570	1015 to 1320
Latency (ms)	∼30	∼40	∼30	∼40 to 50
Satellite life (years)	7	∼5	5 to 7	10 to 12
Constellation capacity at Full Plan	30 to 32	∼50	∼75	∼12

Table 1.2: Main telecommunication constellation in orbit [7].

which is the most crowded area since the beginning of human space exploration [6]. In this context three main areas are populated by satellites: low earth orbit (LEO), medium earth orbit (MEO) and geostationary orbit (GEO), ordered by increasing altitude. A general summary of their characteristics is reported in Table 1.1.

The boundaries between these three orbit classes are the Van-Hallen belts, which are zones of charged particle trapped by Earth magnetic field, that create a harsh environment for satellites transiting through those regions. MEO hosts a considering amount of satellites. All global navigation satellite system (GNSS) missions such as global positioning system (GPS), Galileo, Glonas and Beidou are placed in this orbit. On the other hand, GEO is a special orbit for which the satellite orbit time is equal to one Earth day. For this reason, GEO satellites appear stationary in the sky and are suitable for fixed terminals and for fixed areas of coverage, such as television broadcasting. The higher the altitude, the widest the coverage at ground. MEO constellations requires less satellites compared to LEO, for which thousands are needed to get a full global coverage. LEO ground terminals requires the highest scan speed to follow the satellite, and may need to perform handover between multiple satellites as a consequence of the short visibility time in a passage. However, due to the proximity to Earth, the majority of orbiting objects are at LEO orbit and are related to telecommunication purposes [6]. A summary of the main telecommunication constellations is listed in Table 1.2.

In the last decade the cost-per-mass of a space mission deployment has decreased significantly, enabled by the introduction of reusable launchers. Above all, SpaceX Falcon 9 has imposed itself as the leader of reusable rockets, with more than 400 successful completed missions, landings and booster reflights [8]. In the same scenario, the project management of space missions has changed. The use of commercial-off-the-shelf (COTS) components has

become common practice. These are ready-made components available in the market (in some cases not even designed for space), used for space applications. On the other hand, the use of custom designed components relates now only to large missions that requires a long life, e.g. deep-space scientific missions. This last approach is significantly more costly and requires much time to get to the final flight model [9]. It is therefore mainly adopted in the context of space agencies or army. The adoption of COTS comes after system analysis, for which it can be stated that the integration of a ready-made component is suitable in terms of cost and reliability for the system in which it has to be integrated. For instance, a component placed inside a satellite platform, which has in many cases a temperature control system, does not have to withstand the external space environment. Some components designed for automotive may be tested in a suitable temperature range. Furthermore, missions that do not require long durations and involve a constellation of a large number of satellite can withstand the failure of some nodes and still be fully operative. In literature, many examples of COTS solutions can be found also for 5G SATCOM applications, even at millimeter waves [10].

1.1.1 Radio frequency channel

The design of a satellite communication system has to cope with many factors that are related to the characteristics of the propagation channel. The first, inevitable, drawback of a wireless link is the free-space path loss L_{FS}. Assuming a receiver and a transmitter placed at distance d (in the far-field region of their antennas) the received power P_{RX} decreases with the square of the distance. The whole concept is reported with the Friis formula, shown in (1.1) and (1.2), where the receiver and transmitter antenna isotropic gains are G_{RX} and G_{TX}, the transmitted power is P_{TX}, L_{atm} is the atmospheric power loss, c the speed of light and f the transmitted signal frequency [11].

$$P_{RX} = \frac{P_{TX} G_{TX} G_{RX}}{L_{FS} L_{atm}} \tag{1.1}$$

$$L_{FS} = \left(\frac{4\pi f d^2}{c} \right)^2 \tag{1.2}$$

Losses depend on frequency. L_{FS} increases with the square of f. This can suggest that moving towards higher frequencies is unnecessary, but the actual trend reveals the opposite. The main aspects to be considered are the gain, dimensions of antenna and the available signal bandwidth. The antenna reciprocity formula shown in (1.3) explains the first point well. $A_{eff} = \eta A$ is the effective aperture of the antenna, related to the aperture efficiency η and the physical area of the aperture A.

$$A_{eff} = \frac{\lambda^2}{4\pi} G \tag{1.3}$$

Band	Uplink (GHz)	Downlink (GHz)
L	1.535 - 1.560	1.635 - 1.660
S	2.500 - 2.540	2.650 - 2.690
C	3.400 - 4.200	5.800 - 6.725
X	7.25 - 7.75	7.90 - 8.40
Ku	10.0 - 13.0	14.0 - 18.0
Ka	17.7 - 21.2	27.5 - 31.0
Q/V	37.5 - 42.5	42.5 - 51.4
E	71.0 - 76.0	81.0 - 86.0

Table 1.3: SATCOM frequency bands [12].

By keeping the same physical aperture, the gain increases with the square of the frequency. With this aspect, by shifting towards higher frequency bands, part of the signal lost in the power budget by free-space path loss can be somewhat recovered. On the other hand, the same gain of the antenna can be achieved with smaller antennas at higher frequencies compared to lower ones. This leads to another concept that is critical in satellite systems, which is the challenges introduced by the integration of the components on the space platform. However, the main enabler for the deployment of systems at higher frequency is the greater bandwidth that can be allocated. It can be way more feasible to design a telecommunication system with 200 MHz signal bandwidth using a carrier frequency at 40 GHz rather than at 1 GHz. The main figure of merit in this context is the fractional bandwidth (FBW), defined as the ratio between the allocated bandwidth and the carrier frequency. In a frequency allocation sense, the FBW is positively correlated with the actual cost of the frequency filing. As a general remark, allocating large bandwidth at L, S and X-band can be unfeasible also because nowadays the spectrum is crowded. The provisioned frequencies for SATCOM are listed in Table 1.3. As it can be seen, the available bandwidth increases with the operative frequency.

Two major impairments that can impact 5G SATCOM are latency and Doppler effect. 5G requires both time and frequency synchronization. With $d(t)$ as the distance between the two communicating terminals, which depends on time t, c the speed of light in vacuum and f the operative frequency,it is possible to compute $T_p(t)$ as in (1.4) and the Doppler frequency shift $\Delta f(t)$ as in (1.5).

$$T_p(t) = \frac{d(t)}{c} \tag{1.4}$$

$$\Delta f(t) = -f\frac{\dot{d(t)}}{c} \tag{1.5}$$

Depending on the scenario, equations Equation 1.4 and Equation 1.5 can be developed to obtain an approximation. However, many tools for the computation of satellites movement use perturbation methods like SGP, SGP4, SDP4, SGP8 and SDP8. The trajectory of a body

in space is expressed through state vectors, which comprise position vector, velocity vector and time epoch in a earth-centered inertial (ECI) reference system. However, the above mentioned models use two-line element (TLE) as input that describes satellite trajectory. TLE are two lines of 69 characters containing the space object name, identifier, epoch, parameters for the computation of state vectors and additional information on the evolution of trajectory, such as drag coefficient and derivatives of mean anomaly.

The path between satellite and ground is not only free space. Additional atmosphere impairments are more significant at lower elevation angles. Atmospheric gases can add a frequency-dependent attenuation, which depends on the water vapor content in the telecommunication path [13]. Local ground humidity, clouds, rain and fog impact strongly at higher frequencies [14]. Their effect is mainly attenuation, but they can also cause depolarization. Weather forecast models and required availability time are used to design a satellite coverage system. Refraction effects are caused by the troposphere temperature and pressure profiles, as well as scintillation due to the presence of charged particles in the ionosphere [15].

Apart from atmosphere, a large number of other impairments can be added into the channel mode. Thermal noise detected by the antenna can increase noise level and must be taken into account during the link budget. This is related to the Brillance noise emitted by the scenario in the field of view of the antenna. The co-existence with other systems can impact in terms of interferences.

1.1.2 Payload transceivers

A satellite telecommunication system must provide connectivity between space-born terminals and/or earth stations. A transceiver is a combination of a receiver and a transmitter, and can serve as transparent data relay or integrate functionalities of higher layers level than the physical layer. A sample transceiver architecture is shown in Figure 1.1.

The receiver front-end performs filtering and amplification to ensure a sufficient signal-to-noise ratio (SNR), setting the complete system noise figure (NF). It consists of low-noise amplifiers (LNAs) and a pass-band filter serving as an image rejection filter [16]. [17]. Several works are related to the design of 5G receivers [18] [19]. To process the received signal, most of the times, a superheterodyne or omodyne architectures are used, with a mixer and a variable local oscillator (LO). The LO signal is usually supplied by a phase-locked loop (PLL) controlled by a stable reference oscillator, such as a temperature-compensated crystal oscillator (TCXO). Another approach is the "direct sampling" [20], which bypasses hardware frequency conversion by directly sampling the radio frequency (RF) signal using high-speed analog-to-digital converter (ADC) or digital-to-analog converter (DAC). In this case, the main limitation concerns the maximum sample-rate achievable in the designed system. It can be dictated by hardware limitations for ADC and DAC [21] [22] or constraints in the power consumption.

The intermediate frequency (IF) chain comprises gain blocks and filter stages. In a

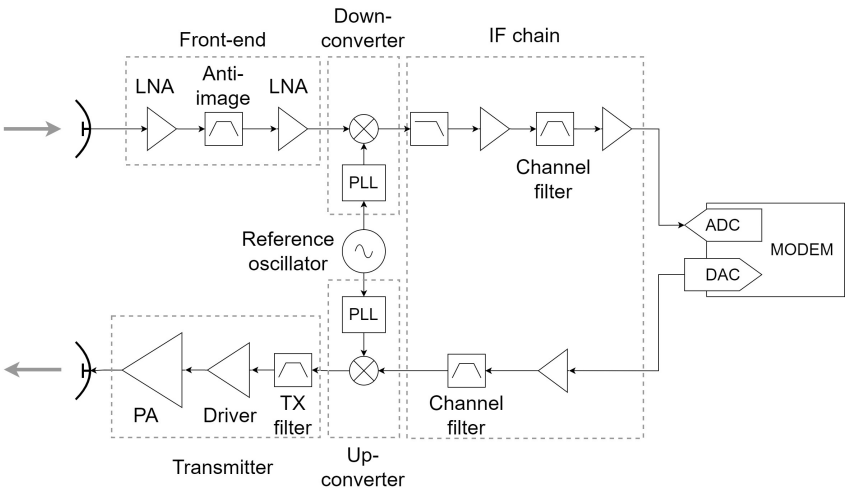

Figure 1.1: Sample diagram of a transceiver incorporating a modem.

transparent payload the IF chain is analog, while in regenerative case modulation and demodulation can be performed with a modem, integrating ADCs and DACs. Once the received or transmitted signal is in the digital domain, higher layers of the protocol stack can be implemented in the payload. In the 5G architecture, this leads to several interesting configurations of the network architecture, which will be explained in detail in the next sections.

The transmitted signal, at the output of the IF chain, is set to the desired transmitted frequency through an up-converter. This part of the circuit can be interfaced to a monolithic high-power power amplifiers (PAs) [23] [24], or to an active antenna, integrating multiple PA feeding its radiating elements [25] [26]. Monolithic solid-state power amplifiers (SSPAs) can be found in different technologies like GaAs [27] and GaN [28]. The GaN technology is the most suitable for high-power solutions, capable of delivering 40 dBm output RF power in Ka band [29].

An interesting solution that integrates transmitter, power amplifier stage and a steerable transmitting antenna is the active electronically steerable antenna (AESA). Printed circuit patch antennas are used as the radiating elements of the array. This is a cost-effective solution that allows integration of beam-forming (BF) chips and other components on the same printed circuit board. The array of radiating elements can be implemented in different configurations to minimize side-lobes in the radiation pattern, and with varying numbers of elements: the greater the number of elements, the higher the gain, beam-steering capability, and accuracy, but also the larger the antenna size, cost, and complexity of the beam-forming network. The BF network is the part of the system that carries the RF signal from the input port to the radiating elements. This section contains several power amplifiers, which increase the radiated power and thus the effective isotropic radiated power (EIRP). Programmable

TX Freq.	EIRP	P. Diss.	n° elem	Scan range	Dim.	Pol.	Ref
27–31	49	280	32x32	±70°	19.2x14.9 cm	Arb.	[30]
28–31	34	76	16x16	±60°	8.75x4.67 cm	Arb.	[31]
13.5–14.5	43		32x32	±70°	33.2x33.8 cm	Arb.	[32]
28–29	10		4x8	±55°		Arb.	[33]

Table 1.4: State of art on AESA.

Release	Start	End	Status	Summary report
Release 15	2016-06-01	2019-06-07	Frozen	TR 21.915 [34]
Release 16	2017-03-22	2020-07-03	Frozen	TR 21.916 [35]
Release 17	2018-06-15	2022-06-10	Frozen	TR 21.917 [36]
Release 18	2019-09-16	2024-06-21	Frozen	TR 21.918 [37]
Release 19	2021-06-18	2025-12-12	Open	/
Release 20	2024-03-14	/	Open	/

Table 1.5: Current status of 3GPP Releases involving 5G NR [38].

phase shifters are used for beam-pointing, steering the main lobe in the desired direction. In Table 1.4 a state of art on AESA technologies is reported.

1.2 5G NR

5G NR is the radio access technology defined by 3GPP for the fifth generation of mobile networks. This section begins with an overview of the standardization process and the 5G NR protocol stack, followed by a description of the physical layer and its main characteristics. It then examines the integration of NTN, focusing on the associated technical challenges. Finally, it outlines representative testbeds developed for evaluating and validating 5G NR in NTN scenarios.

1.2.1 Standardization and general overview

5G NR is standardized by the 3GPP consortium, which unites worldwide seven telecommunication standard development organizations: ARIB and TTC (Japan), CCSA (China), ETSI (Europe), ATIS (North America), TSDSI (India), TTA (South Corea). The initial objective on 3GPP, in 1998, was to develop technical specification for a 3G mobile system based on GSM core networks. The work in the following years evolved into the development and maintenance of UMTS with related 3G standards, LTE with related 4G standards and 5G NR. Actually, the initial study on improvements of 5G NR is ongoing and will be developed under the future 6G. 3GPP standards are organized in a system of "Parallel Releases". The date for every release are shown in Table 1.5.

The work on 5G began from Release 15, noted as "5G Phase 1", and continued in Release 16 and 17 as "5G Phase 2". Between Release 17, 18 and 19 further improvements led to

the final "NR Advanced" phase of the 5G development [39]. Release 20 will be the last 5G-related and will incorporate the initial 6G use cases study item. The work is planned to continue with the 6G requirements in Release 21.

The targeted improvements for 5G over the previous 4G standard can be listed according to the following profiles, described by 3GPP:

- enhanced mobile broadband (eMBB): increase the data-rate capabilities of mobile networks.
- critical communications and ultra reliable and low latency communications (URLCC): ensure reliable and real-time connection through mobile network for applications such as Edge Computing and Vehicular remote driving.
- massive internet of things (mIoT): support to networks composed by many devices in the context of Internet-of-Things.

As a general aspect 5G aims also to increase the network flexibility, depending on the requirements in a wide range of use cases[40]. In the following, the protocol stack is described. An overall description of the 5G NR system architecture is provided in [41], while the radio technology is described in [42]. The main components of the 5G architecture are the user equipment (UE), the new generation - radio access network (NG-RAN) and the 5G core network (5GC). The UE is connected to the services of the 5GC through the NG-RAN. An overview of the 5G NR network is reported in Figure 1.2.

The radio interface in the NG-RAN that connects the UE to the core network is the gNB base station. The signal path from the UE to the gNB is the uplink (UL), whereas downlink (DL) is the one on the opposite direction. 5GC comprehends at high level all the control infrastructure and the data network (DN), which is the main set of online services to which the UE connects. One of the main aspects of 5G NR is the separation of the *user plane*, related to the data traffic between users and the DN, from the *control plane*, which, on the other hand, represent the network components responsible for signaling and network management. This separation improves efficiency and reliability. Indeed, the control data exchange needed for network maintenance is way less than the huge user plane data traffic that goes towards the DN. Furthermore, the level of security needed in control and user planes can be significantly different, depending on the application. In the context of NG-RAN the gNB is not necessarily a monolith, but it can be divided in multiple gNB - distributed units (gNB-DUs) controlled by a gNB - centralized unit (gNB-CU). gNB-DUs are the physical interfaces of the gNB to the UEs. While gNB-CU handles the control plane instructions by higher layers of the network and orchestrates gNB-DUs. This separation is beneficial in terms of efficiency, but also because it enables the virtualization of network functionalities. This paves the way to emerging networking technologies such as software-defined networking (SDN) and network function virtualization (NFV) [43]. At the 5GC side,

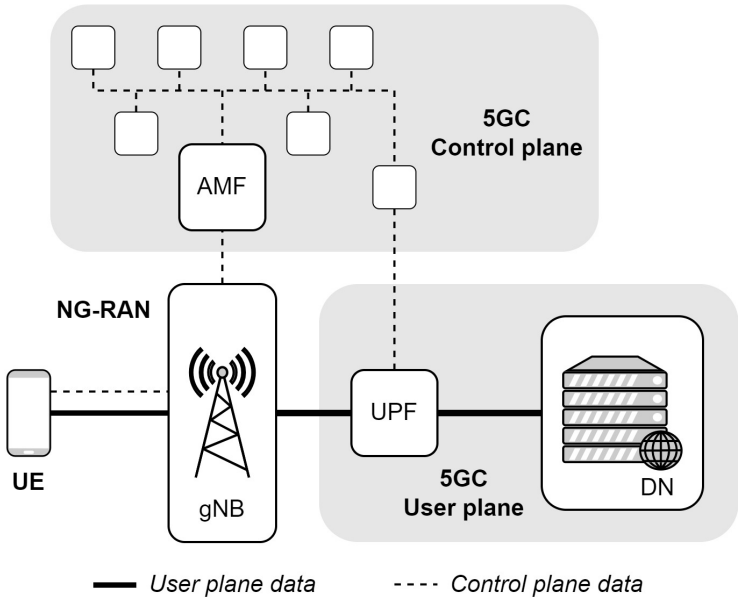

Figure 1.2: Simplified diagram of the 5G network architecture, involving: UE, NG-RAN with the 5G node B (gNB) and the 5GC divided in its User plane and Control Plane sections. Other components of the 5GC, rather than user plane function (UPF) and access and mobility management function (AMF), are not reported for simplicity.

the user plane traffic is handled by the UPF entity:, which is placed between the NG-RAN and the DN. The 5GC control plane interface to the NG-RAN is the AMF, which regulates the UE access to the NG-RAN, orchestrates mobility and other functions related to the control of user plane.

1.2.2 Protocol stack

The division of Control plane and User plane is evident in the protocol stack, for which two separate cases are provisioned. In Figure 1.3 a generic description of it is shown. Both signaling and data go through a common first layer stack:

- physical layer (PHY): the lowest layer in the stack that relates to the radio interface. Since the presented work is related to this layer, this will be explained in more detail in the next sections.

- medium access control (MAC): it manages the resources of the PHY through flow control, data multiplexing and schedules traffic from multiple UE to the gNB. This layer is where retransmission procedures and error corrections are implemented through hybrid automatic repeat request (HARQ), which is the combination of automatic repeat request (ARQ) together with forward error correction (FEC) [44].

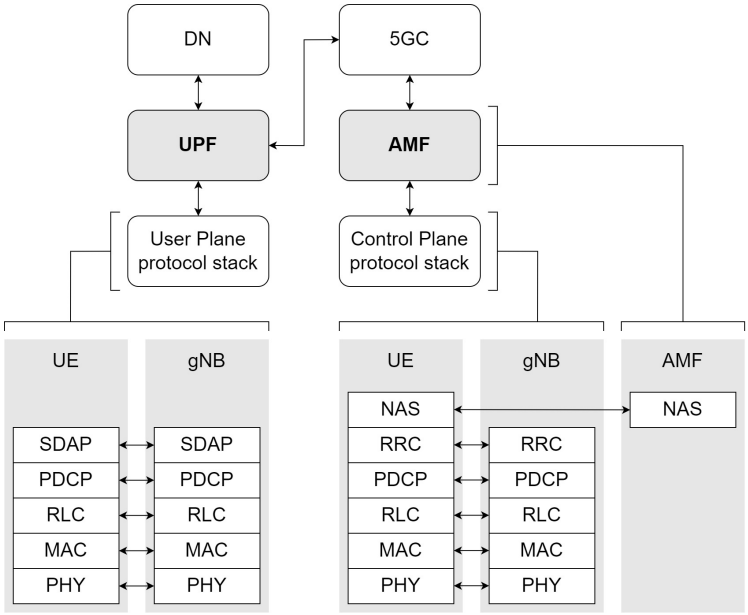

Figure 1.3: Diagram of the protocol stack, divided in User and Control plane cases.

- radio link control (RLC): three layer operative modes are provisioned: transparent mode (TM), unacknowledged mode (UM) and acknowledged mode (AM). RLC TM simply forwards packets from upper layers to MAC, while UM provide segmentation and reordering of packets that can come in inappropriate order from the MAC. The most complete mode, AM, comprises also ARQ strategies [45].

- packet data convergence protocol (PDCP): in this layer data encryption, packet compression and integrity protection are implemented. It acts as an interface between the physical resources management (RLC, MAC and PHY) and the management of higher level services [46].

Channelization is another key aspect of 5G, for which the flux of information and signaling is divided and forwarded to different physical or logical channels that spans across the protocol stack. Channels act as an interface between layers. Physical channels are within PHY and allocates data and signaling in different resources of the radio interface (subcarriers). This will be seen more in detail further. In the interface between MAC and RLC Logical channels divide and organize the traffic between broadcast information, unicast data, paging, and other control signaling. Another key MAC function is the mapping of Transport channels, which are the interface between the RLC Logical channels and the PHY Physical channels. The interface between PDCP and higher layers are the Radio Bearers, which can be divided in data radio bearers (DRB) or signalling radio bearers (SRB). The presented list of channels is depicted in Figure 1.4.

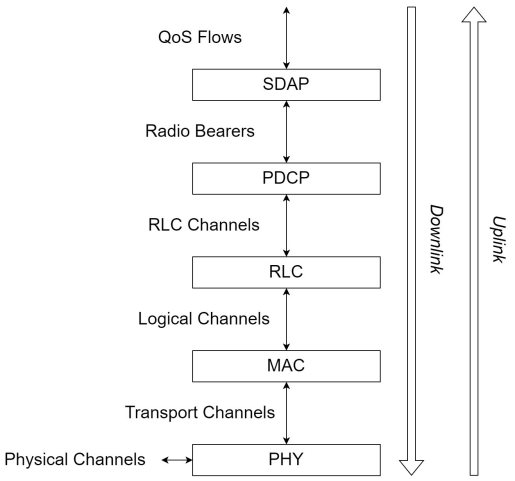

Figure 1.4: 5G layer 1 and 2 protocol stack, with a focus on channelization between layers.

From this point on, the higher protocol layers are:

- service data adaptation protocol (SDAP): it is present only for the User plane and is bypassed for the Control plane. It is not present in LTE. Its main function is to map quality of service (QoS) flows to Radio bearers. QoS flows are channels that can forward services of different type. For instance, video broadcasting QoS flow is separated from voice calls services. In this way the network can handle the two type of services in a different way, based on their needs [47]. The data traffic from this layer finally goes to the 5GC through the UPF.

- radio resource control (RRC): its main function is to handle the establishment, maintenance and release of communications between UE and gNB. RRC discipline the UE connection states: idle, inactive and connected; it also helps handover processes and assigns QoS flows. Key components for the protocol are the RRC timers, which discipline several operations, giving the maximum time to wait for RRC requests [44].

- non access stratum (NAS): this is the final layer that interfaces UE signaling to the 5GC through the AMF. Together with RRC it is present only for the Control plane. NAS is related to the authentication of the UE and other functions that ensure that the device has a known identity when interfaced with the network [48].

With respect to the open systems interconnection protocols (OSI) stack, Layer 1 is associated with PHY, while in Layer 2 MAC, RLC, PDCP and SDAP are present, and in Layer 3 RRC and NAS.

FR1	410 MHz - 7125 MHz
FR2	24.25 GHz - 71.0 GHz

Table 1.6: 5G NR frequency bands

1.2.3 Physical layer

The presented work is mostly related to hardware technologies enabling 5G in space, therefore, a major detail will be spent in this section to describe the physical layer PHY.

5G is based on orthogonal frequency-division multiple access (OFDMA), which makes possible for multiple users to organize the main physical resources: frequency and time [49]. With OFDMA the signal bandwidth is divided in multiple orthogonal subcarriers. Their spacing is named subcarrier spacing (SCS). The duration of OFDMA symbol is proportional to $1/SCS$. A standard OFDMA transceiver does not comprise multiple frequency conversion stages to allocate each subcarrier. Instead, the transmitted OFDMA symbols are computed by inverse fast fourier transform (IFFT) of the subcarriers vector describing a OFDMA symbol. At the receiver side, subcarriers symbols are extracted by fast fourier transform (FFT) of the received samples of the OFDMA signal. FFT size is the number of samples used by IFFT and FFT processing, which must be greater than the number of subcarriers. Being the N_{FFT} the FFT size, the OFDMA transceiver should work, at least, with a sample rate equal to $N_{FFT}SCS$. In the time domain, each symbol is spaced by a guard-time, needed to mitigate inter-symbol interference (ISI) between two consecutive symbols. In the frequency domain some subcarriers at the edges of the bandwidth are leaved null to respect a guard-band needed to mitigate adjacent channel interference (ACI). In a slow frequency-selective channel, multipath can affect significantly ISI. This is mitigated through the cyclic prefix (CP), which consists of filling the guard-time replicating the last OFDMA symbol samples for each symbols. In this way frequency-selective channel equalization is simplified. For more details refer to [50]. However, the duration of CP affects throughput, and it should be more than the duration of the channel impulse response. Channel equalization comes after channel estimation, which is performed through known pilot subcarriers, used to probe the channel frequency response. Data subcarriers are the one used for data transmission, while guard subcarriers are those allocated in the guard-band. The physical resources are divided in this way in resource elements, which are single subcarriers in a OFDMA symbol. The general picture of what have been described is reported in Figure 1.5

5G NR frequencies are divided in two main sections, FR1 and FR2, according to Table 1.6.

For each group other standard sub-bands are defined: from n1 to n109 for FR1 and from n257 to n263 for FR2. Each one can be allocated with defined channel bandwidths, utilizing either time division duplexing (TDD) or frequency division duplexing (FDD) for the uplink-downlink duplexing. In FDD uplink and downlink frequencies are separated, while in TDD

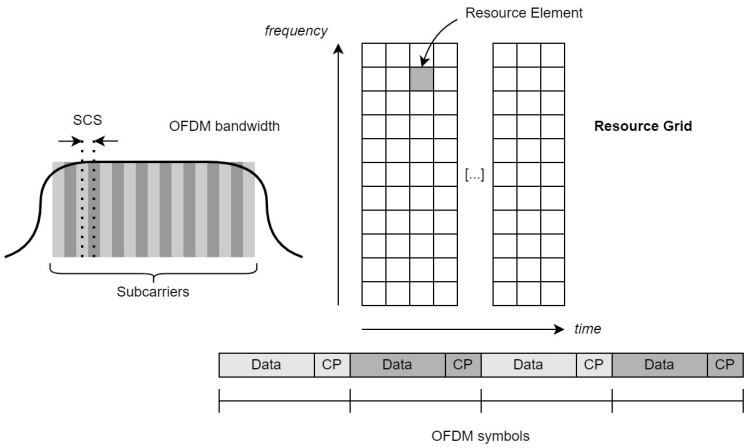

Figure 1.5: General picture of an OFDMA system physical resources.

Name	Duplex	Uplink (MHz)	Downlink (MHz)	Channel bandwidth (MHz)
n254	FDD	1610 – 1626.5	2483.5 – 2500	5, 10, 15
n255	FDD	1626.5 – 1660.5	1525 – 1559	5, 10, 15, 20
n256	FDD	1980 – 2010	2170 – 2200	5, 10, 15, 20

Table 1.7: FR1 NTN frequency bands

the duplexing is performed in terms of allocated resources in the resource grid [51]. Within FR1 and FR2 other frequency bands designed for NTN are also defined. These are the 5G frequency bands used in this work. For this reason, they are listed in Table 1.7 and Table 1.8 [52] [53].

In 5G a physical resource block (PRB) is defined as 12 consecutive subcarriers in the frequency domain. The number of usable PRB is defined in [51] for each pair of SCS and total channel bandwidth, in FR1 and FR2 frequency ranges. In a similar fashion, the minimum guard-band is specified. The time domain is divided in 5G in radio frames, each 10 ms long. A radio frame is divided in 10 sub-frames, each divided in slots, which are composed of consecutive OFDMA symbols. This division is defined by the quantities N_{symb}^{slot}, N_{slot}^{frame} and $N_{slot}^{subframe}$, being symbols in a slot, slots in a radio frame and slot in a frame, respectively. In 5G, numerology refers to the SCS configuration that can be used and the time division of radio frames. This specification is dictated by the compromise between

Name	Duplex	Uplink (GHz)	Downlink (GHz)	Channel bandwidth (MHz)
n510	FDD	27.50 – 28.35	17.30 – 20.20	50, 100, 200, 400
n511	FDD	28.35 – 30.00	17.30 – 20.20	50, 100, 200, 400
n512	FDD	27.50 – 30.00	17.30 – 20.20	50, 100, 200, 400

Table 1.8: FR2 NTN frequency bands.

μ	SCS (kHz)	N_{symb}^{slot}	N_{slot}^{frame}	$N_{slot}^{subframe}$	CP mode	Symb. duration (us)
0	15	14	10	1	Normal	71.35
1	30	14	20	2	Normal	35.68
2	60	14	40	4	Normal	17.84
2	60	12	40	4	Extended	71.35
3	120	14	80	8	Normal	8.92
4	240	14	160	16	Normal	4.46
5	480	14	320	32	Normal	2.23
6	920	14	640	64	Normal	1.12

Table 1.9: Numerology table as in [49]

versatility in many scenarios and spectral efficiency. Each numerology is defined with the letter μ and affects also the CP length. The higher the SCS, the lower the CP length. CP mode can be either normal or extended, depending on the formula used for the computation of CP length. For more details refer to [49]. A summary of 5G numerologies is reported in Table 1.9.

The frame subdivision is the starting point of the allocation of time resources between users and uplink/downlink. Several duplexing modes are defined, at slot subdivision level, for TDD 5G scenarios.

The resource grid of PHY is divided in uplink and downlink in different physical channels, related to transport channel at MAC, connected to logical channels at RLC [54] [55]. For the downlink they are listed in the following:

- primary downlink shared channel (PDSCH): main channel for the transmission of user data, together with information of higher layers and system information block (SIB). Its modulation and coding scheme can be dinamically adjusted based on the link conditions.

- primary downlink control channel (PDCCH): it carries downlink control information (DCI) for the downlink stream, which transports information on the channel state and the schedule instructions for the allocation in the resource grid of the PDSCH and its counter part for the uplink. The modulation and coding scheme is fixed to quadrature phase shift keying (QPSK) with polar coding.

- physical broadcast channel (PBCH): used to broadcast synchronization signal from gNB to the UE connected to the cell. The synchronization procedure will be examined with more detail.

On the other hand, uplink physical channels are:

- primary uplink shared channel (PUSCH): counterpart at the uplink side of the PDSCH, used for user data.

- primary uplink control channel (PUCCH): in a similar fashion to PDCCH it carries uplink control information (UCI), which may contain acknowledgement, requests for the gNB or channel state information.
- physical random access channel (PRACH): used to access the channel. It will be detailed better when describing the random access channel (RACH), which is the transport channel at MAC that handles the initial UE connection with a gNB.

The physical channels hosts control, user data, and also physical channels, which are known subcarrier patterns that enable several protocol functions. They are listed below as well.

- primary synchronization signal (PSS) and secondary synchronization signal (SSS): reference signals used for downlink synchronization. They are contained in the synchronization signal block (SSB) (explained later). PSS and SSS can be one out of several possible known sequences, which the UE checks in parallel. The type of sequence broadcasted by the gNB is a sort of identifier of itself, or one of its beams in case of beamforming.
- demodulation reference signal (DM-RS): pilot subcarriers used for channel estimation, spread among the resource elements of PDSCH and PUSCH.
- sounding reference signal (SRS): known subcarriers sent by UE, received by the gNB to sense the channel state and optimize resource allocation and scheduling.
- phase-tracking reference signal (PT-RS): optional reference signal used to track the phase of the transmitter local oscillator, to mitigate its phase noise or frequency drift. This is particularly useful at higher frequencies and with high order modulation schemes.
- positioning reference signal (PRS): like SRS it is a sounding signal, but transmitted by gNB and received by UE. This is used for estimation on time and direction of arrival, for UE that can implement beamforming, or in applications like drones or automotive. Also SRS can be used in a similar way at gNB side.
- channel state information reference signal (CSI-RS): downlink sounding signal, which can seem similar to PRS, but its purpose is different and relies within the wider framework of channel state information (CSI). While PRS is used by UE only, CSI-RS is sent by gNB expecting that the UE reports back its estimations, helping the gNB to make the CSI-report. This is useful for the gNB in the context of beam-management and UE scheduling.

In this section the main components of the 5G NR physical layer have been presented. Now the focus is shifted to the RACH procedure, which specify how a UE can get access to

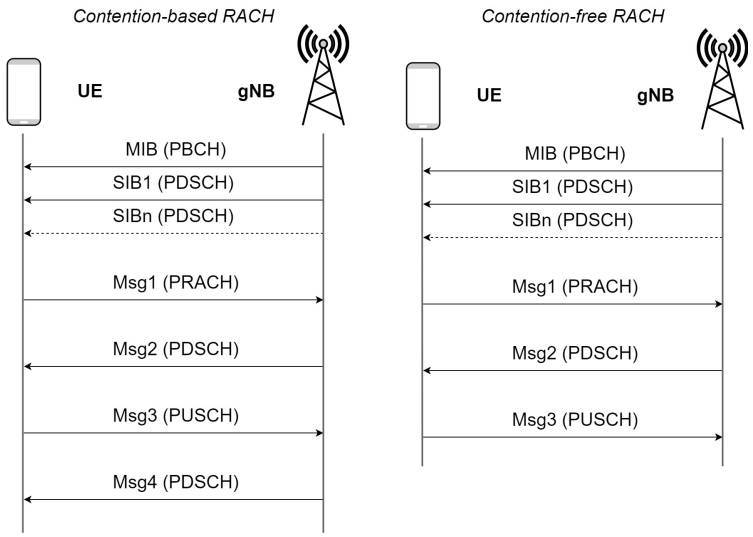

Figure 1.6: RACH procedure in 5G NR in contention-based and contention-free cases.

a gNB. RACH can be triggered at RRC in different ways: initial access from RRC inactive mode, handover, re-connections and other scenarios for which the UE should authenticate to the gNB or require more information. Contention-based RACH is defined when multiple UE can randomly access the network using the same PRACH preamble. This scenario is used for the majority of cases and expecially when a UE wants to access the network from RRC inactive. On the other hand, contention-free RACH occures during handover or services for which a deterministic and reliable behaviour of the access to the network is needed. In Figure 1.6 the sequence of messages for contention-based RACH is shown, and they are listed in the following:

- Downlink synchronization: the UE which wants to connect to a gNB does not know its configuration, such as SCS, therefore, a synchronization procedure is needed. The minimum set of information needed is acquired with master information block (MIB) and SIB1 messages. At first with the MIB message on PBCH, which gives information on how to demodulate the SIB1 on PDSCH. Every 2 frames (20 ms) the gNB broadcasts bursts of SSB. The structure of the SSB is fixed and is depicted in Figure 1.7. It comprises PSS, SSS and PBCH. The PBCH contains the MIB, together with DM-RS for channel compensation. The PBCH is updated with the current MIB every 80 ms. On top of that, gNB broadcast on PDSCH the SIB1 every 160 ms. Other SIBs (SIB2, SIB3, SIB4...) are periodically transmitted by gNB on PDSCH in the PDSCH and give further information to the UE.

- Msg 1 PRACH Preamble Transmission: The UE detects the SIB and selects a pseudo-random Zadoff-Chu preamble to be transmitted on the PRACH. This acts as a tempo-

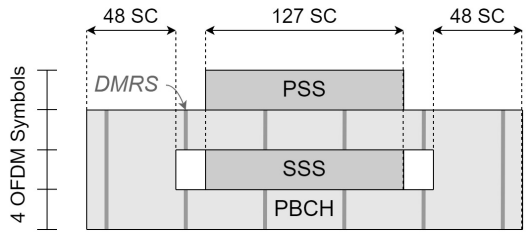

Figure 1.7: SSB downlink signal structure.

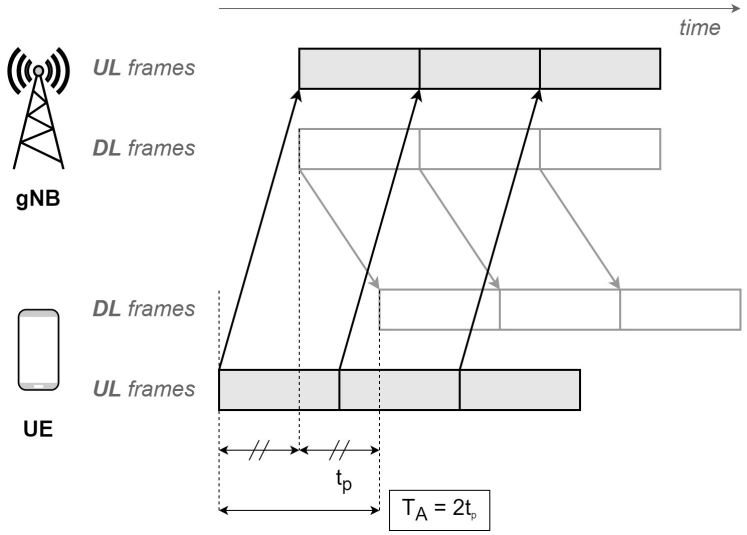

Figure 1.8: Uplink timing in 5G NR. The UE adjusts its uplink start of frame in order to have at gNB side uplink and downlink start of frames at the same timing.

rary identifier for the UE. The gNB still does not know if multiple UEs are contending the same identifier.

- Msg 2 random access response (RAR): The gNB replies in the PDSCH to the UEs assigning another temporary identifier, to distinguish among them, and specifies their transmission window with a key information: the timing advance (TA). The uplink start of frame time must be adjusted according to the propagation delay, avoiding collisions between frames in uplink or downlink at both ends. To achieve this the gNB informs the UE, through the TA, on how much to anticipate the start of frame for PUSCH, PUCCH and SRS. A schematization of this process is reported in Figure 1.8.

- Msg 3 RRC Connection Request: UE aligns its timing according to TA and sends a RRC request to conect to the gNB through PUSCH.

- Msg 4 (Contention Resolution): if only one UE Msg 3 is decoded by the gNB, it concludes the handshake with an ACK in the PDSCH. If multiple UEs RRC requests

are decoded, the gNB performs other operation to grant the connection to only one and restart the RACH for the others.

In contention-free RACH the steps are slightly different. At first, the gNB sends a unique preamble, defined by the network, to a specific UE, thus, eliminating any chance of collisions. The UE sends back the received preamble within the PRACH. At the end, the gNB transmit the RAR with TA and UE identifier.

1.2.4 NTN in 5G

The work of 3GPP on NTN started in the context of Rel-15. The study carried out was published in 3GPP TS 38.811 [56] [57]. 3GPP classifies NTN as a network where space platforms like LEO, MEO or GEO satellites or airborne platform act as a relay node or a base station [56]. The identified NTN use cases identified are:

- *Service ubiquity*: serve "unserved" or "underserved" areas, like rural places and off-shore sea platform, thus filling the gap of the terrestrial 5G infrastructure.
- *Service continuity*: increase the availability and reliability of 5G network services even in case of moving users.
- *Service scalability*: by using the large area served by satellites, the NTN infrastructure can be used for off-loading the terrestrial infrastructure traffic and scale its capacity dinamically.

The main system blocks of a 5G NTN are listed in the following [58]:

- one or more UEs which connects to the network through the satellite platform. The network can serve UEs classified as very small aperture terminal (VSAT), which incorporate directive antennas, like reflector antennas, and can be suitable for K/Ka band links. Otherwise, UEs can also be handled devices with omni-directional antennas. This kind of application is more suitable for lower frequency bands like S band.
- a service link between the UE and the space platform.
- a space platform hosting the telecommunication payload: transparent or regenerative.
- inter satellite links (ISLs) in case of satellites connected in a constellation, incorporating gNB.
- a gateway connecting the satellite platform to the core network.
- a feeder link between the gateway and the satellite platform

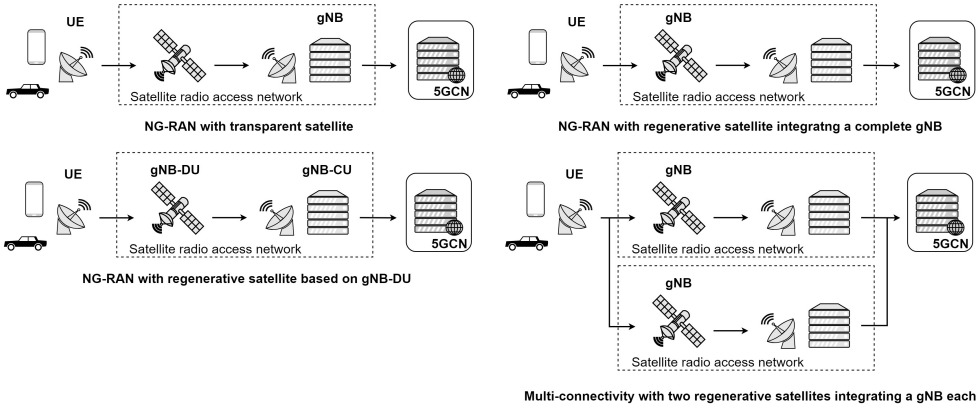

Figure 1.9: NG-RAN examples for NTN

The satellite platform can integrate a *transparent payload* performing frequency conversion, filtering and signal amplification. The payload is transparent to any protocol and its features are all within the physical layer. It can be used to serve as a relay between UE and gNB, or between multiple gNBs. On top of that, if the payload integrates higher layers functionalities, it can be considered as a *regenerative payload*. Its functionalities are those of a transparent payload plus demodulation, decoding, routing, modulation and/or encoding. In this latter case, the gNB can be on board the satellite platform: as a monolith, or splitted in gNB-CU and gNB-DUs among the NTN network components. For each of these cases multiple NG-RAN architectures are defined [56]. Some examples are reported in Figure 1.9. The radio access to a 3GPP core network can also be accomplished through a non-5G connection type, e.g., DVB-S2X. The direct-to-device use case is of particular interest in this work and regards the full 5G-compliant connection between UE and the 5G NTN infrastructure [59].

Several works in the literature, related to 3GPP documents, explain the NTN scenario highlighting the challenges and possible solutions [60]. On notable advancement in NTN is the adoption of the SIB19 downlink signal, specified in [61]. The information contained in the SIB refers to satellite ephemeris and timing adjustments, that the UE can use to synchronize itself with the NTN scenario. In the following the main design challenges and related solutions are listed. The analysis is here restricted to the scenario of a fixed UE with a focus on direct access to LEO satellites with transparent payload.

- *Frequency alignment*: Satellite movement, especially for LEO, introduces a time-varying Doppler frequency shift to the 5G signal. A closed form for the computation of Doppler shift during a satellite passage is described in [62]. In a OFDM waveform based technology such as 5G NR, it is straightforward to say that the impact of the Doppler shift is relevant when it is comparable to or higher than the SCS. The Doppler spread of a LEO satellite at 600 km altitude, relative to a fixed UE, can range up to

± 48 kHz at 2 GHz carrier frequency and ± 480 kHz at 20 GHz. If the SCS is not wide enough the total frequency shift at the UE should be compensated. As described in [63], the frequency offset is both compensated in downlink and pre-compensated in uplink by the UE. This can be done through downlink reference signals, i.e. SIB19 packet containing satellite ephemeris data, from which a UE with GNSS capabilities can estimate Doppler shift. On the other hand, the UE can be adviced by the 5GC on the required compensation to be performed.

- *Timing*: propagation delay in a NTN scenario are certainly higher than in terrestrial network. The round-trip time (RTT) is dependant on elevation angle of the satellite with respect to the earth station. It is in the order of 10 ms for a LEO scenario and around 130 ms for a GEO satellite. This relates to the fact that for some RRC procedures a time window extension is needed, e.g. RRC timers procedure, RAR time window size, Contention Resolution window size, TA, and HARQ. In a LEO scenario the RTT changes with satellite motion, therefore, the TA received from gNB should be adjusted further to align with it.

- *SNR*: For a one-way signal path, the main SNR is dependent on the EIRP of the transmitter ($EIRP_{TX}$), the G/T of the receiver (G/T_{RX}), the total path loss (L_{tot}), which increases with carrier frequency, and the signal bandwidth B. As described in (1.6), with k as the Boltzmann constant [11].

$$SNR = EIRP_{TX} + G/T_{RX} - L_{tot} - 10\log_{10}(kB) \tag{1.6}$$

  Expecially in the context of direct access, UE power and size constraints at UE and non-terrestrial platform can impact EIRP or G/T, depending on which component is at transmitter or receiver side. Dimension of the receiving/transmitting antennas impact both EIRP and G/T. They can be a big concern for handled UE devices or telecommunication system installed on moving platforms. On the other hand, satellite platform are limited mainly for what concerns transmitted power, expecially with the trend towards the deployment of small satellites in LEO [6]. In the context of regenerative payloads, uplink signal path from UE requires a high satellite receiver sensitivity. The trade-off between SNR and throughput is often shifted towards modulation and coding schemes with low spectral efficiency (less than 1 bit/Hz) [64], compared to earth-borne 5G links. If also a narrow bandwidth is needed to close the link with a sufficient SNR, then SCS can be reduced to increase throughput, but increasing the impact of Doppler shift and timing issues analyzed before.

- *HARQ*: To improve reliability 5G NR supports Stop-And-Wait HARQ. Up to 16 multiple processes are possible in uplink and downlink [54]. It is possible to compute the minimum number of HARQ processes needed to achieve maximum throughput

($N_{HARQ}^{(min)}$) as in (1.7); with TTI as the time to transmit a transmission block, and T_{HARQ}, dependent on RTT, as the HARQ processing time.

$$N_{HARQ}^{(min)} = \frac{T_{HARQ}}{TTI} \tag{1.7}$$

If the above-mentioned condition is not satisfied, it is not possible to occupy the maximum number of time slots, since there can be the possibility that all HARQ process identifiers are occupied and every process is waiting for a ACK/NACK. If the reception time window is narrower than RTT the connection can even stall. As an example: by considering a T_{HARQ} of 29 ms, comprising RTT for a LEO satellite and processing time, and 1 ms of TTI, the minimum number of HARQ processes should be 29 [65], greater than what is provisioned in [54]. Viable solutions can be increasing the number of HARQ processes, ensuring better throughput but with greater buffer size reserved for HARQ for UE; or disabling HARQ, addressing re-transmission procedures to higher level protocols.

1.2.5 Testbeds for 5G NTN

5G testbeds are an essential tool for validating network architecture and the interfacing between hardware equipments with the proposed software radio-stack. The work presented in [66] proposes cross-layer adaptations made to OpenAirInterface5G to ensure compliance with 3GPP Release 17, as part of the 5G-LEO project. This project focuses on enabling direct access to 5G services from ground UE via a transparent payload LEO satellite. Given the unique challenges of LEO satellite communications—such as high and time-varying Doppler shifts, significant RTT, and frequent handovers represents one of the first efforts to adapt the 5G protocol to these conditions. A software defined radio (SDR)-based end-to-end demonstrator was developed to validate these adaptations. The experimental results from this demonstrator confirm the feasibility of direct 5G access through LEO satellites. [67] evaluates an OpenAirInterface implementation for direct satellite access using a 5G NR waveform. The study connects OpenAirInterface UE and a gNB through a satellite channel emulator to assess the performance of various IP-based protocols over geostationary transparent payloads. Experimental results indicate that the implementation is stable, achieving uplink and downlink speeds of 3.5 Mbit/s with a typical geostationary latency of approximately 600 ms. The findings confirm that this software-based demonstrator is suitable for investigating broadband universal service applications. In the context of OpenAirInterface, the work presented in [68] introduces a 5G mobile network testbed designed with a virtualised and containerized architecture, enabling integration with artificial intelligence applications. Built using open-source technologies, the testbed allows for the deployment and orchestration of virtual network functions to create flexible mobile network scenarios with different fronthaul and backhaul topologies. Key advantages of this setup include its relatively low

cost and its capability to leverage artificial intelligence for network performance optimization. The future coexistence of integrated NTN and terrestrial networks is examined in [69]. It leverages SDN to monitor network traffic and make dynamic routing decisions through traffic handovers in response to unexpected events such as congestion or link failures. Additionally, for traditional handovers caused by the loss of Line of Sight, the SDN controller proactively manages the transition to minimize traffic loss. The study highlights the potential of SDN-based approaches in enhancing the reliability and efficiency of integrated NTN-terrestrial networks. In the presented papers, overall communication performance is evaluated at the transport and application layers. NTN adaptations are tested by assessing frequency and timing offset compensation. Throughput is measured using commercial software such as iPerf, while latency is assessed via ping commands. At the application layer, various services are tested, including voice-over-ip (VoIP), web browsing, Ookla speed test, and YouTube video streaming.

Chapter 2

Scenario

In this chapter the main missions that served as reference scenarios for this work are presented. For each mission, a link budget analysis is provided. An application-specific system analysis is also carried out, focusing on power compression and phase noise introduced by the satellite payload's power amplifier and frequency conversion stages, in the context of OFDMA. Additionally, the impact of frequency offset caused by frequency conversions in a transparent payload 5G satellite system is examined. The components mentioned in this chapter will be described in detail in chapter 3.

2.1 Missions description

Much of this work focuses on the design of satellite transceivers. During the time at Picosats, several projects were dedicated to develop K/Ka-band transceivers, resulting in three design iterations carried out over the course of the PhD. Each iteration addressed a different use case, requiring specific modifications that ultimately led to a new version of the design. This chapter presents selected aspects from these iterations to highlight the overall design process and the challenges encountered in this context. In the following the three relative projects, in a chronological order, are listed:

- *radiosat* and *beamsat* in-orbit demonstration (IOD).
- 5G live in-orbit demonstration (LIDE) mission.
- design of an improved version of the 5G transceiver designed for covering the complete K/Ka band fixed-satellite service (FSS).

A crucial step for the development of a satellite communication system is the IOD, required to validate system performance directly in space. IOD plays a crucial role in verifying compliance with design requirements and enhancing the technology readiness level

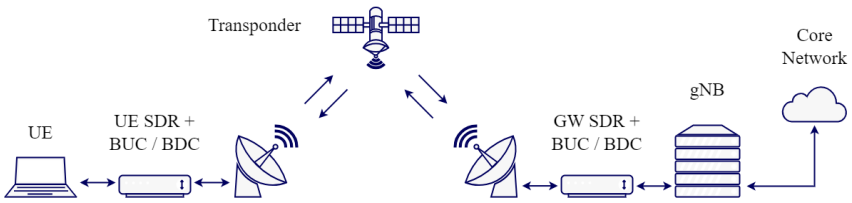

Figure 2.1: LIDE mission scenario and key components.

(TRL) of new components, enhancing their appeal on the market. This study focuses on the in-orbit validation of a regenerative transponder operating in the K/Ka band (*radiosat*), alongside a dual-band, dual-polarization horn antenna (*beamsat*). This mission aimed at evaluating the performance of the *radiosat* Ka-band transponder and the *beamsat* Ka-band horn antenna in an operational space environment. These technologies were integrated into the D-Orbit ION Satellite Carrier SCV13, and launched on November 11th, 2023, as part of the SpaceX Transporter-9 mission. Following the deployment, the validation phase started on February 27th, 2024 once the satellite entered a sun-synchronous orbit at an altitude of 645 km. The operations were successfully completed on August 31st, 2024.

LIDE is an European space agency (ESA) funded project for the demonstration of 5G-compliant satellite link between a UE and a gateway (GW) through a transparent K/Ka-band satellite relay [70]. The satellite platform is a 12U CubeSat, equipped with a bidirectional transparent K/Ka-band transponder system, connecting a UE with a GW integrating a gNB. The ground-based UE and GW adopt 5G commercial software radio stack compliant with the technical standards defined by 3GPP, provided by Amarisoft, adapted for the NTN scenario. Each UE and GW terminals includes a SDR, a block up-converter (BUC), and a block down-converter (BDC). The K/Ka band links connecting ground terminals with the satellite are named hereafter service uplink and service downlink, for the ones related to UE and feeder uplink and feeder downlink for those related to GW. The target bit-rate is 1 Mbps in upload and 10 Mbps in download, measured at UE side. The SDRs generate signals in the n256 frequency band (uplink: 1995 MHz; downlink: 2185 MHz), which is designated for FR1 NTN applications in FDD mode by 3GPP [63]. The chosen SCS is 30 kHz. A simplified diagram of the mission is shown in Figure 2.1. The mission payload was deployed successfully on 23/07/2025 with SpaceX Falcon9, as reported in ESA news page [71]. A photo of the LIDE release is shown in Figure 2.2.

The final iteration of transceiver design was developed to extend the bandwidth beyond the previous versions. The receive band was expanded from 27.0 GHz to 30.2 GHz to 27.0 GHz to 31.0 GHz, and the transmit band from 17.0 GHz to 20.2 GHz to 17.0 GHz to 21.0 GHz. This upgrade introduced additional challenges, which will be discussed later, along with adaptations aimed at enabling not only transparent operation but also compatibility with a modem, paving the way for a regenerative payload. Furthermore, this

Figure 2.2: LIDE satellite deployment.

device will enable the integration in the space platform of a SDR modem connected to the transceiver IF outputs. The previous versions where designed to be used in a transparent payload scenario, without the integration of other systems which perform modulation/demodulation at IF. This will enable the evolution towards regenerative payload, which, in the context of 5G will make possible to integrate the gNB onboard.

Two link budget studies were carried out in the *radiosat/beamsat* IOD and in the LIDE missions. In botses this is a crucial mission design phase, for which, antenna gain and size, transmitted power, receiver sensitivity and other system specifications are extracted from telecommunication link requirements such as bit-rate and availability. The SNR is the main low-level parameter to assess the feasibility of a link. As shown in (1.6) SNR depends on the EIRP of the transmitter, the G/T of the receiver and all the impairments added by the link path. This was described in subsection 1.1.1.

The main *radiosat/beamsat* IOD link parameters are listed in Table 2.1. In Table 2.2 the link budget for the LIDE mission is reported. In this case feeder uplink / feeder downlink are the two signal paths defined for the GW connection to the satellite relay, and service uplink / service downlink are those for the other path between UE terminal and satellite. The relay is transparent and the total SNR resulting from the uplink and downlink path combined can be expressed as in (2.1), by computing the two separate uplink and downlink link budgets and combining them afterwards [72]. In the LIDE link budget a dedicated analysis was performed on the noise added by the transponder SSPA non-linearities, as described in section 2.2.

$$SNR_{tot} = \frac{SNR_{UL} SNR_{DL}}{SNR_{UL} + SNR_{DL}} \tag{2.1}$$

2.2 SNR degradation due to non-linear distortion

A common issue in telecommunication systems using modulations with variable amplitude envelope, like OFDMA, is the peak-to-average power ratio (PAPR) [73] [74] [75] [76] [77]. The input-to-output power characteristic of a transmitter can induce both amplitude-to-amplitude distortion (AMAM) and amplitude-to-phase distortion (AMPM), which affects signal quality. AMAM is related to the amplifier gain with respect to the input signal power. AMPM, on the other hand, is related to phase shift induced by the amplifier. This phenomena can be added on a link budget as a SNR degradation, dependent on the output back-off (OBO), which is the power ratio between the actual mean power at the transmitter output and its saturated power. Depending on the waveform used a low OBO induces a SNR degradation due to AMAM and AMPM, which increases the noise floor due to self-interference. With SNR degradation we refer to the SNR achievable with a distortion-free transmitter and a mean output signal power equal to the transmitter saturated power. A high OBO leads to an SNR degradation as well, but in the sense that the mean power used is less than the saturated power. In this work a simulator in Matlab for computing the SNR degradation due to non-linearities was defined. The amplifier model used in the simulator is related to the SSPA used in the transceiver designs presented in the following chapters, whicn deliver up to 40 dBm output saturated power in K band. Only AMAM is included in the computation since AMPM is under 5° and can be neglected. The distortion simulation uses as input parameters the number of subcarriers, the number of guard and pilot subcarriers (even if no channel estimation is done in this simulation), the AMAM distortion characteristic with respect to amplifier input power, and the OFDMA signal mean input power. A schematic of the simulation performed is given in Figure 2.3.

A simulation run begins by defining a stream of QPSK, unit-power, randomly generated symbols. The symbols are then inserted into a vector, to which the symbols of the pilot carriers are added: in this way the frequency samples of the single OFDMA block are generated. Using IFFT, the time domain samples vector of the individual OFDMA block are generated. The FFT size is chosen as the first power of 2 higher than the total number

Table 2.1: *radiosat/beamsat* IOD link budget main parameters, at 20° satellite elevation.

Parameter	Uplink	Downlink
Satellite antenna gain	24 dBi	20 dBi
Earth station antenna gain	49 dBi	46 dBi
Polarization	LHCP	RHCP
Transmitter power	30 dBm	32 dBm
Carrier frequency	29.0 GHz	19.8 GHz
Receiver noise figure	3.0 dB	2.5 dB
Signal bandwidth	300 kHz	300 kHz
SNR	24.0 dB	8.2 dB

Table 2.2: Link budget summary of LIDE mission, at 50° satellite elevation.

Single trip parameters				
Parameters	S. UL	F. UL	S. DL	F. DL
Frequency	29.1 GHz	29.5 GHz	19.2 GHz	18.8 GHz
TX EIRP	39.4 dBW	54.2 dBW	22.4 dBW	7.5 dBW
RX G/T	$-10.1\,\mathrm{dB\,K^{-1}}$	$-11.4\,\mathrm{dB\,K^{-1}}$	$6.4\,\mathrm{dB\,K^{-1}}$	$19.8\,\mathrm{dB\,K^{-1}}$
Path loss	178.6 dB	178.7 dB	175.0 dB	174.8 dB
TX output power	4.8 dBW	10.0 dBW	6.0 dBW	−10.0 dBW
RX input power	−96.5 dBm	−83.3 dBm	−94.5 dBm	−95.8 dBm
Signal bandwidth	5.0 MHz	10.0 MHz	10.0 MHz	5.0 MHz
Single link SNR	8.3 dB	18.5 dB	9.1 dB	11.7 dB

Satellite bent-pipe link SNR	
Total SNR UE to GW	6.7 dB
Link margin UE to GW	4.1 dB
Total SNR GW to UE	8.6 dB
Link margin GW to UE	6.0 dB

of subcarriers. The proposed model is memory-less and works only on the instantaneous time domain samples, as shown in (2.2). Being x the input signal sample, y the output signal sample and $AMAM(|x|^2)$ the AMAM characteristic, which is dependent on the input sample power $|x|^2$.

$$y = xAMAM(|x|^2) \tag{2.2}$$

To make a comparison with a transmission without AMAM distortion, a copy of the symbol vector of the OFDMA block is created. The un-distorted samples are amplified in a uniform way, according to the gain G_0 computed as the AMAM value at the OFDMA mean input power P_{in}. No oversampling operation is done at this stage. An additive white gaussian noise (AWGN) type channel is used. Multiple copies of the vector of samples output to the transmitter are generated, one for each E_b/N_0 sample used to graph the bit error rate (BER): each is associated with a different level of E_b/N_0, from which real and imaginary parts of white Gaussian noise standard deviation are calculated. The power of each component of the noise is σ^2, computed by reversing the E_b/N_0 formula, as shown in (2.3).

$$\sigma^2 = \frac{G_0 P_{in}}{4E_b/N_0} \tag{2.3}$$

Next, the receiver is assumed to be perfectly synchronized. Using FFT, received time domain samples are translated to the frequency subcarriers domain. Pilot carriers and guard bands are removed. The obtained data subcarriers are compared with those transmitted. The overall symbol error rate (SER) can then be calculated from the errors made: assuming

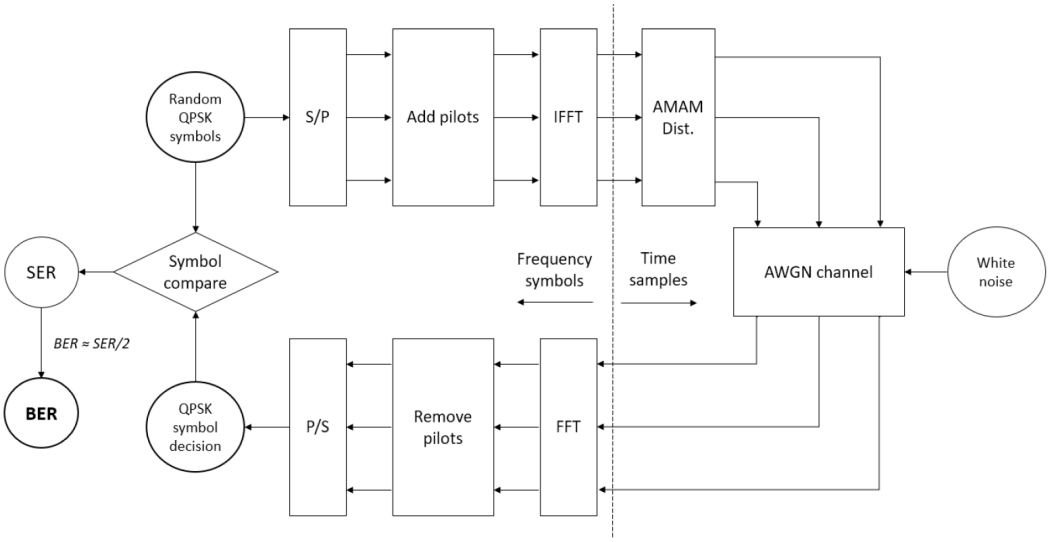

Figure 2.3: AMAM degradation simulation setup.

Gray coding and, a sufficiently low noise level and QPSK modulation, BER can be calculated as $BER = SER/2$.

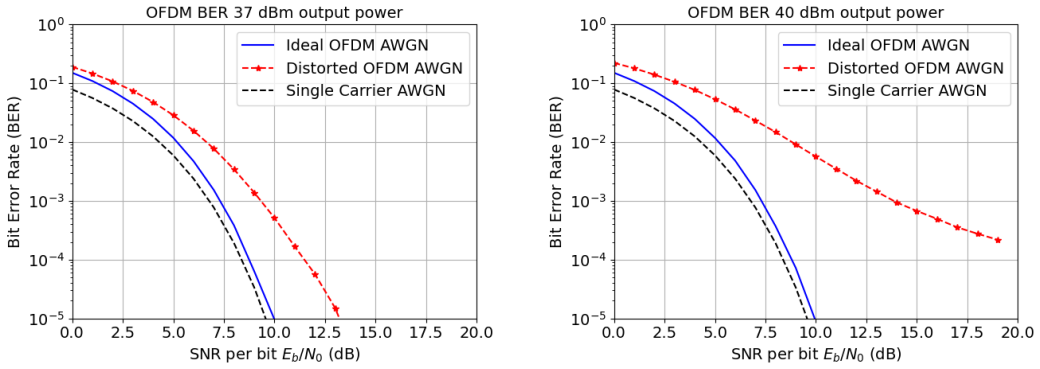

(a) (b)

Figure 2.4: BER simulation with AMAM distortion, with 37 dBm output mean power (left) and 40 dBm (right).

In table Table 2.3 the parameters used in the AMAM simulation are listed.

The simulated BER with respect to E_b/N_0, at 37 dBm and 40 dBm output mean power, is shown in Figure 2.4. In botses the BER curve related to the distorted signal is shifted towards higher E_b/N_0. In the 40 dBm case a plateau on the BER graph is showing that for high E_b/N_0 the overall noise is no longer dominated by AWGN, the highest noise contribution is due to the AMAM distortion instead. Assuming a target BER of 10^{-4} and computing the distance between the blue and red curve shown in Figure 2.4 for different values of OBO, it

FFT size	256
Data subcarriers	203
Pilot subcarriers	7
Guard subcarriers	23
Subcarrier spacing	30 kHz
Channel bandwidth	7680 kHz
Data bandwidth	6090 kHz
Guard band	690 kHz

Table 2.3: AMAM degradation simulation signal parameters.

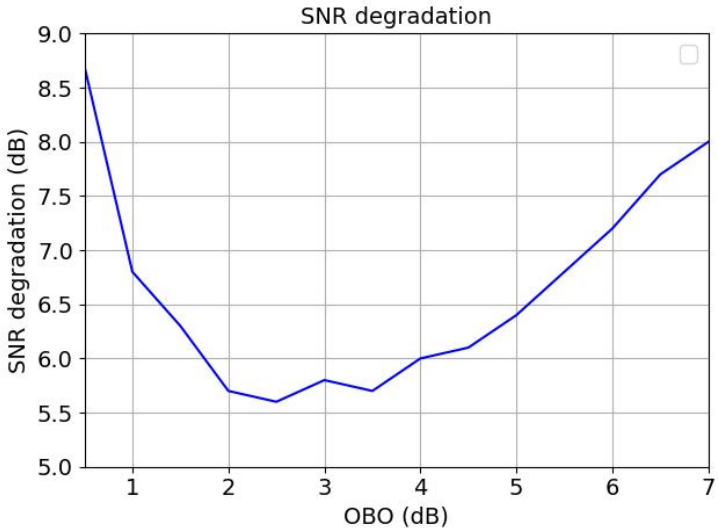

Figure 2.5: SNR degradation due to AMAM.

is possible to compute the SNR degradation as shown in Figure 2.5. For decreasing OBO the degradation rises rapidly due to AMAM distortion, while for increasing OBO the SNR degradation is due to the lower power delivered by the PA. In between it is possible to define the best OBO for the selected simple OFDMA waveform which is 2 dB to 3 dB.

An analysis on the phase noise added by the transponder was carried out. A similar approach as in Figure 2.3 was used, with a simulation block that adds phase noise according to a spectrum mask, in place of the AMAM distortion block. With this simulation setup the maximum phase noise mask was defined according to Figure 2.6. The phase noise mask values were computed empirically by checking when the SNR degradation is over 0.5 dB. The payload added phase noise is, however, way below this threshold and its effect on BER is negligible.

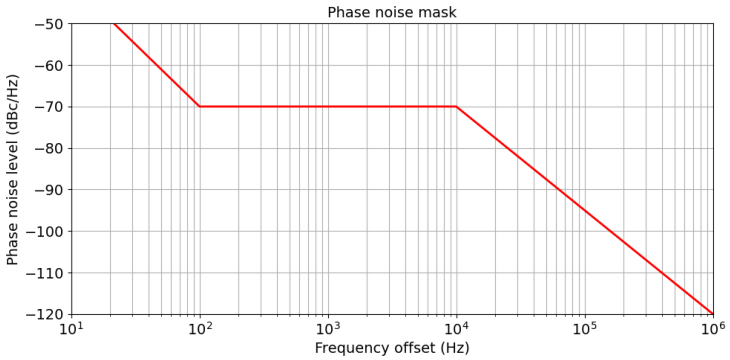

Figure 2.6: Phase noise mask defined for the scenario in Table 2.3

2.3 Frequency offset analysis

In a OFDMA system, time and frequency synchronization are essential. Carrier frequency offset (CFO) is the residual shift in the carrier frequency of the received signal with respect to the expected actual frequency. Its presence affects the orthogonality of OFDMA subcarriers increasing the iinter-carrier interference (ICI), which in the end can also lead to a failure in the synchronization between gNB and UEs. Mitigation of CFO is approached considering the static offset introduced by frequency conversions, and dynamic offset, caused by Doppler shift. The static offset induced by reference clock precision can be computed according to the formula $CFO = \pm CFO_{ref} f_{LO}$, with f_{LO} oscillator signal used by the up/down converter stage and CFO_{ref} its precision in ppm. For instance, for a LO signal at 24 GHz, generated from a 0.01 ppm reference TCXO, a static frequency offset in the range ±290 Hz can be expected. If two frequency conversion stages are synchronized, i.e. their relative PLLs share the same reference oscillator source, they will share the same relative frequency error as well. Synchronization is useful in a transceiver for which the RF signal should transit in down and then up conversion stages. In this case the sign of one conversion stages is the opposite to the other, assuming upper side-band conversion. In up-conversion $f_{RF} = f_{IF} + f_{LO}$, while in down-conversion $f_{IF} = f_{RF} - f_{LO}$. The opposite sign of $f_{LO} = f'_{LO} + f_{err}$ in the two cases implies that in one f_{err} is positive while in the other is negative. As a result, with f_{UP} and f_{DWN} uplink and downlink carrier frequencies respectively, the static CFO added by a transparent transceiver is expressed in (2.4).

$$CFO = \pm CFO_{ref} \left| f_{UP} - f_{DWN} \right| \tag{2.4}$$

The LIDE mission was analyzed in terms of added CFO by system components. A simplified diagram showing the main conversion stages in the whole path from gNB to UE and back is shown in Figure 2.7.

As can be seen, SDRs, BUCs and BDCs share the same reference; therefore, their added

static CFO can be computed as in (2.4). The single satellite transponder can be treated in the same way. A SYNC cable was added in order to have a master transponder sharing its reference to the other slave transponder. Since the LIDE operating frequencies in K/Ka band for uplink and downlink are pretty close to each other, the added CFO of one transponder is almost the same as the other. During the design phase several CFO compensation strategies were considered. Among these the use of a beacon close to the pass band was proposed by the company responsible for the ground segment, and having both transponders introducing the same added CFO was beneficial for the CFO compensation by the UE. The assumption of this method was that the gNB would have been in the service downlink beam, with another SDR listening to the beacon relayed by the transponder. However, this method was considered unfeasable and cumbersome later on. Nevertheless, the SYNC cable connecting transponders remained in the designed payload.

The most suitable method for this purpose is at 5G physical layer level. ThegNB, instead of decoding the first PRACHs that receives from UE, uses those to compute the frequency error in the feeder downlink and calibrates its transmit frequency to compensate the CFO measured. Then the rest of the RACH sequence continues as usual. Furthermore, gNB compensates the Doppler shift in the feeder link from its position and ephemeris data contained in SIB19, which is then forwarded to the UE. On the other side, the UE compensates the Doppler of the service link from its position and the SIB19 data received by gNB. The residual CFO in the service downlink, after UE Doppler compensation, is forwarded to the service uplink path. The frequency error for SDRs, BUCs, BDCs and transponders references is assumed to be uniformly distributed in the range ± 0.1 ppm [78], with Doppler compensation frequency error with the same distribution as well. Considering the architecture in Figure 2.7 a CFO analysis was carried out in the following cases: S/N (payload synchronized / no PRACH compensation), N/N (payload not synchronized / no PRACH compensation), S/P (payload synchronized / PRACH compensation) and N/P (payload not synchronized / PRACH compensation). In the payload synchronized case the transponder has its receiver and transmitter stages with their own reference, while in the opposite case

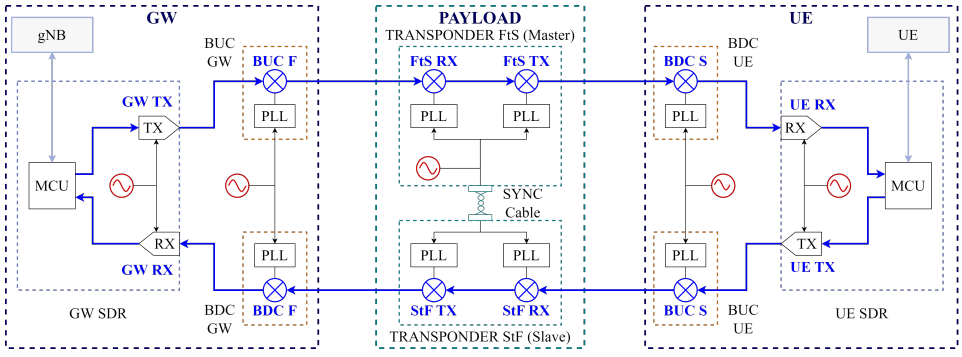

Figure 2.7: LIDE mission conversion stages.

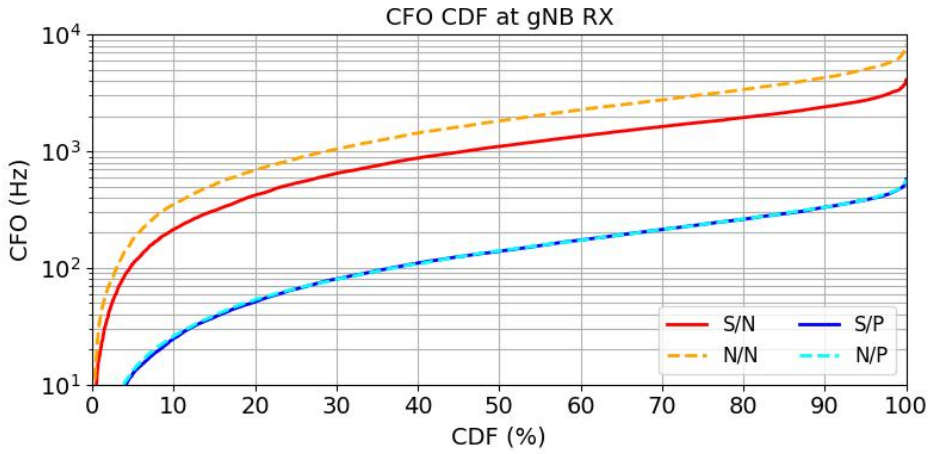

Figure 2.8: cumulative distribution function (CDF) of the added CFO in the following cases: S/N (payload synchronized / no PRACH compensation), N/N (payload not synchronized / no PRACH compensation), S/P (payload synchronized / PRACH compensation) and N/P (payload not synchronized / PRACH compensation).

the reference is shared. The added CFO is reported in terms of its CDF in Figure 2.8.

The residual CFO in the case without PRACH compensation is in the order of SCS (30 kHz), which can be problematic. The synchronization of the payload conversion stages lowers the added CFO by some kHz. However, the best improvement can be achieved with the PRACH calibration, leading to a residual CFO below 1 kHz. The synchronization of the payload is not improving the overall performances in this last case. However, the initial PRACH incoming at the gNB has a frequency error in line with the red or the orange curves (S/N, N/N cases), since no compensation is performed at that moment. In this sense, having the payload synchronized can reduce the search space around the wanted carrier frequency for the gNB trying to calibrate itself, with subsequent improvements in terms of precision and speed.

In [79] an analysis on OFDMA signal degradation induced by CFO is presented . This analysis is used to assess the effect of CFO in the presented work. The signal-to-noise-plus-interference ratio (SINR) parameter gives an estimate on the quality of the received signal, which takes into account the interference added noise induced by ICI, caused by CFO. It can be defined a worst case lower bound for the SINR for a received signal affected by a frequency offset ΔF, expressed as relative to the actual SCS $\epsilon = \Delta F / SCS$. The lower bound formula is expressed in (2.5) with respect to E_s/N_0, where E_s is the averaged received energy and $N_0/2$ is the AWGN power spectral density.

$$SINR \geq \frac{E_s}{N_0} \frac{\left(\frac{\sin(\pi\epsilon)}{\pi\epsilon}\right)^2}{1 + 0.5947 \frac{E_s}{N_0} \sin^2(\pi\epsilon)} \tag{2.5}$$

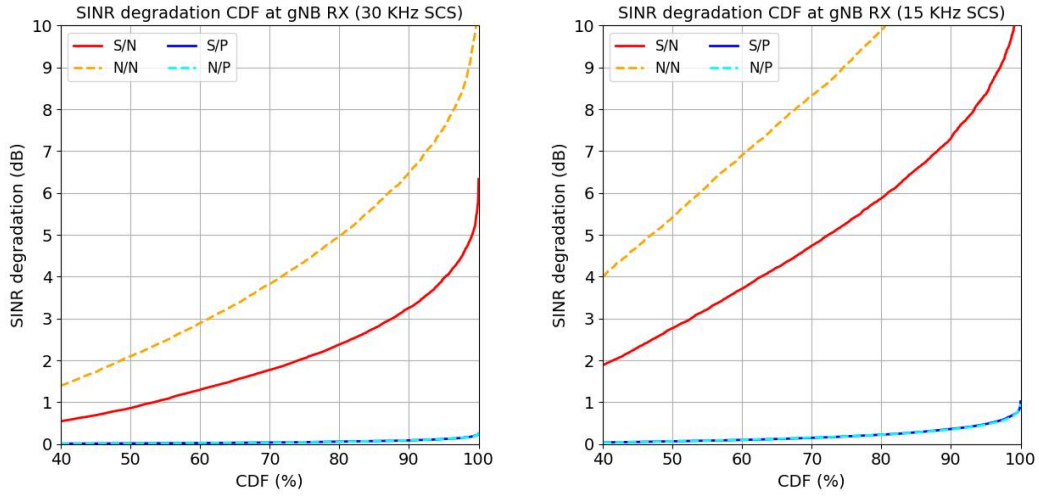

(a) (b)

Figure 2.9: CDF of the added SINR degradation induced by CFO for 30 kHz SCS (left) and 15 kHz (right). The following cases are considered: S/N (payload synchronized / no PRACH compensation), N/N (payload not synchronized / no PRACH compensation), S/P (payload synchronized / PRACH compensation) and N/P (payload not synchronized / PRACH compensation)

Starting from the CFO CDF reported in 2.8, the SINR degradation is computed as the ratio between E_s/N_0 and the worst case lower bound in (2.5). The final results are presented in 2.9, comparing 30 kHz and 15 kHz SCS cases, using the service downlink E_s/N_0 reported in 2.2 and equal to 14.6 dB.

In both cases it can be seen that the PRACH compensation leads to an almost negligible SINR degradation below 1 dB. For other CFO compensation techniques the degradation is quite relevant and is higher in the case of 15 kHz SCS, as expected. This analysis suggests that without PRACH based CFO compensation the proposed OFDMA satellite link is significantly affected for the 30 kHz SCS case and practically not feasible if 15 kHz is implemented as SCS instead.

Chapter 3

Transceiver Design

In this chapter are gathered some works performed during the PhD activity, related to the design of satellite transceivers. Only the works that had an outcome on scientific papers are presented. The design of Ka band receiver front-end is described with a focus on its integration in the transponder chassis. The design of an upconverter with low spurious emission is described as well, considering the ITU recommendations in matter of spurious emission. These two major thopics are not describing the whole transceiver design. The IF section between up and down converter is omitted in this chapter, because it is not of big interest in terms of research impact.

3.1 Payload architecture

A telecommunication payload must comprise an analog frequency conversion and amplification section, which are the transceivers in our case, controlled by a main on-board computer (OBC), which is then interfaced to the rest of the satellite platform. Antennas are then interfaced to the transceivers to transmit or received the wanted signals from ground or other satellite platforms in the case of ISLs. A transparent data relay comprises only the analog transceivers controlled by the OBC. On the other hand, a regenerative payload must integrate also a modem to modulate and demodulate signals transiting in it.

In the *radiosat/beamsat* IOD the non-regenerative bent-pipe transponder occupies a volume of 0.5 U and has a mass of 700 g. The complete satellite communication payload is reported in a simplified block diagram in Figure 3.1.

It features coaxial connectors for input from the receiving antenna and output to the transmitting antenna, along with a multi-pin connector for data and power interfacing with the OBC. Its gain is adjustable, thanks to an internal attenuator, within a 60 dB range, allowing operational flexibility. The internal attenuation can also be automatically adjusted with the automatic gain control (AGC) mode where, measuring the output power with a

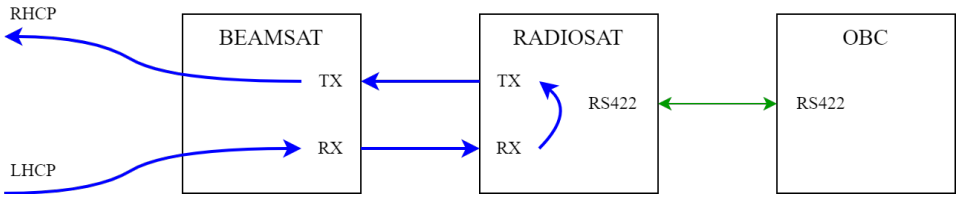

Figure 3.1: *radiosat*/*beamsat* IOD telecommunication payload main architecture. In blue the RF signal path from reception to transmission is shown, while the serial control interface in RS422 towards the OBC is shown in green.

detector, the power is maintained constant by adjusting the gain. In addition to bent-pipe operation, the transponder can generate a continous wave (CW) or GFSK modulated beacon [1].

The transponder's firmware is reprogrammable in orbit. It interfaces with the satellite's OBC via an RS422 connection. The transponders comprises two main boards: the receiver and the transmitter. The receiver board, which determines the noise figure of the entire system, and down-converts the signal, receives the uplink signal in the Ka band. The description of the LNA front-end is reported in [16]. The transmitter board up-converts the IF signal to the K band for data downlink. The transponder's output stage is a SSPA integrated into the transmitter section and can deliver up to 10 W of saturated RF power. The *beamsat* dual-band K/Ka band horn antenna is designed to be interfaced with *radiosat* at both its transmit and reception ports. It includes an orthogonal mode transducer (OMT), which isolates antenna transmit and reception ports and makes it possible to transmit and receive at two orthogonal polarizations, i.e., left-hand circular polarization (LHCP) or right-hand circular polarization (RHCP). It features a compact design with a volume of less than 2 U and a mass of 570 g.

The LIDE transponder is pretty similar to the one used in the *radiosat*/*beamsat* IOD, with two separate reception and transmission sections. The telecommunication payload in the LIDE mission comprises two transponders, each connected to a receive antenna in the Ka band and a transmit antenna in the K band. This architecture ensures isolation between the four data streams: Feeder uplink, Feeder downlink, Service uplink, and Service downlink. The general block diagram of the satellite payload is depicted in Figure 3.2. Both transponders share the same synchronization signal for their frequency synthesizers. One transponder acts as the Master: generating the 100 MHz synchronization signal for itself and the other, designated as the Slave transponder. An additional board, named SYNC, is used for sharing a precise 100 MHz reference signal for the transponder's frequency synthesizers. When the transponder is used as the Master, a digitally controlled TCXO is integrated into its SYNC board. The SYNC output is forwarded to the reception and transmit boards of the Matser transponder and also to the Slave transponder via a twisted-pair cable. The TCXO's oscillating frequency can be adjusted via an I2C interface, allowing for further

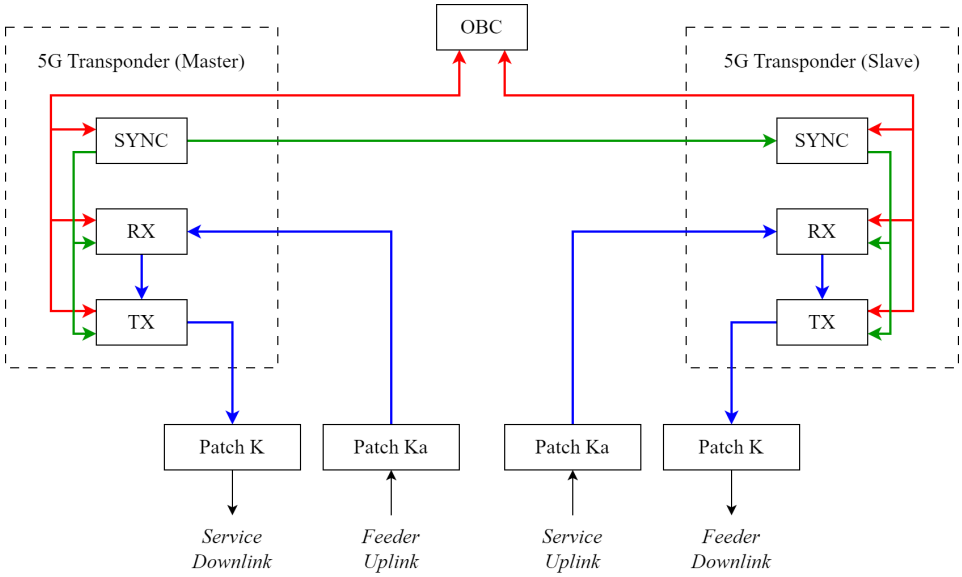

Figure 3.2: Block diagram of the LIDE telecommunication payload.

CFO mitigation during the device calibration phase. The RF signal paths are shown in blue, the 100 MHz synchronization signal in green, and the digital control lines for the communication with the OBC in red. The antennas are mounted on one aluminum satellite surface and connected via 2.92 mm harness cables to the transponders. A photograph of the payload transponder pair and the payload patch antennas are shown in Figure 3.3 Figure 3.4, respectively.

LIDE mission antennas are realized in printed circuit technology. Both K and Ka band antennas comprise an 8×8 array of circularly polarized patches in a nested architecture to enhance the axial ratio over the required bandwidth [80]. A SMP-type connector is placed on

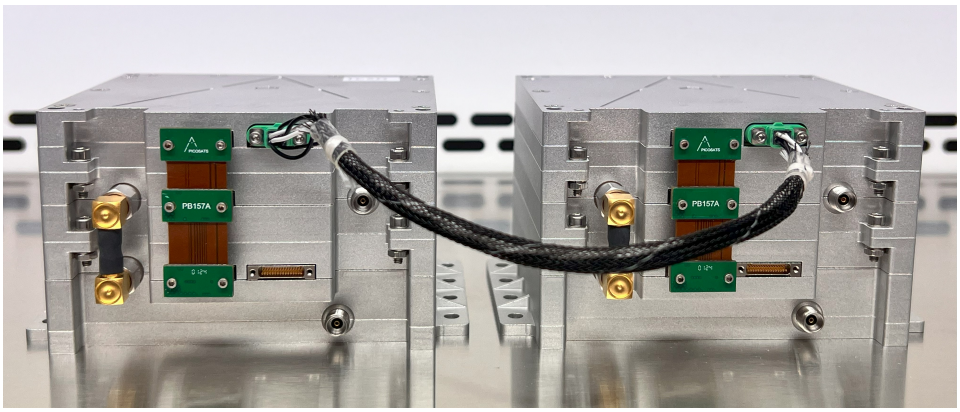

Figure 3.3: Flight model pair of LIDE transponders.

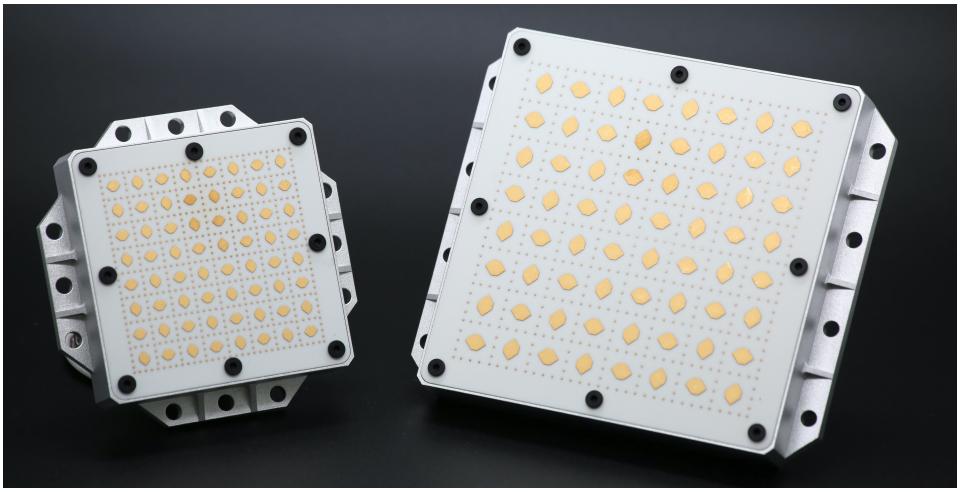

Figure 3.4: Photo of the Ka band antenna (left) and K band antenna (right).

the bottom layer of the PCB and connected to the feeding network, propagating the signal to the patch array on the top layer. To facilitate integration, they are designed together with an aluminum enclosure. This design allows the antennas to be easily bolted onto the satellite chassis without significant issues related to the coupling of feeding networks.

In the wideband transceiver design miniaturization is a key design parameter. In this case, the reception and transmission boards are all integrated in a single board. Furthermore, the printed circuit board (PCB) design ensures reconfigurability during components soldering phase. Components can be mounted on different arrangements on the same PCB layout. In this way, it is possible to manufacture a bent-pipe transponder with several values of analog bandwidth, or a regenerative transceiver by adding an IF output to the transceiver towards the external modem and another connector for the way back. This approach reduces by a significative amount the lead time for a component, since the PCB manufacturing time is way higher than the components soldering once. For this design an IOD is not yet scheduled.

3.2 Receiver front-end

The IOD and the 5G transponders shares a similar front-end architecture described in [16]. In this section the wideband transponder front-end is described. The goal of this new design was to shrink by a significative amount the dimensions of the front-end section in the PCB. The proposed circuit layout comprises a LNA and a band-pass filter, acting as image rejection filter for the following downconverter module. This latter component is out of the scope of this simulation and is an Analog Devices ADMV1014, which integrates another LNA in the first stage and a image rejection down-converting mixer. The first LNA and the band-pass

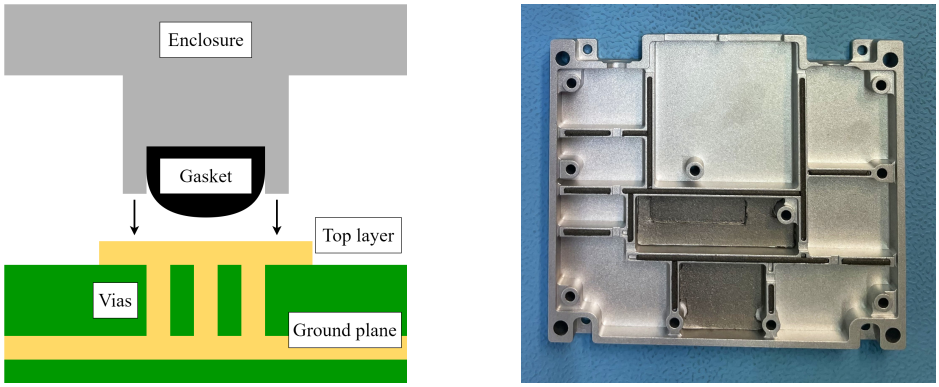

(a) Section of the enclosure shielding wall

(b) PCB enclosure

Figure 3.5: Block diagram of a section of shielding wall and a picture of an aluminium PCB enclosure, comprising cavities, gaskets and RF absorbing pads.

filter are placed on the PCB within an aluminum enclosure, which is the main chassis of the transceiver. This can lead to cavity resonances that can affect the behavior of the front-end. This is a phenomena that can happen also in other sections of the circuit. Furthermore, the insertion of the enclosure can affect the coupling between PCB sections. For example, coupling between the LO sections and the output amplification stage could increase LO leakage at the output port. This issue can compromise spectral quality, potentially leading to non-compliance with spurious emission masks [5]. The designed sections are intended to isolate the following functional blocks: the LNA section, PLLs, output driver stage, and IF gain blocks. The shielded PCB sections act as resonant cavities, with the PCB ground plane serving as the bottom conducting layer of the cavity. The enclosure walls are designed as shown in Figure 3.5, with a metallic wall in contact with the PCB through a conductive gasket.

Beneath it, a metallic exposed PCB track is filled with vias connected to the ground plane, extending the cavity wall within the PCB substrate. RF coplanar waveguide traces can enter the shielded cavity through rectangular openings in the wall. Other lines, such as power and digital signals, enter the cavity only through vias from other PCB layers. The circuit was simulated in CST Studio Suite, in a co-simulation setup that involves also Altium Designer for the PCB layout drawing. The cavity resonance modes frequencies of the structure can be computed according to (3.1)

$$f_{mnk} = \frac{c}{2\pi\sqrt{\varepsilon_r}}\sqrt{\left(n\frac{\pi}{a}\right)^2 + \left(m\frac{\pi}{b}\right)^2 + \left(k\frac{\pi}{c}\right)^2} \tag{3.1}$$

A list of resonant cavity frequencies in the proximity of the receiver bandwidth 27.0 GHz to 31.0 GHz for the receiver front-end section is reported in Table 3.1. As can be seen, more than one resonance frequency is within the receiver bandwidth.

Resonance frequency	Order X (24.5 mm)	Order Y (8.2 mm)	Order Z (5.0 mm)
25.92 GHz	3	1	0
30.00 GHz	0	0	1
30.56 GHz	4	1	0
30.61 GHz	1	0	1
32.40 GHz	2	0	1

Table 3.1: Cavity resonance frequencies in the proximity of the receiver bandwidth 27.0 GHz to 31.0 GHz.

The simulation is then performed by drawing the front-end layout in Altium Designer, with signal traces, ground planes, vias and the selected substrate. Only the first two layers of the PCB were defined (top layer and ground plane), since they are reserved for the RF signal traces and are well separated from the other layers, in which digital and other signals at lower frequencies are present. The Altium layout is then exported in CST Studio Suite for the simulation. The metallic enclosure is then added on top of the PCB. In this environment simulation ports are added in the PCB 3D model and a frequency-domain simulation was set up. A section of the simulated structure is reported in (cite). The simulation S-parameters are then exported as a .sxp file, and placed in a circuital block connected to other blocks modeling the LNA and the band-pass filter.

The structure was analyzed also by changing PCB components spacings, between each other and from components to enclosure, and the size of the metallic enclosure. Even though it is possible to slightly move resonances across the receiver bandwidth, none of the simulated cases was satisfactory. Therefore, the insertion of a RF absorber pad on the ceil of the enclosure was necessary. The selected pad is the Laird Eccossorb GDS. This latter component was added in the simulation as well.

A evaluation board (EVB) of the proposed front-end was designed and manufactured. A picture of it is reported in Figure 3.6.

The final comparison was performed between the following cases: the front-end without the metallic enclosure, the addition of the metallic enclosure and the complete system comprising also the RF pad. S11 and S21 plots regarding this comparison are reported in Figure 3.8.

Simulations shows that the insertion of the RF pad is necessary since at resonant freqencies the system appears to be unstable, with S11 peaks over 0 dB. The insertion of the RF pad makes results somewhat similar to the case without enclosure, which is what it is wanted. Measurements of the complete system are satisfactory and shows an S11 below -12 dB and a gain over 18 dB over the required signal bandwidth 27.0 GHz to 31.0 GHz. Regarding the comparison with measurements, there is a major error in each case around the resonant frequency at 30 GHz. Furthermore, the S11 peaks over 0 dB are not present in measurements. All this aspects shows that the simulation should be improved for bet-

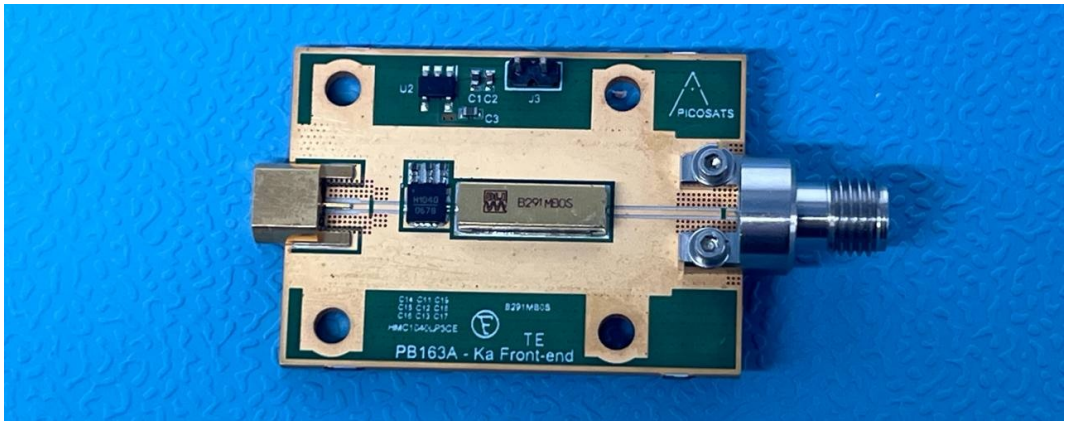

Figure 3.6: Photo of the manufactured front-end EVB.

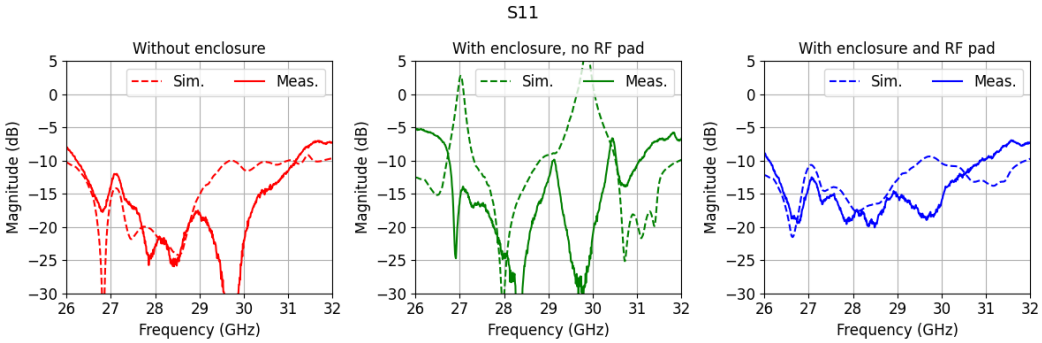

Figure 3.7: S11 comparison between simulation and measurement for the selected case of study.

ter modeling the cavity resonances. Another aspect not present in the simulations is the decrease of gain (S21) in the case without the RF pad. However, the final result was considered satisfactory and no further analysis were made. Noise figure is a key parameters in front-ends, but was not measured in this phase due to lack of instrumentation.

Regarding other PCB sections, if the computed resonant frequencies are above the operating signal bandwidth, then they can be considered not an issue. For instance, in the IF section, in which signals below 6 GHz are transiting, a cavity resonance at 20 GHz could not be an issue if the RF chain path is well filtered. In the proposed design resonances were unavoidable near the PLLs. In this case, an empirical approach was adopted: if resonances effects were detected during transceiver normal operation, an RF absorber layer was added to the upper face of the shield. This solution damped all the detected resonances in PLLs sections.

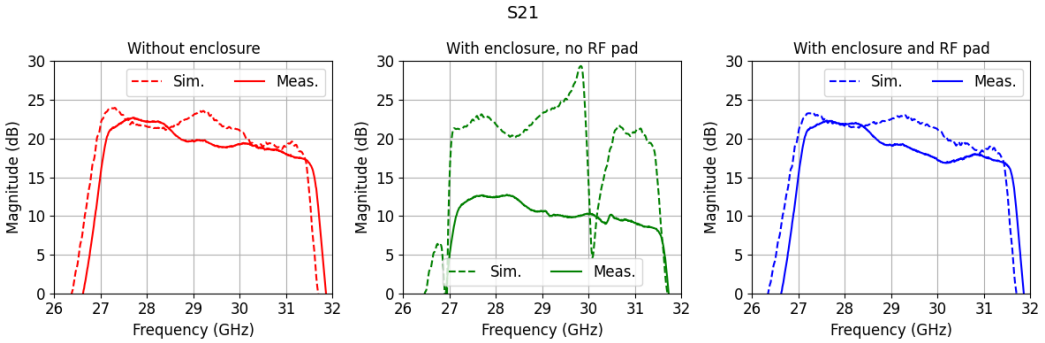

Figure 3.8: S21 comparison between simulation and measurement for the selected case of study.

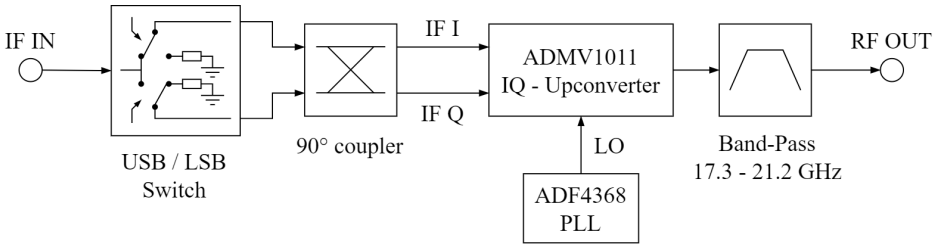

Figure 3.9: Upconverter schematic.

3.3 Up-converter design

In this section an upconverter architecture for 17.3 GHz to 21.2 GHz FSS and IF frequency up to 4 GHz is proposed and validated with a focus on spurious emissions. To increase spurious rejection, upper side-band (USB) and lower side-band (LSB) frequency conversion modes are combined, and LO leacage reduction techniques are used. The proposed architecture is validated in terms of spurious-free dynamic range (SFDR) on a preliminary set-up, realized through the interconnection of adopted EVBs. The upconverter is finally connected to a 10 W PA. Spurious emission of this latter test set-up is compared with ITU recommendations, to assess the feasibility of the system to be integrated in LEO satellite telecommunication equipment. error vector magnitude (EVM) for a 16-APSK modulated signal with 10 MHz symbol rate was finally measured to characterize the complete system.

3.3.1 Upconverter Architecture

The complete upconverter architecture is reported in Figure 3.9. The main component of the system is the Analog Devices ADMV1011: an in-phase/quadrature (I/Q) integrated upconverter with x2 frequency multiplier in the LO-chain and a RF output driver amplifier. To improve LO leakage rejection, LO-nulling can be performed by changing the bias of the I/Q

Table 3.2: ITU spurious emission mask for FSS in the proposed scenario.

Region	**Mask**
Out-of-band domain	$40\log(F/50+1)$ dBsd
Spurious domain	$43+10\log(P)$ or 60 dBc, whichever is less stringent

mixers [81]. The LO signal for ADMV1011 is generated by the Analog Devices ADF4368 PLL, with controllable output power level. The ADMV1011, together with a 90° coupler, is used as an image rejection mixer (IRM) [82], [83]. A non-reflective single-pole-double-throw (SPDT) switch is used to select the USB or LSB output spectrum component, by feeding the IF signal in one of the two input ports of the 90° coupler and terminating the other one on a matched termination. The RF signal is filtered in the desired band by a 17.3 GHz to 21.2 GHz transmit channel band-pass filter. Compared to single USB operation, the combination of USB and LSB modes shifts the LO leakage frequency further from the pass-band of the transmission channel filter, thereby enhancing the rejection of LO leakage. The proposed upconverter allows for an IF frequency from 0 to 4 GHz. However, in a FSS scenario, the output spectrum might not comply with ITU spurious emission recommendations across the entire 2D plane defined by RF and IF frequencies.
The ITU regulations [84] divide the unwanted emission spectrum into two main sections: out-of-band domain [85] and spurious domain [86]. Considering the modulated test signal used for the upconverter characterization, described in the following sections, the out-of-band domain extends 2.5 MHz beyond the edges of the main allocated signal bandwidth. In Table 3.2 the spurious emission mask is reported, with F as the frequency offset from the boundary of allocated signal bandwidth, dBsd decibels relative to the maximum value of power spectral density within the allocated bandwidth, P average power supplied to the antenna transmission line, and dBc decibels relative to the unmodulated carrier power of the emission. The reference bandwidth for spurious emission measurement should be 4 kHz.

3.3.2 Measurement set-up

Measurement set-up was composed of EVBs of the components described in Figure 3.9. The USB/LSB switch was modeled by combining the results of USB and LSB modes in post-processing. A spectrum analyzer Rohde & Schwarz FSW was used for the measurement of spurs. Resolution bandwidth was set to 4 kHz, as specified in [86] for spurious domain characterization. A 16-QAM 100 MHz modulated IF signal was generated by a signal generator Rohde & Schwarz SMW200 and forwarded to the system under test. The main measured parameter was the SFDR, which is defined as the magnitude ratio between the unmodulated

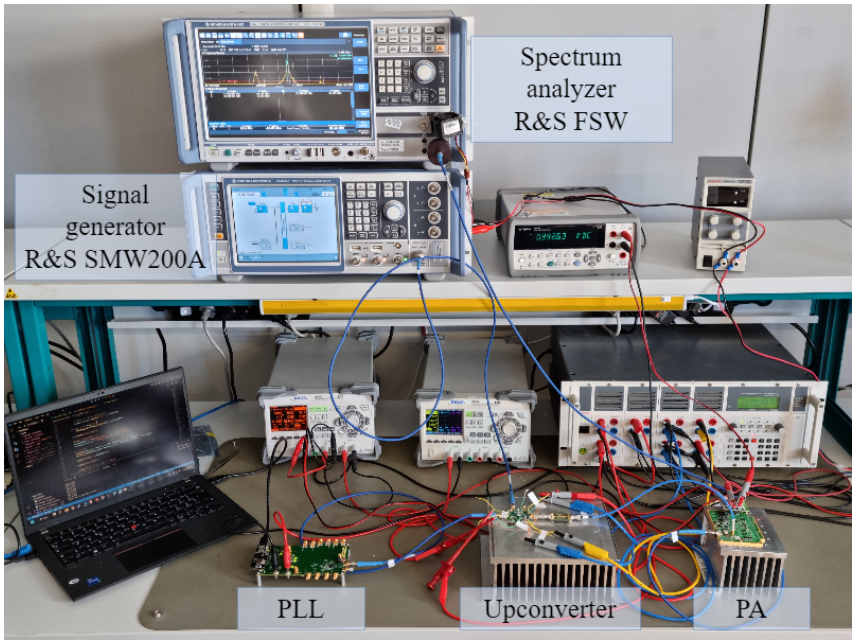

Figure 3.10: Test set-up with upconverter and 10 W power amplifier.

carrier and the most powerful spur in the modulated scenario. SFDR is therefore reported in dBc. Spurious emission was evaluated in the range 14 GHz to 25 GHz. Unmodulated carrier power was measured in a CW test for all the RF-IF frequencies, prior to modulated SFDR measurement. The proposed set-up emulates a more realistic scenario compared to a single-tone CW measurement, where third-order intermodulations are not considered. Moreover, a test with a modulated input signal enables the differentiation between spurs influenced by modulation in terms of spectral density and those that are not, such as LO leakage and its harmonics, whose spectral density remains independent of the symbol rate. To assess the compliance with ITU recommendations, the upconverter was connected to a 10 W power amplifier, which is limited in the 17.3 GHz to 20.2 GHz bandwidth; therefore, in this case, measurement were repeated with the narrower bandwidth. To ensure a sufficient back-off from saturation, output power of the power amplifier was limited to 5 W. In Figure 3.10 the complete test set-up is shown.

3.3.3 Test Results

In this section, the following results are presented: (i) the SFDR of the upconverter across the entire FSS bandwidth for the IF band 1.5 GHz to 4 GHz without LO-nulling, and a comparison of SFDR with and without the LO-nulling for a fixed 3.2 GHz IF frequency, (ii) measurement of ITU spurious emission mask margin of the upconverter connected to a 10 W power amplifier, without LO-nulling, and (iii) 16-APSK, 100 MHz symbol rate, constellation

and EVM for sample IF and RF frequencies; with 36 dBm of mean output PA power.

In Figure 3.11 the SFDR in USB mode (Figure 3.11a), LSB mode (Figure 3.11b), and combined mode (Figure 3.11c) are reported. The used RF-IF frequency threshold is added on the graph, which is the separation line in the 2D RF-IF frequencies plane between the two side-band operating modes. LO-nulling was not applied in this case and PLL power was set at a fixed value. The main unwanted spurs are 2LO and 3LO, which are not affected by modulation and appear on the output spectrum as tones. The 2LO spur effect on SFDR can be seen where SFDR plot is clearest: in the upper-right part of USB mode plot and in the upper-left of LSB mode; while 3LO causes a SFDR degradation in the bottom-left of USB mode.
By adding LO-nulling and controlling the PLL output power, it is possible to lower the LO leakage and its harmonics. As an example and demonstration of such an improvement, the SFDR for a 3.2 GHz IF frequency is reported in Figure 3.12 with and without these adjustments. Since the RF bandwidth is wide enough to have the 3LO spur in the pass-band of the transmitter channel filter, the spur rejection can be enhanced only by adjusting the non-linear performances of the system with LO-nulling. The use of switchable filters can be another viable solutions, as proposed in [87] for a Ku band receiver, though with the trade-offs of lower system integrability and higher costs.

Finally, in Figure 3.13 the results of the test of the upconverter with 10 W power amplifier are shown. The reported parameter is the margin relative to the mask of Table 3.2. Spurious signals within the ITU spurious domain were measured in dBc, while in the out-of-band domain in dBsd: which is the power ratio between the main RF signal and spur peak, both measured with the same modulated input signal. As in the previous section, ITU margin is reported for USB mode (Figure 3.13a), LSB mode (Figure 3.13b), and combined mode (Figure 3.13c). In this case the RF-IF frequency threshold was fixed for every IF frequency at 19.1 GHz RF frequency. Since the spurious emission margin is high enough, a simple RF-IF threshold profile was selected. The LO-nulling was not applied in this case. In Figure 3.14 a detail of ITU spurious mask margin is shown for different IF frequencies.
The area defined by RF frequency 17.3 GHz to 17.7 GHz and IF frequency 3.6 GHz to 4.0 GHz has a non-compliant spurious mask margin due to the presence of 3LO spur in USB operating mode.

The complete system (upconverter and 10 W PA) was finally evaluated in terms of EVM and quality of a 16-APSK constellation, with 100 MHz symbol rate. Mean output PA power was set to 36 dBm. In Table 3.3 16-APSK constellations with relatives EVM are shown, for sample IF frequencies 2.5 GHz, 3.2 GHz and 4.0 GHz and RF frequencies 17.5 GHz and 20.0 GHz. For the RF frequency 17.3 GHz USB mode was used; on the other hand, for 20.0 GHz LSB mode was used instead. Measured EVM ranges between 3.41 % and 6.75 %

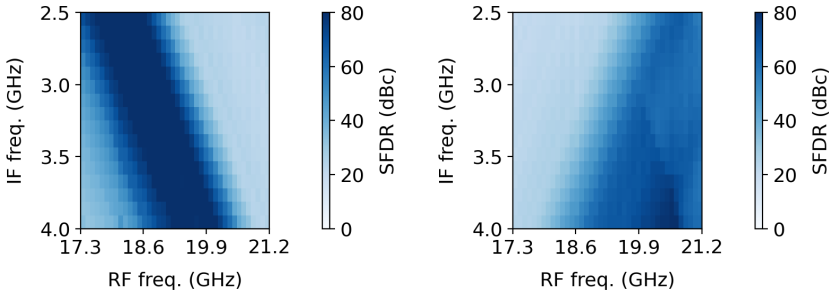

(a) USB mode.

(b) LSB mode.

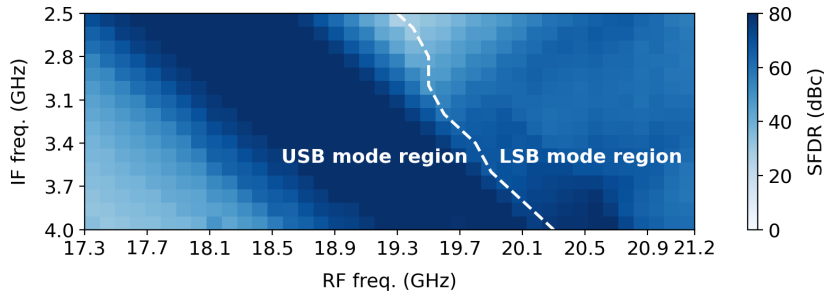

(c) USB-LSB combined mode.

Figure 3.11: Upconverter SFDR in the side-band operating modes.

for the presented cases. The main reason for the degradation of EVM, expecially at 20.0 GHz RF frequency, is due to the lower saturation power of PA at this frequency, which translates in a less OBO, hence, in a lower linearity caused by compression distortion [88].

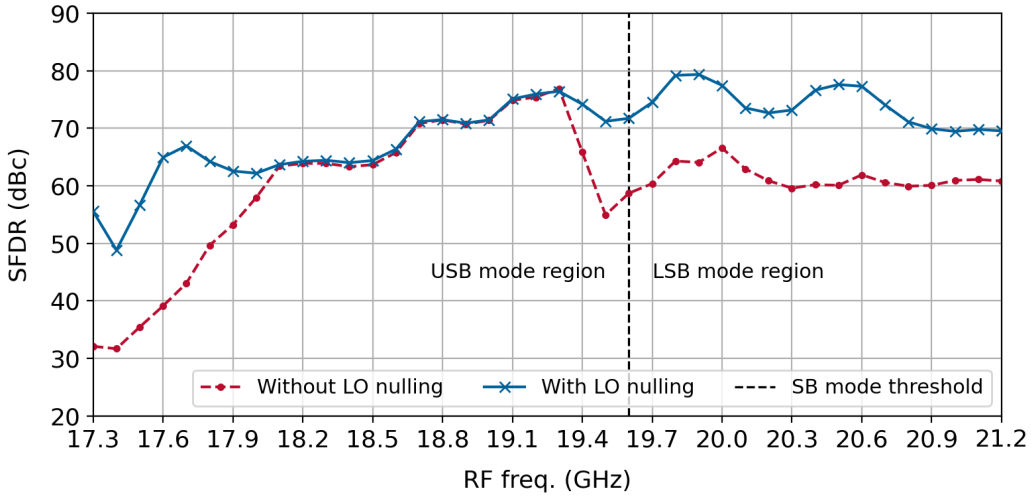

Figure 3.12: Upconverter SFDR at 3.2 GHz IF frequency with and without the LO-nulling and PLL output power adjustment.

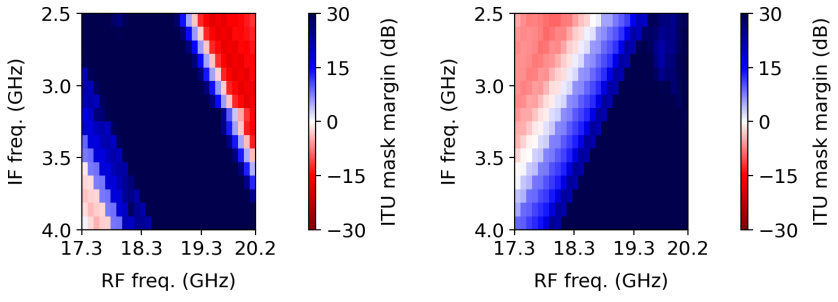

(a) USB mode.

(b) LSB mode.

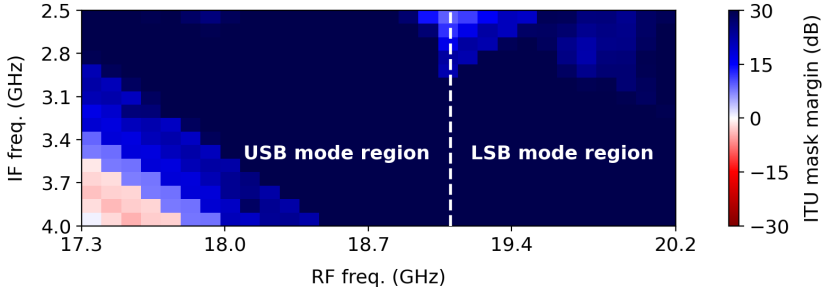

(c) USB-LSB combined mode.

Figure 3.13: ITU spurious mask margin in USB/LSB modes.

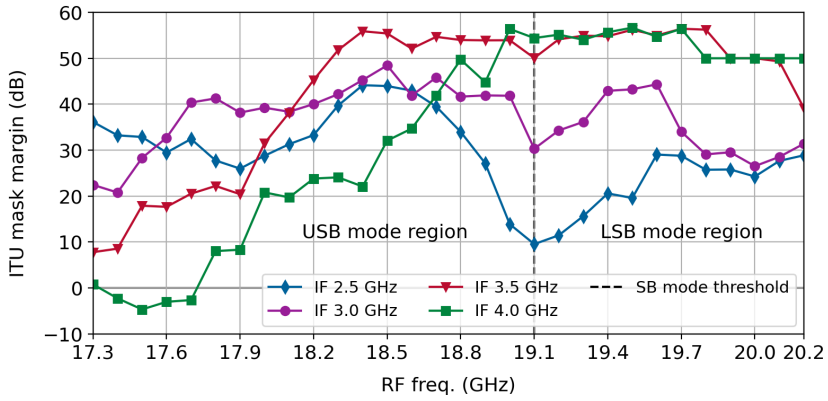

Figure 3.14: ITU spurious mask margin at various IF frequencies.

Table 3.3: 16-APSK constellation, 100 MHz symbol rate, measured with 36 dBm mean output PA power.

RF frequency:	17.5 GHz	20 GHz
IF frequency 2.5 GHz	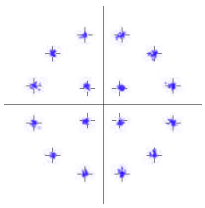	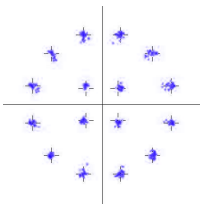
EVM:	4.16%	5.37%
IF frequency 3.2 GHz	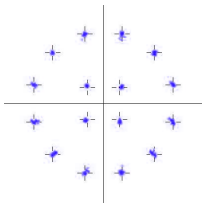	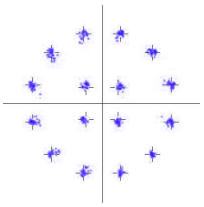
EVM:	3.41%	5.50%
IF frequency 4 GHz	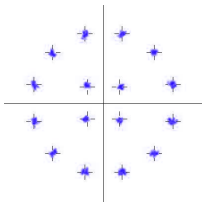	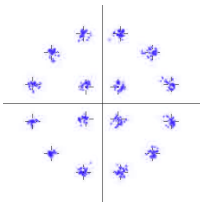
EVM:	3.87 %	6.75%

Chapter 4

Testing

In this chapter, the testing activities carried out during this work are presented. As in the previous chapters, the content is organized around the main projects developed throughout the study. The LIDE payload went through a qualification campaign, which is briefly described below. At the time of writing, the improved FSS K/Ka-band transceiver has been manufactured but not yet sufficiently tested; for this reason, it is not included in this chapter. Two 5G NTN testbeds, developed in the context of the LIDE mission, are described. In the first testbed, both the design and the final performance are presented, while in the second only the design is reported, as the project is currently on standby and scheduled to continue in November. The first setup was primarily constrained by the availability of test components and aimed at demonstrating the compatibility between the ground and space segments. The second setup focuses mainly on the space payload as the device under test, making it of greater technical interest than the first for the purpose of this study. The results of the *radiosat* and *beamsat* IOD campaigns are also presented, along with the design of the corresponding test schedules. This activity achieved highly positive outcomes: all functional tests were successful, and, as a final demonstration, an image of Earth was transmitted to the ground, proving the full functionality of the satellite payload. Finally, the LIDE IOD is presented. The satellite was successfully deployed on 24/07/2025, but full ITU licensing was only granted in September; therefore, this document reports preliminary test results only.

4.1 Payload qualification

In the final phase prior the deployment of a satellite mission the designed component should be verified. A picture of the payload under environmental test campaign (EVT) is shown in Figure 4.1, with antennas mounted on the satellite structural mock-up and the transponder hosted on the shaker during vibration tests. The objectives of the verification process are as follows:

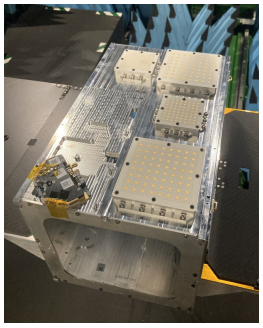

(a) Satellite structural mock-up with K and Ka band antennas

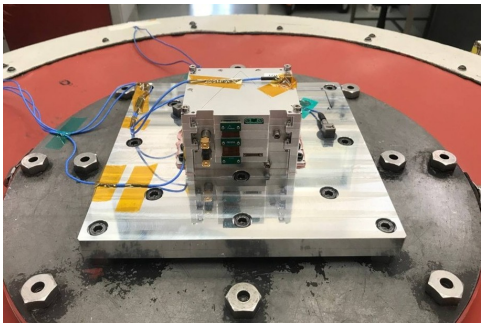

(b) Transponder on the shaker during vibration tests

Figure 4.1: Payload main components during EVT campaign.

- to demonstrate the qualification of design and performance, as meeting the specified requirements at the specified levels;
- to ensure that the product is in agreement with the qualified design, is free from workmanship defects and acceptable for use;
- to confirm product integrity and performance at particular steps of the project life cycle (e.g. launch, commissioning, mission events and landing).

The model philosophy is the definition of the optimum number and the characteristics of physical models required to achieve confidence in the product verification with the shortest planning and a suitable weighing of costs and risks [89]. More replicas of the design were manufactured: the proto flight model (PFM), the engineering qualification model (EQM), and the spare model (SPM). The PFM is the flight end product on which an acceptance test campaign is performed before flight. For this device, the objective of tests is demonstrating that the product is free of workmanship defects, is in accordance with the qualified design and is ready for its intended use. The EQM is an exact replica of the PFM and is intended to be tested more extensively according to the qualification campaign. This verification stage has the objective to demonstrate the design, ensuring that it satisfies the applicable requirements including proper margins. This testing philosophy is applied to get sufficient data to ensure that the designed PFM can withstand the operative scenario, and at the same time, to not stress it twice at the qualification campaign stage and during the flight. For some applications, EQM tests can also be destructive. The SPM is another device which can be promoted to PFM if unexpected issues may occur during the testing phase of the actual PFM.

In the LIDE mission development, the EQM payload went through an EVT, comprising thermo-vacuum chamber (TVAC) tests with 4 cycles in the range $-15\,^{\circ}\mathrm{C}$ to $50\,^{\circ}\mathrm{C}$ with $1\,^{\circ}\mathrm{C\,min^{-1}}$ slope, and vibration tests (quasi-static load, random and sine on each axis) [89].

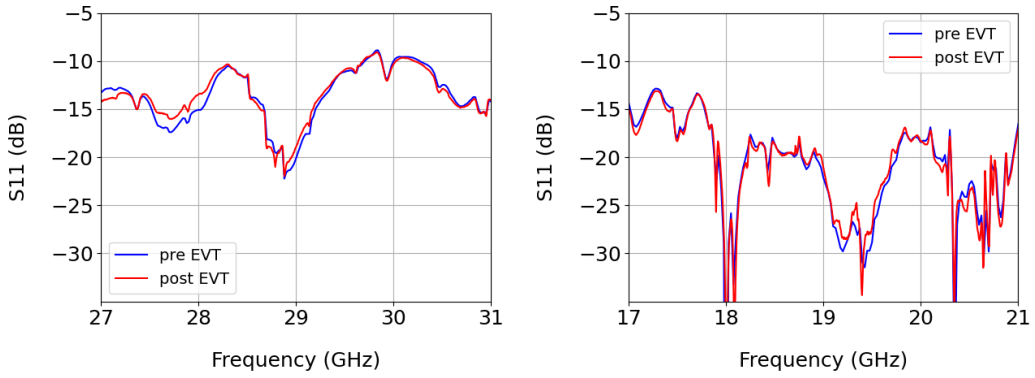

(a) Ka band antenna (b) K band antenna

Figure 4.2: S11 comparison before and after qualification campaign

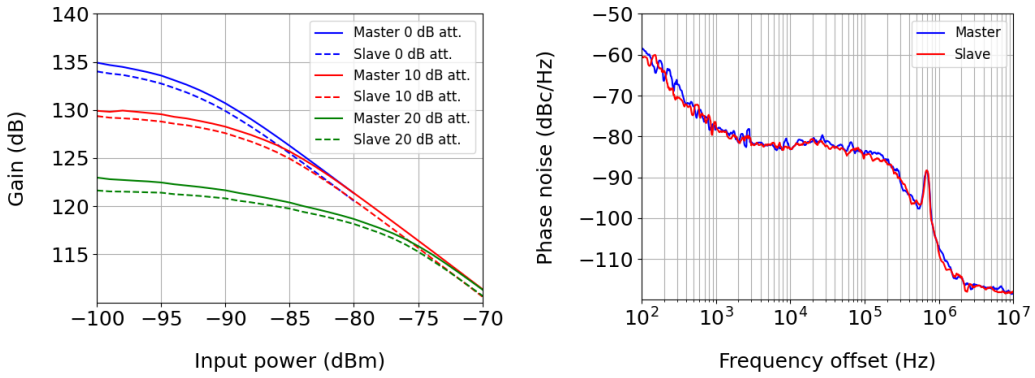

(a) Large signal gain (b) Phase noise

Figure 4.3: Transponder key parameters after EVT.

EVT antennas were checked by visual inspection and by comparing S11 parameters before and after EVT, as shown in Figure 4.2. Since there is no performance degradation in terms of S11, antennas were mounted on the satellite structural mock-up and their radiation diagram was measured in anechoic chamber (not shown in this document).

In Figure 4.3, transponder large signal gain and phase noise are shown after EVT. Furthermore, telemetry was queried to the device under test every 5 °C to check proper operation. The receiver noise figure was not measured at this stage; however, in the work presented [16] a measurement of the same receiver front-end design of the transponder under test is described.

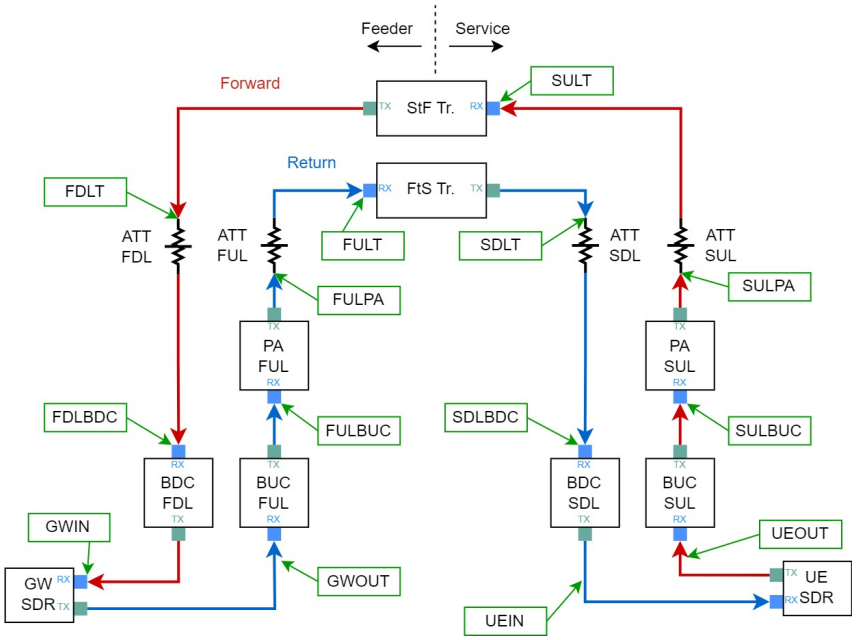

Figure 4.4: First 5G test setup, with components and node labels (in green boxes).

4.2 5G testing

The EQM transponder pair was also used to assess compliance with the ground equipment and the 5G deployment (after EVT). In this document two test setups are described: in the first one most of the ground segment of LIDE is interfaced with the space segment, while in the second one only transponders are used as the device under test with a laboratory channel emulator and frequency converters.

4.2.1 5G NTN test setup 1

In the first setup, described in Figure 4.4, two SDRs were used for the UE (UE SDR) and for the gNB (GW SDR) terminals, each equipped with a 5G software radio stack incorporating NTN adaptations from Rel. 17 [63].

The main goal was to test, in one solution, the space telecommunication payload, ground segment power amplifiers, BUCs and BDCs, using the selected Amarisoft software radio stack. Given the available components to set up the testbed, testing all the components and ensuring power levels and SNR similar to the operative scenario is challenging. In the following, an analysis of the testbed is shown. The designed ground BUCs (BUC feeder uplink (FUL) and BUC service uplink (SUL)) and BDCs (BDC feeder downlink (FDL) and BDC service downlink (SDL)) were included in the setup, along with fixed attenuators (ATT SDL, ATT FDL, ATT SUL, and ATT FUL). The transponders were integrated into the setup in place of the space segment (StF Tr. and StF Tr.). Ground power amplifiers

were included in the satellite uplink paths (PA FUL and PA SUL).

Doppler and latency effects are introduced within the Amarisoft software radio-stack emulator at the gNB side and compensated at the UE side. Even though this is not as relevant as a test where impairments are added with an external channel emulator, it is sufficient to check whether transponders are introducing impairments that could degrade the link. Furthermore, the SNR at the UE and gNB sides is higher than what is estimated by the link budget. This is due to the limited availability of fixed attenuators, which were introduced to ensure that signal levels at the input of devices are within a safe range, rather than to reproduce the operative case path attenuation. The achieved SNR can be computed considering the noise figure and gain of each device in the test chain, as described in Algorithm 1.

Algorithm 1 Procedure for test-bed SNR analysis, using the following parameters: P_{IN} test-bed input power, B channel bandwidth, k Boltzmann constant, T_0 IEEE standard noise temperature, G_{tot} total test chain gain, F_{tot} total test chain noise figure, S output signal level, N output noise level and SNR output SNR. This pseudo-code computes just the output of the whole test chain. To get a plot like Figure 4.5 S, N and SNR are saved for each component in the test chain and then plotted on a graph.

for component **in** chain **do** ▷ loop through components in the test chain
  if component **is** first **then** ▷ if the component is the first in the test chain
    $F_{tot} \leftarrow F_{component}$ ▷ get component noise figure
    $G_{tot} \leftarrow G_{component}$ ▷ get component gain
    $S \leftarrow P_{IN}$ ▷ update S as the test-bed input power
    $SNR \leftarrow S/(kT_0B)$ ▷ consider thermal noise floor
  else
    $F_{tot} \leftarrow F_{tot} + (F_{component} - 1)/G_{tot}$ ▷ two stages Friis formula
    $G_{tot} \leftarrow G_{tot} \times G_{component}$ ▷ update total gain
  end if
  $S \leftarrow S \times G_{tot}$ ▷ update component output power
  $SNR \leftarrow SNR/F_{tot}$ ▷ update component output SNR
  $N \leftarrow S/SNR$ ▷ update component output noise
end for
return $G_{tot}, F_{tot}, S, N, SNR$

In Figure 4.5, the results of this analysis are shown in terms of signal and noise power levels across the test chain. It is worth noting that the link power level can be controlled through the input power from the SDRs and the transponders' variable gain. These two degrees of freedom are not sufficient to ensure that, in the testbed, power amplifiers and transponders operate at the selected output power back-off while, at the same time, the SNR at the far-end SDRs inputs is consistent with the link budget. As can be seen from Figure 4.5, the SNR at the input of the far-end SDRs (UEIN or GWIN nodes) depends mainly on the first uplink attenuator and the transponder noise figure.

There is a significant drop of SNR between nodes FULPA–FULT and SULPA–SULT, due to the first fixed attenuators (ATT FUL and ATT SUL). Then, there is a slight drop of

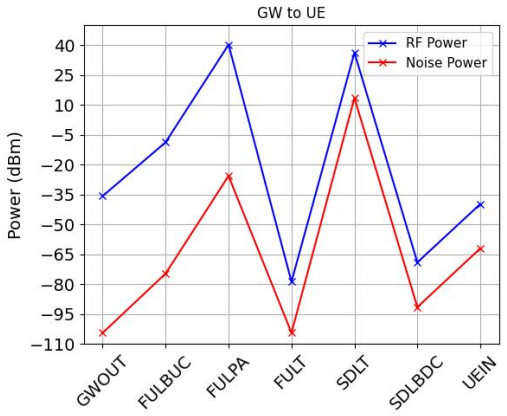

(a) GW to UE signal and noise power levels

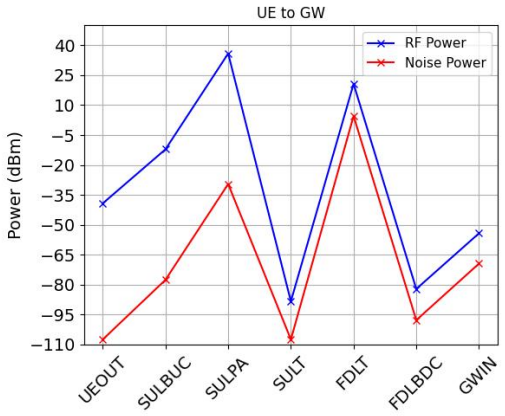

(b) UE to GW signal and noise power levels

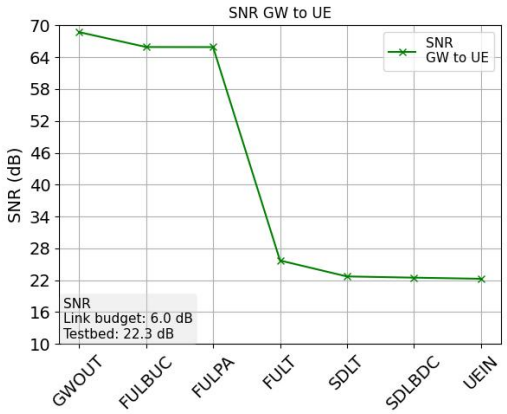

(c) GW to UE SNR

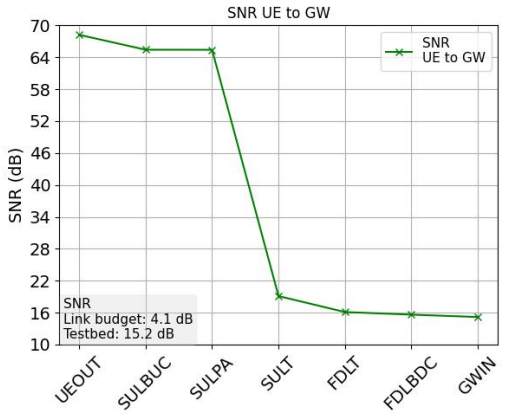

(d) UE to GW SNR

Figure 4.5: First 5G setup power levels and SNR in the first 5G test setup probe points. Please refer to Figure 4.4 node labels.

SNR at the transponder outputs: FULT–SDLT and SULT–FDLT. This is due to the noise figure of the transponders. Finally, at the outputs of the downlink attenuators (ATT FDL and ATT SDL), the SNR remains almost constant. This is the main issue of this setup: the noise at the BDCs inputs is mainly amplified thermal noise coming from the transponders. There is no control over the satellite downlink SNR after the transponders. Therefore, the only way to change the SNR at the far-end SDRs is by changing the testbed input power, which affects the output back-off of the ground power amplifier. The only way to achieve control would be to manually add noise before the far-end SDRs (or simply use channel emulators). However, the selected approach was to operate all components at the chosen back-off, despite the SNR being higher than in the link budget. The bit rate was evaluated using the Iperf3 tool. Figure 4.6 presents the achieved upload and download bit rates for the UE SDR. Based on this test, it can be concluded that the transponders do not introduce

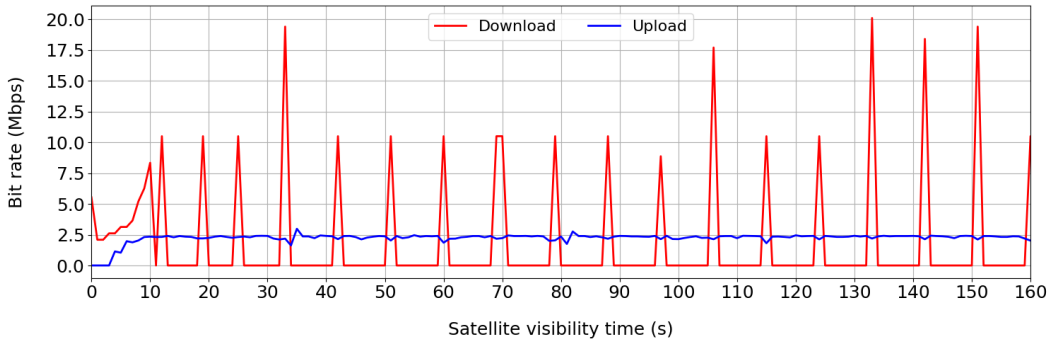

Figure 4.6: Achieved bit-rate during an emulated satellite passage measured at the UE side using the Iperf3 tool. The UE acts as the client, performing a standard upload test. The primary tested link is the uplink, which shows a consistent bit-rate. The observed download traffic corresponds to acknowledgments and control signaling generated by the connection.

significant impairments and can be integrated into the LIDE mission scenario.

4.2.2 5G NTN test setup 2

This second iteration of 5G NTN testing was performed in ESA ESTEC, Noordvijk, The Netherlands. Due to issues on the availability of laboratory equipment and PhD timeline, only the set up was completed, but, at the moment of writing of this document, no test has been performed. In the following, the test set up is presented. The block diagram of this testbed is shown in Figure 4.7.

The setup is similar to the one used in the one described in the previous section. BUCs and BDCs are laboratory equipment installed in a rack, as well as channel emulators. The used transponders are the same EQM used in the previous setup, interfaced to fixed attenuators. A testbed controller computer is used to monitor and control every component in the setup through a dedicated software that schedules a test procedure. Test devices are placed in two separate racks, as shown in Figure 4.8: one for channel emulators, SDRs, UE and gNB terminal; and another one for transponders, attenuators, BUCs, BDCs and power supply.

Each component in the testbed is connected to the laboratory ethernet network. For timing purposes, the testbed controller is a network time protocol (NTP) server for all the devices. Test procedures are written in Python and comprise an initial instrument setup, a main schedule of operations to be performed at precise timestamps, and a release schedule used to switch off instruments in a controlled way. Two separate machines are used for gNB and UE terminals; both integrate the Amarisoft software radio stack. The gNB Amarisoft terminal integrates also core network functionalities such as AMF and UPF. The satellite OBC is emulated on the same computer used for the gNB. This is implemented by connecting the computer to the transponder's interface boards via USB. The transponders accepts

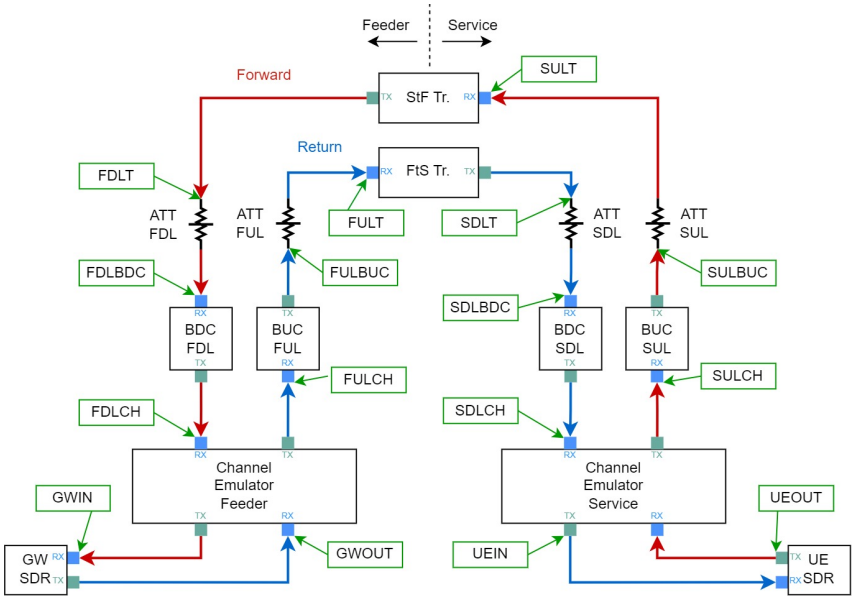

Figure 4.7: 5G NTN test setup 2.

string-based commands over an RS-422 interface. The transponder'ss interface boards serve as USB to RS422 converters. Each of the UE and gNB computers is connected to an Ettus X300 universal software radio peripheral (USRP) SDR. The X300 operates over a frequency range 0 GHz to 6 GHz and supports an instantaneous bandwidth of up to 120 MHz. This makes it suitable for operation in the 5G FR1 band, and also capable of generating baseband signals for FR2 channels with bandwidths up to 100 MHz. Both SDRs shares the same 10 MHz reference signal. It is provided by the high quality ESA ESTEC facility atomic clock and is forwarded by a reference distribution unit to SDRs, channel emulators and frequency converters on the testbed rack.

The used channel emulators are Squarepeg RLS-2100 radio link simulator. They feature 4 channel with instantaneous bandwidth up to 1200 MHz with operative frequency in the range 140 MHz to 2450 MHz. Latency, path loss and Doppler shift impairments can be added. The channel emulator features propagators for the computation of impairments that takes as input the terminal position on ground, fixed or mobile, and satellite position as state vector or from TLE. Some of the other available impairments are multipath fading, atmospheric effects, and blockage. Upconverter (BUC) and downconverter (BDC) to and from K/Ka band to the channel emulators operative frequency range are included in the setup, provided by Work Microwave.

The transponders can deliver up to 10 W saturated power in K/Ka band and need a very low input signal level, down to −90 dBm and up to −60 dBm. This operating level is wider than the one of the rest of the components in the rack. Therefore, fixed attenuation stages should be added in the testbed to prevent damage. Furthermore, the attenuation value

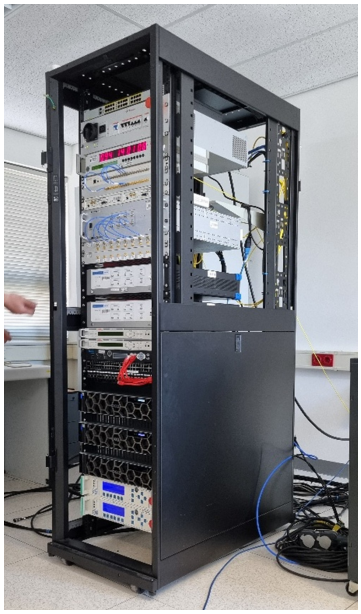

(a) Main rack

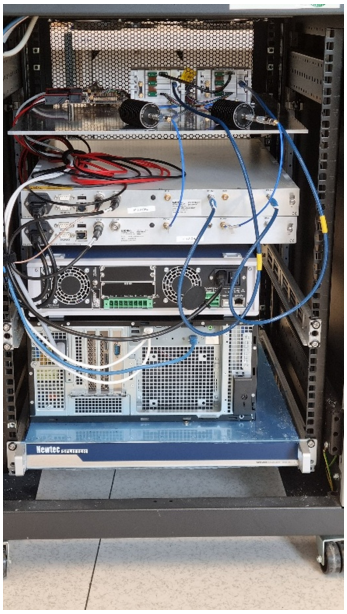

(b) Transponders rack

Figure 4.8: Pictures of the main rack, hosting channel emulators, SDRs, UE, gNB terminal and other equipment not related to this activity. On the right, the rack hosting transponders, BUCs, BDCs and power supply is shown.

should be known at channel emulator side, to compute the correct path loss and ensure that SDRs receives a signal with a SNR in line with the scenario to be emulated. Compression effects due to PAPR should be emulated only on the transponder. Other components in the testbed should be as much linear as possible.

The Amarisoft software radio stack of the gNB is integrated in one machine, along with the UPF. On another machine the UE simulator is integrated. Doppler and latency compensations are performed on service link by UE, based on SIB19 and UE position. On the same way, a similar pre-compensation is performed at gNB side from satellite TLE and gNB position.

Time windows of RACH procedure were adjusted according to the RTT. In this scenario, which involves a transparent, single satellite data relay, the RTT_{max} is computed as in 4.1 [66]. R_E is the Earth radius, h the satellite altitude and c the speed of light in vacuum. θ_{min} is the minimum elevation angle at which gNB and UE can transmit. This can be imposed by the scenario or by telecommunication regulations in the operative area.

$$RTT_{max} \approx \frac{2}{c}\left[\sqrt{(R_E+h)^2 - R_E^2\cos^2(\theta_{min})} - R_E\sin(\theta_{min})\right] \tag{4.1}$$

RAR window size is defined by gNB and tells the UE how much time to wait from Msg1 transmission to Msg2 reception. MAC contention resolution timer, in a similar way,

TLE field	**Line**	**Column**	**Value**
Satellite name	0	1–24	satellite name
Line 1 number	1	1	1
Satellite number	1	3–7	99954
Classification	1	8	U
International designator	1	10–11	25046A
Epoch	1	12–32	t_0 (test time origin)
1^{st} mean motion derivative	1	34–43	0
2^{nd} mean motion derivative	1	45–52	0
Drag term	1	54–61	0
Ephemeris type	1	63	0
Element set number	1	65–68	1
Checksum	1	69	Modulo 10 of Line 1
Line 2 number	2	1	2
Satellite number	2	3–7	99954
Inclination	2	9–16	i (4.9)
Right ascension	2	18–25	α (4.3)
Eccentricity	2	27–33	0
Perigee argument	2	35–42	0
Mean anomaly	2	44–51	M (4.4)
Mean motion	2	53–63	n (4.8)
Revolution at epoch	2	64–68	0
Checksum	2	69	Modulo 10 of Line 2

Table 4.1: TLE field mapping.

is related to Msg3 and Msg4. These timers were set both at 20 ms, which is higher than the maximum RTT combined with gNB processing time. The *timeAlignmentTimer* is used to control for how long the actual TA value is considered valid and when it should be updated. UE adjust its time alignment also through SIB19, but TA updates are necessary.*timeAlignmentTimer* should be higher than the maximum RTT, and enough frequent to maintain the time alignment. The chosen value, obtained empirically is 160 ms.

The testbed control procedure should specify a reference satellite TLE, which is provided to the channel emulator for impairment calculation and to the gNB for SIB19 broadcasting and proper feeder-link pre-compensation. Using a real satellite TLE is not feasible, as this would require each test to coincide with the actual satellite passing over the selected ground position. A straightforward solution would be to modify the time reference of all instruments in the testbed. However, manipulating the system clock of the test machine was considered cumbersome. To overcome this, a virtual TLE generator was developed. For each test, a TLE is generated dynamically based on the current time and the desired satellite passage characteristics. A summary of the TLE fields is shown in Table 4.1 and their calculation in the following.

The generator produces a TLE file from the following input parameters: satellite altitude h_s, satellite mass m_s, ground position $[g_{lat}, g_{lon}, g_{el}]$ (latitude, longitude, elevation), maxi-

mum elevation e_{max}, and minimum elevation e_{min} with respect to the ground station. The following approximations apply: spherical Earth model, null orbit eccentricity, null drag, and null mean motion derivatives. The virtual satellite corresponding to the generated TLE is at elevation e_{min} when the test starts. The TLE epoch is set at the test time origin t_0. The ascending node longitude AN_{lon} at t_0 is then computed. The ascending node is the origin of the equatorial coordinate system and is defined as the Sun location at the March equinox. At t_0, the Sun is located above $[0; AN_{lon}]$ in $[latitude; longitude]$ Earth coordinates. The calculation of AN_{lon} is shown in (4.2), with t_{ME} as the time epoch of the March equinox (20/03/2024 03:07 UTC), Δt_{ME}^{noon} as the time difference between t_{ME} and 12:00 UTC on the same day, and t_{syd} as the duration of a sidereal day:

$$AN_{lon} = \frac{t_0 - t_{ME}}{360 t_{syd}} + \frac{t_{ME} - \Delta t_{ME}^{noon}}{360 t_{syd}} \tag{4.2}$$

AN_{lon} is the sum of two terms: the first relates to Earth's rotation from t_{ME} to t_0, while the second is the longitude of the Sun at noon UTC on t_{ME}. Once AN_{lon} is known, the right ascension α and mean anomaly M TLE fields can be computed as in (4.3) and (4.4) from the ground station location. The offsets Δs_{lat}, Δs_{lon}, defined in (4.6) and (4.7), from (4.5), define the latitude/longitude displacement needed to obtain the desired satellite passage with the specified starting and maximum elevation. R_E is the Earth radius.

$$\alpha = g_{lon} + \Delta s_{lon} + AN_{lon} \tag{4.3}$$

$$M = g_{lat} + \Delta s_{lat} \tag{4.4}$$

$$l(\vartheta) = \tan^{-1}\left(\frac{1}{\tan\vartheta}\right) - \frac{\sin^{-1}\left(\frac{R_E + g_{el}}{R_E + h_s}\right)}{\sqrt{(\tan\vartheta)^2 + 1}} \tag{4.5}$$

$$\Delta s_{lon} = l(e_{max}) \tag{4.6}$$

$$\Delta s_{lat} = \sin^{-1}\left(\sqrt{\sin^2(l(e_{min})) - \sin^2(\Delta s_{lon})}\right) \tag{4.7}$$

The last parameters needed for the TLE generation are the satellite mean motion n and orbital inclination i. In (4.8), m_E and m_s denote Earth and satellite masses, respectively, and G is the universal gravitational constant.

$$n = \frac{t_{syd}}{2\pi}\sqrt{\frac{G(m_E + m_s)}{(R_E + h_s)^3}} \tag{4.8}$$

A slight orbital inclination i is added to the generated TLE to compensate for Earth's ro-

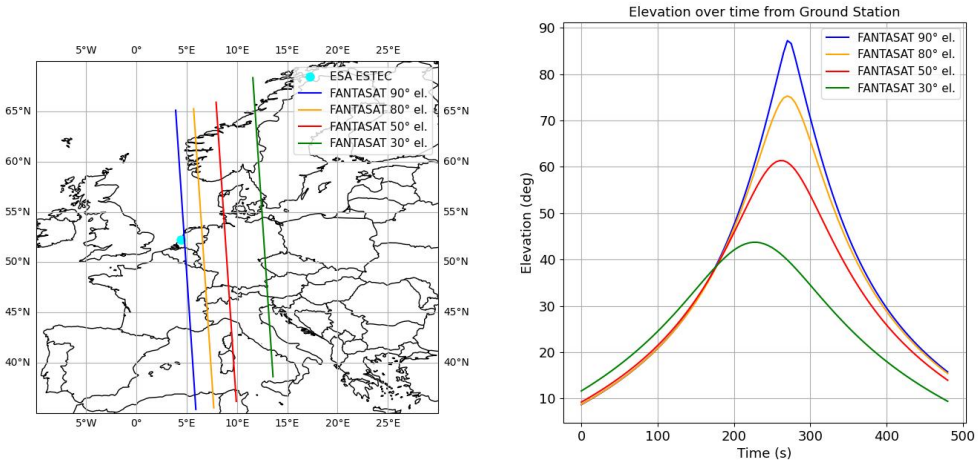

(a) Satellite footprint on ground

(b) Satellite elvation with respect to ESA ESTEC

Figure 4.9: TLE generator tested for different satellite maximum elevation. Satellite mass is 300 kg, its altitude is at 600 km and ground station is placed at ESA ESTEC, Noordvijk, The Netherlands.

tation during the satellite passage, as shown in (4.9) ensuring that the satellite ground track remains approximately parallel to the meridians. This assumption significantly simplifies the computations.

$$i = \cos^{-1}\left(-\frac{2\pi}{t_{syd}n}\right) \tag{4.9}$$

In Figure 4.9, the TLE generator is tested with four satellite passages at maximum elevations of 90°, 80°, 50°, and 30°. The satellite mass is set to 300 kg, and its altitude to 600 km. The ground station is located at ESA ESTEC, Noordwijk, The Netherlands. As observed, the maximum elevation is not reproduced with full accuracy, and the satellite ground track is not exactly parallel to the meridians. This could be a consequence of the simplified model. Nevertheless, the result is more than sufficient, as the TLE generator is only required to provide a reference satellite passage that can be replicated at different times.

In conclusion, this setup is ready to be used in ESA ESTEC but in stand-by at the moment of writing of this document. The 5G NTN test setup 1 was developed in the context of the LIDE activity, as a de-risking test to assess the compatibility of the space segment, with ground segment and 5G protocol deployment. 5G NTN test setup 2 was instead developed to serve as a in-lab reference scenario during LIDE in orbit demonstration, which are ongoing.

4.3 In-Orbit demonstration

The two IODs of *radiosat* and *beamsat* payload, and the LIDE IOD are presented in this section.

4.3.1 Radiosat and beamsat IOD

The *radiosat* and *beamsat* devices, as a payload, were integrated into a satellite carrier, which can point at a base station on ground actively, changing its attitude during the satellite passage. The satellite, still in orbit, is at 645 km of altitude in the LEO range. A ground station located in central Italy interfaced with the satellite during its orbital passes. The station, developed by a partner company, featured a dual-band, dual-polarization reflector antenna, frequency up/down converters, and a 10 W power amplifier for transmission.

The received power spectrum, for every transponder operative mode, are presented. As a final demonstration of the success of the mission, a photo of the earth acquired by the satellite camera was transmitted by the developed device using the Beacon modulated mode.

A series of in-orbit tests were performed during the mission's operational phase to evaluate system performance. These tests included:

- Check-alive: Transponder telemetry was queried to ensure all system parameters were within expected values in a non-operative phase.
- *radiosat* CW beacon reception: Reception of the CW beacon generated by *radiosat*.
- Transponder bent-pipe mode with CW transmission: Evaluation of the transponder's ability to relay a CW signal generated by the ground station.
- Transponder bent-pipe mode with QPSK transmission: Main operativity test, in which the ground station transmits a QPSK signal and receives it after the *radiosat* relay operation.
- Modulated beacon transmission: A predefined string was transmitted via the satellite transponder's modulated beacon in GFSK and received by the ground station.
- In-orbit firmware upload: An update of the *radiosat* firmware was fetched to the OBC through the telemetry and command (TT&C) link to the satellite, separated by the K/Ka link object of this work. The new firmware version was then flashed in the transponder memory and main functionalities were evaluated.
- Image transmission: Through the modulated beacon two photos of the earth were transmitted, which were captured by satellite camera during operations.

The initial check-alive tests were successful, with all telemetry parameters confirming nominal operation. No anomalies were detected throughout the test campaign. During the IOD, telemetry data were consistently monitored to ensure proper system functionality.

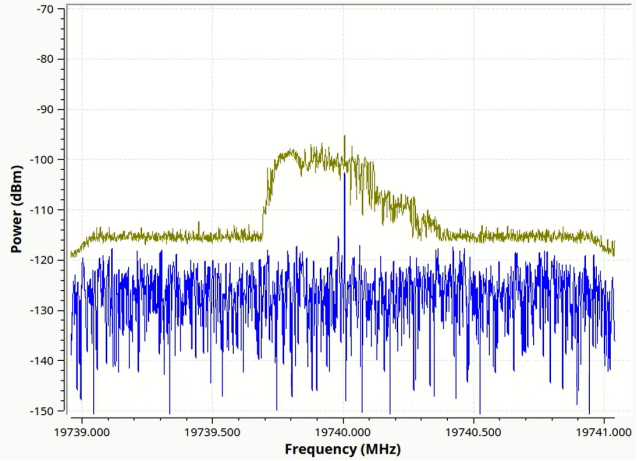

Figure 4.10: 19.74 GHz CW beacon test passage shown with the spectrum analyzer max-hold function. Doppler shift is not compensated. Test performed on 08/05/2024 with satellite maximum elevation at 38°

The first set of operational tests focused on CW beacon transmission. This test provided an initial assessment of the overall performance of both space and ground segments, as well as the pointing accuracy. The received signal is shown in Figure 4.10.

The second set of tests focused on the primary functionality of the transponder, which operates as a bent-pipe repeater. In this configuration, a signal generated by the ground station is transmitted to the satellite, relayed by the transponder, and received back by the same ground station. The test was conducted in two phases:

- Initially, the ground station transmitted a CW signal to facilitate a straightforward evaluation of the transponder's relay capability. This result is not shown here.
- Following multiple successful CW tests, the ground station began transmitting a modulated signal using QPSK.

The tests confirmed the proper operation of the transponder. However, signal loss was observed at high elevation angles. This is due to the high angular speed required for the ground station to follow the satellite, which led to a degradation of pointing accuracy. During the passage the transponder handled its gain through AGC. The spectrogram of the visibility and output spectrum is presented in Figure 4.11.

In this test and in the following ones, the ground station actively compensated for the Doppler effect induced by the satellite relative speed to the ground station.

During each test transponder telemetry was queried every 5 s by the OBC running in the satellite subsystems and managing Picosats transponder. Then, after each test, the telemetry, saved in a text file format, was downloaded using the S-band TT&C transceiver available on the satellite. The telemetry data collected included voltages, currents, temper-

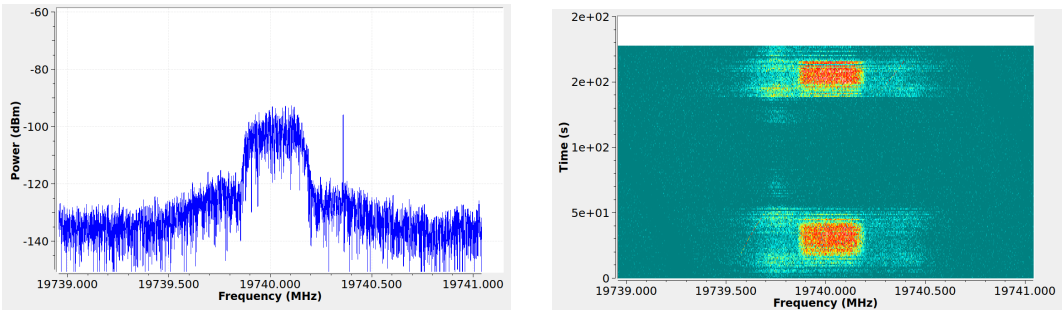

(a) Signal spectrum (b) Passage spectrogram

Figure 4.11: 19.74 GHz transponder mode test passage shown with the spectrum analyzer. Doppler shift is compensated. Test performed on 23/07/2024 with satellite maximum elevation at 59°. The ground station lost connection around maximum elevation, probably due to the required high angular scan rate.

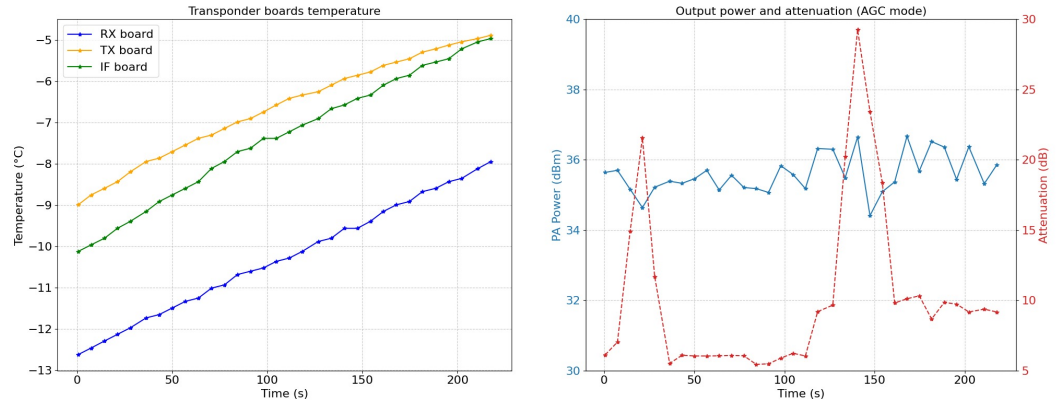

Figure 4.12: Transponder telemetry recorded during the test reported in Figure 4.11 on 23/07/2024.

atures and other parameters such as RF output power read through the detector, internal attenuation and frequency of operation. During some tests of the IOD the AGC was turned on. In Figure 4.12 temperatures telemetry (left) and AGC telemetry (right) during the same test reported in Figure 4.11 are shown.

Board temperature traces shows that the payload system was heating at around $0.02\,\mathrm{K\,s^{-1}}$. The transponder mass is 790 g and its power consumption was around 13 W all along the satellite passage. The estimated thermal capacitance is then $923\,\mathrm{J\,kg^{-1}\,K}$, which is in line with what was simulated by Picosats (not shown in this document). Regarding the temperature absolute value it is difficult to extract further information, since the satellite has an active temperature management system which ensures that the payload is always in the temperature range −30 °C to 70 °C. Satellite internal temperature information was not provided.

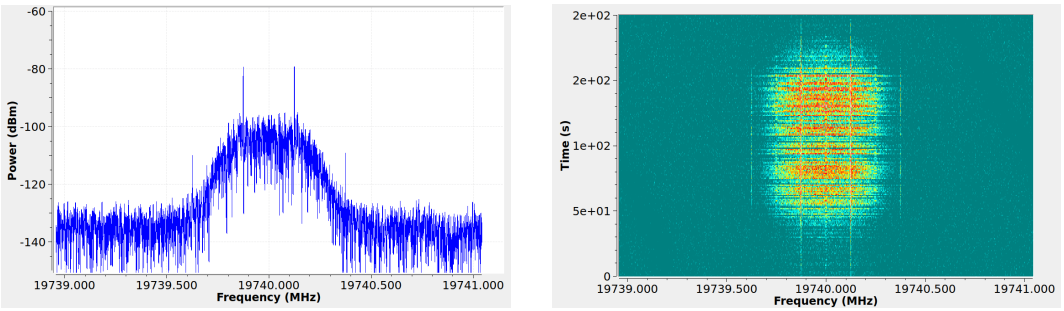

(a) Signal spectrum

(b) Passage spectrogram

Figure 4.13: 19.74 GHz GFSK mode test passage shown with the spectrum analyzer. Doppler shift is compensated. Test performed on 22/08/2024 with satellite maximum elevation at 48°.

Regarding the output power and internal attenuator value, the AGC algorithm clearly increases the attenuation when an incoming signal is detected. The attenuator value peaks in Figure 4.12 align with the spectrogram in Figure 4.11. On the other hand, the output power appears constant at the 35 dBm AGC set point throughout the satellite pass. This might seem unexpected, given that the ground station lost visibility during the pass. However, the attenuator reaches 30 dB upon signal reception, and the estimated SNR (based on Table 2.1) ranges from 24.0 dB to 30.0 dB for elevations between 20° to 59°. Since the estimated SNR falls within the observed attenuator variation, the 35 dBm output recorded during loss of visibility is likely just amplified noise. Therefore, the output power reading is considered accurate, and the AGC is working properly.

The final set of tests evaluated the transponder's modulated beacon. In this case, a GFSK modulated signal carrying the string "PICOSATS Radiosat&Beamsat – IOD 2023" was transmitted. The string was successfully received multiple times (results not shown here). The output spectrogram is presented in Figure 4.13.

Following the successful completion of previous tests, the transponder firmware was successfully updated in orbit. Rather than a standard test, this upgrade enabled the satellite payload to transmit an image of Earth via the modulated beacon. The photo was captured by the satellite camera.

To carry out this test, part of the transponder's software was rewritten to facilitate image transfer from the satellite to the transponder's memory, to segment the image into packets, and to transmit it to Earth using the modulated beacon mode. The test was performed twice, successfully receiving two images reported in Figure 4.14. The first image was unclear, while the second distinctly captured Italy.

The purpose of this IOD was to demonstrate the transponder and horn antenna compliance with the space environment. The presented results fully demonstrate the satellite telecommunication payload in transponder, CW beacon and modulated beacon modes. How-

Figure 4.14: Two images of earth captured by satellite camera and transmitted with GFSK transponder beacon. The first image captured on the left is unclear, but the one at the right is clearly shows the Italian peninsula.

ever, a comparison with K/Ka-band propagation experiments like [90] and [91] is difficult to make. Several uncertainties affect the ground station and satellite pointing, which were not under the control of the author of this thesis or Picosats in general. As far as the author's knowledge, a complete description of the in-orbit demonstration of a K/Ka-band satellite has not been presented in academic literature.

4.3.2 LIDE IOD

In this section, only the relevant tests conducted at the time of writing of this thesis are described. These tests were carried out to assess the operation of at least one transponder prior to the full deployment of the LIDE mission. A CW signal was transmitted from the ESA ESTEC ground station, relayed by one transponder in the satellite payload, and then received by the same ground station. The CFO of the entire system can be easily measured with this setup. Baseband data samples were recorded during the satellite passage on 25/09/2025 and subsequently processed to generate the plots shown below.

In Figure 4.15, the useful spectrogram of the satellite passage is shown. Unfortunately, the recording encountered issues shortly after the satellite rose above the horizon. The plot shown is therefore limited to the useful portion of the data. It can be observed that the CW signal was successfully detected on the ground.

The received signal was then compared to the predicted Doppler shift using the TLE of the LIDE satellite and the SGP4 propagator. The received signal frequency, the estimated Doppler, and the Doppler-compensated signal are shown in Figure 4.16. The Doppler-

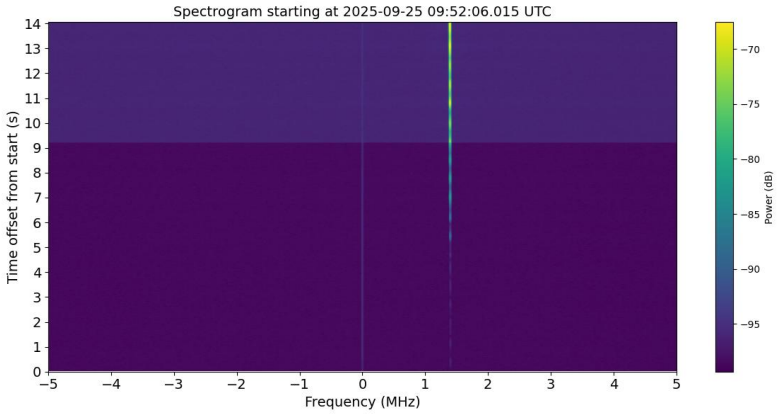

Figure 4.15: Spectrogram of the LIDE satellite passage on 25/09/2025 at ESA ESTEC. Only the useful portion of the data is shown due to recording issues.

compensated frequency error is significant, approximately 330 kHz. As can be seen in Figure 2.8, this frequency error is much larger than what could be caused by an unsynchronised payload over the entire round-trip path from the GW to the UE and back. Further investigations should be done.

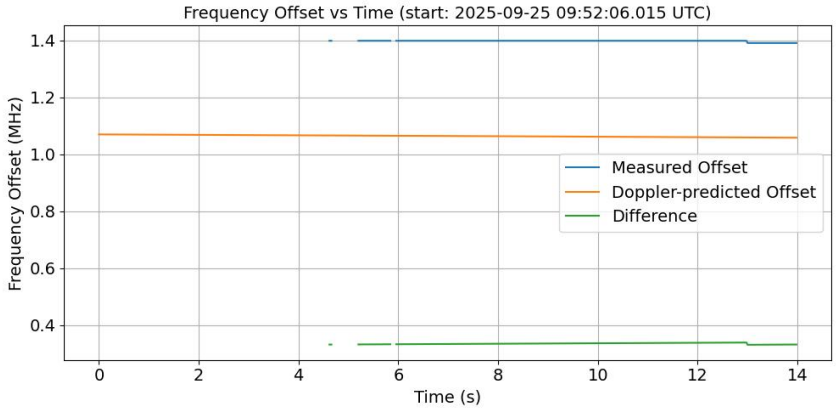

Figure 4.16: Frequency offset of the received signal on 25/09/2025, related to the spectrogram in Figure 4.15. The displayed traces are: measured at ground (blue), predicted Doppler shift (orange), and the difference between the two (green).

On 26/09/2025, another test was performed using the same setup. A 5G NR signal was generated with a signal generator, relayed by the satellite, and decoded using a spectrum analyzer. Doppler shift was not compensated in this case. At the point of maximum elevation, where Doppler shift is minimal, the 5G signal was successfully received and decoded, with a mean EVM of approximately 9.7%. This result is promising for the planned mission operations in the following months. A spectrum analyzer screenshot of the performed test

around maximum elevation is shown in Figure 4.17.

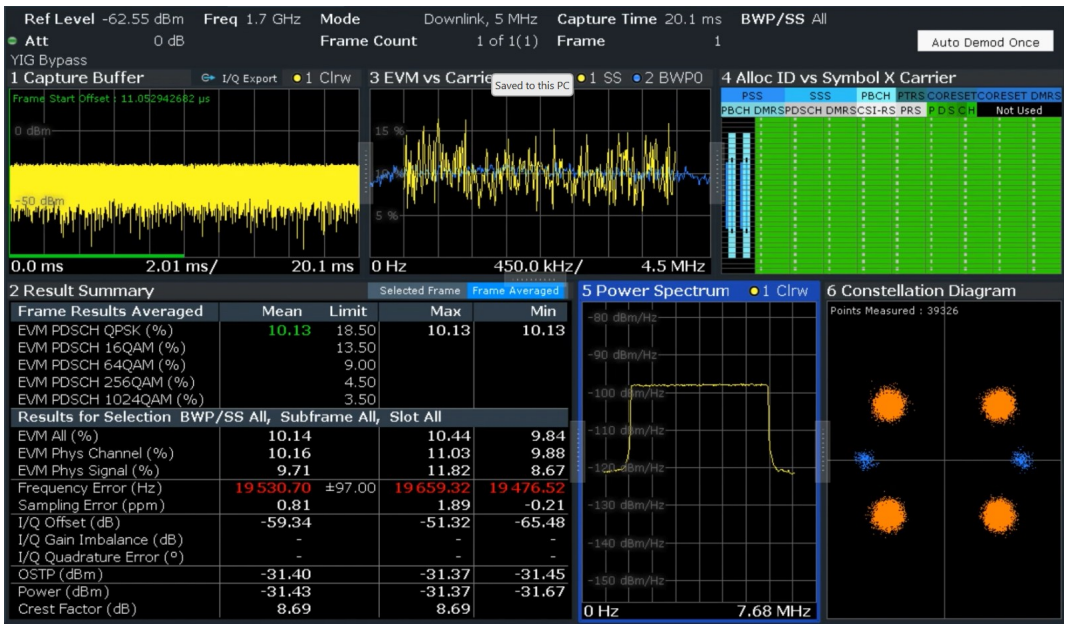

Figure 4.17: Spectrum analyzer screenshot of the satellite passage on 26/09/2025, in which a 5G NR signal was generated and relayed to the ground station. In this case, Doppler was not compensated.

Conclusions

In this work, transceiver technologies for 5G NTN were described, focusing in the context of LIDE mission and other activities from hardware design to system analysis and testbed implementation.

In initial chapters, the fundamental characteristics of satellite communications was presented, as well as the basics of the 5G NR protocol stack. This analysis led to the description of 5G NTN design challenges and standardization process. The work presented here revolves mainly around the 5G physical layer. In this context, the main issues are related to Doppler shift, latency, constrained terminals capabilities and higher layer issues related to the large propagation delay, such as HARQ.

The scenario in which this work was carried out is then described. The main activities are the IOD of a K/Ka band transponder with dual-band horn antenna, the LIDE mission and the improved design of the satellite transceiver. In the presented IOD a K/Ka-band transparent transponder *radiosat* and the dual-polarization, dual-band K/Ka horn antenna *beamsat* were validated in a LEO environment. LIDE mission involves a 12U satellite acting as a transparent data relay between a 5G UE and a gNB, which provides access to the core network. The satellite's uplink and downlink operate in the FSS K/Ka-band frequency range, while the 5G software radio stack used on the ground operates in the FR1 frequency range with NTN adaptations. A pair of transponders and four antennas operating in the K and Ka bands were designed as the mission payload. Link budgets and system analysis on PAPR and carrier frequency offset were presented. The transceiver systems presented in this work were described in terms of their architecture. The LIDE mission payload and space platform architecture and interfacing with the ground segment was described as well. The design of the transceiver up-converter and the receiver front-end were presented, focusing on the integration of the designed PCB with the metallic enclosure.

An upconverter architecture based on COTS componets for FSS LEO was proposed. The system is capable of covering the 17.3 GHz to 21.2 GHz FSS RF bandwidth with a variable IF frequency from 2.5 GHz to 4.0 GHz. Combined USB and LSB frequency conversion modes are used to increase SFDR, which was characterized using a modulated 100 MHz 16-QAM input signal. The presence of 3LO spur, however, degrades the SFDR for RF frequencies near 17.3 GHz and IF near 4.0 GHz. This drawback can be mitigated with LO-nulling and PLL

output power adjustment; for instance, at 3.2 GHz IF frequency, it is possible to increase the minimum SFDR on the RF band from 31 dBc to 48 dBc. A 10 W power amplifier, limited to the 17.3 GHz to 20.2 GHz band, was added and the overall spurious emission was compared with ITU recommendations. The system is compliant for all the RF bandwidth within IF band 2.5 GHz to 3.5 GHz and in the sub-band 17.8 GHz to 20.2 GHz for IF band 3.5 GHz to 4.0 GHz. As a final characterization EVM was measured. In the presented cases, EVM ranges between 3.41% and 6.75%.

As a final chapter, the testing of the presented devices and systems was presented. The qualification campaign of the payload was briefly described. In particula, two 5G-specific testing activities carried out during the PhD were described. The first one was related to the LIDE mission development and involved ground equipment as well. The results confirm that the designed payload is in line with the scenario even after qualification. Its compatibility with a 5G environment was further validated through the dedicated testbed. The achieved data rates are in line with LIDE requirements, reaching more than $1\,\mathrm{Mbit\,s^{-1}}$ for upload and $10\,\mathrm{Mbit\,s^{-1}}$ for download at the UE side. The second testing activity, carried out in ESA ESTEC, was mainly involving the satellite payload integration with the 5G protocol stack and related NTN adaptations. This activity is in standby and will be continued in November. The designed testbed will be used as an in-lab comparison for the LIDE IOD. During the PhD two IODs were successfully deployed by Picosats and the LIDE consortium. The Picosats IOD test results demonstrated the transponder's capability to generate both a CW beacon signal and a Gaussian Frequency Shift Keying (GFSK) modulated beacon. The primary bent-pipe transponder functionality was successfully validated, along with initial system health checks and in-orbit firmware programmability. During modulated beacon tests, a predefined string was transmitted and received multiple times. As a final test, two images of Earth were captured and successfully transmitted in multiple packets over several satellite passes, with one image clearly depicting Italy. The LIDE IOD is still ongoing; in this work the main outcomes available at the moment of writing of this document have been presented. In particular, a 5G NR link was implemented suing a signal generator, spectrum analyser, and a reduced LIDE mission setup. The payload is currently working properly, based on preliminary tests, and the full deployment of LIDE system will be performed soon.

The presented work gives a practical overview of the SATCOM ecosystem from 2022 to 2025, described through the author's activities carried out at Picosats srl. Based on the experimental and in-orbit evidence collected during this period, the research questions posed in the introduction can now be addressed.

The results demonstrate that COTS solutions can be successfully integrated into space telecommunication systems. As evidenced by the presented IODs, a reliable K/Ka-band system based on COTS components can survive and operate in the LEO environment. The LIDE experiments further link this capability to the 5G NTN scenario, proving that commercial hardware can meet the physical layer requirements of modern standards.

Regarding 5G NTN satellite systems, this study highlights that while transparent payloads offer reduced hardware complexity, they impose significant challenges on system integration, particularly regarding frequency and timing synchronization. Since the satellite acts as a "bent-pipe" relay without regenerative capabilities, impairments such as Doppler shift, delay, and SSPA must be compensated by the ground system. Furthermore, the feeder link compensations is outside current 3GPP specifications. The satellite payload should be as "transparent" as possible in terms of frequency accuracy and other impairments such as non-linearities introduced by the satellite power amplifier. Since the satellite does not implement other network layers apart from the physical layer, this type of compensation should be performed at the GW-gNB side through non-3GPP adaptations like the satellite TLE-based timing and PRACH frequency compensation proposed by the Amarisoft software radio stack. On the service link side, SIB19 and GNSS capabilities of the UE could help on the synchronization. In the case of the integration of the gNB in the satellite payload, the feeder link issues could be bypassed since the feeder link could be implemented with other point-to-point protocols like DVB-S2X. The GW could then be interfaced with 5GC functions and the DN. Several activities initiated during this PhD remain open. Above all, the LIDE IOD, which is currently yielding promising preliminary results, and the related 5G testbed designed at ESA ESTEC.

While this work focused on transparent solutions, recent trends, especially in the context of ESA IRIS2 and future 6G networks, show increased interest in gNBs integrated directly on satellites. While the question of whether to host 5GC some functions in orbit remains an open research topic, the transition towards regenerative payloads represents the next step towards more versatile and scalable NTNs.

Bibliography

[1] G. Schiavolini, G. Orecchini, F. Adamo, *et al.*, "Novel Architecture for Beacon Signal Generation in Satellite Applications," in *2023 IEEE/MTT-S International Microwave Symposium - IMS 2023*, 2023, pp. 815–818.

[2] F. Adamo, A. Loppi, S. Pauletto, F. Zanchetta, N. S. Gorella, I. Zebochin, F. Santarossa, G. Simoncini, G. Schiavolini, B. Valinoti, M. Fragiacomo, A. Gregorio, S. Carrato and C. Monti, "In-Orbit Demonstration of a Tansponder and Antenna for K/Ka Band SATCOM," in *Space Microwave Week, ESA ESTEC, Noordvijk, The Netherlands*, 2025.

[3] F. Parigi, L. Deva, S. Pauletto, F. Adamo, S. Perticaroli, A. Checih, R. Vallauri and A. Vicentini, "IOD Mission For Direct 5G Broadband Access From LEO," in *75th International Astronautical Congress (IAC)*, 2024.

[4] F. Adamo, S. Pauletto, N. S. Gorella, F. Zanchetta, A. Loppi, I. Zebochin, G. Simoncini, M. Fragiacomo, A. Gregorio and S. Carrato, "A K/Ka Band 5G Satellite Payload for LIDE Mission," in *55th European Microwave Conference (EuMC), Utrecht, The Netherlands*, 2025.

[5] F. Adamo, G. Simoncini, S. Pauletto, S. Carrato, and A. Gregorio, "Design of a 17.3-21.2 GHz SATCOM Upconverter Based on COTS with Low Spurious Emission," in *2025 IEEE Space Hardware and Radio Conference (SHaRC)*, 2025, pp. 12–15.

[6] ESA Space Debris Office, *ESA's Annual Space Environment Report*, version 8.0, Aug. 2024.

[7] Qorvo, "Satcom Market Overview: Cost Effective Solutions Needed to Address the Exponential SATCOM Market Growth," White paper.

[8] "SpaceX FALCON 9." (Jul. 2025), [Online]. Available: `https://www.spacex.com/vehicles/falcon-9/`.

[9] "From custom-made to commercial: how ESA is changing the way that spacecraft are built." (Jun. 2020), [Online]. Available: `https://www.esa.int/Enabling_Support/Preparing_for_the_Future/Discovery_and_Preparation/From_custom-made_to_commercial_how_ESA_is_changing_the_way_that_spacecraft_are_built`.

[10] R. Gomes, L. Sismeiro, C. Ribeiro, *et al.*, "Will COTS RF Front-Ends Really Cope With 5G Requirements at mmWave?" *IEEE Access*, vol. 6, pp. 38 745–38 769, 2018. DOI: 10.1109/ACCESS.2018.2851781.

[11] G. Maral and M. Bousquet, *Satellite Communications Systems: Systems, Techniques and Technology* (Wiley Series in Communication and Distributed Systems). Wiley, 1998.

[12] ITU, *Radio Regulations*, Article 5 - Frequency allocations, 2024.

[13] ITU, *Attenuation by atmospheric gases and related effects*, Recommendation ITU-R P.676-13, Aug. 2022.

[14] ITU, *Propagation data and prediction methods required for the design of Earth-space telecommunication systems*, Recommendation ITU-R P.618-14, Aug. 2023.

[15] ITU, *Prediction method of fade dynamics on Earth-space paths*, Recommendation ITU-R P.1623-1, Mar. 2005.

[16] F. Alimenti, P. Mezzanotte, G. Simoncini, *et al.*, "A Ka-Band Receiver Front-End With Noise Injection Calibration Circuit for CubeSats Inter-Satellite Links," *IEEE Access*, vol. 8, pp. 106 785–106 798, 2020.

[17] G. Orecchini, G. Schiavolini, P. Mezzanotte, *et al.*, "Low-Noise Ku-band Receiver Frontend with Switchable SIW filters for Cubesat Applications," in *2022 29th IEEE International Conference on Electronics, Circuits and Systems (ICECS)*, 2022, pp. 1–4. DOI: 10.1109/ICECS202256217.2022.9971113.

[18] L. Gao, Q. Ma, and G. M. Rebeiz, "A 20–44-GHz Image-Rejection Receiver With 75-dB Image-Rejection Ratio in 22-nm CMOS FD-SOI for 5G Applications," *IEEE Transactions on Microwave Theory and Techniques*, vol. 68, no. 7, pp. 2823–2832, 2020. DOI: 10.1109/TMTT.2020.2979441.

[19] M.-Y. Huang, T. Chi, S. Li, T.-Y. Huang, and H. Wang, "A 24.5–43.5-GHz Ultra-Compact CMOS Receiver Front End With Calibration-Free Instantaneous Full-Band Image Rejection for Multiband 5G Massive MIMO," *IEEE Journal of Solid-State Circuits*, vol. 55, no. 5, pp. 1177–1186, 2020. DOI: 10.1109/JSSC.2019.2959495.

[20] D. Chen, W. Wang, and T. Kwasniewski, "Design Considerations for a Direct RF Sampling Mixer," *IEEE Transactions on Circuits and Systems II: Express Briefs*, vol. 54, no. 11, pp. 934–938, 2007. DOI: 10.1109/TCSII.2007.902063.

[21] Analog Devices, *Quad, 16-Bit, 12 GSPS RF DAC with Wideband Channelizers*, 2025.

[22] Texas Instruments, *ADC12DJ5200RF 10.4GSPS Single-Channel or 5.2GSPS Dual-Channel, 12-bit, RFSampling Analog-to-Digital Converter (ADC)*, 2019.

[23] Y. Yi, D. Zhao, J. Zhang, *et al.*, "A 24–29.5-GHz Highly Linear Phased-Array Transceiver Front-End in 65-nm CMOS Supporting 800-MHz 64-QAM and 400-MHz 256-QAM for 5G New Radio," *IEEE Journal of Solid-State Circuits*, vol. 57, no. 9, pp. 2702–2718, 2022. DOI: 10.1109/JSSC.2022.3169588.

[24] M. Pashaeifar, L. C. N. de Vreede, and M. S. Alavi, "A Millimeter-Wave Mutual-Coupling-Resilient Double-Quadrature Transmitter for 5G Applications," *IEEE Journal of Solid-State Circuits*, vol. 56, no. 12, pp. 3784–3798, 2021. DOI: 10.1109/JSSC.2021.3111126.

[25] M. Ide, K. Yuasa, S. Kato, T. Tomura, K. Okada, and A. Shirane, "A 256-Element Phased-Array Relay Transceiver for 5G Network Using 24-GHz Wireless Power Transfer With Discrete ICs," *IEEE Microwave and Wireless Technology Letters*, vol. 34, no. 6, pp. 793–796, 2024. DOI: 10.1109/LMWT.2024.3395300.

[26] Y. Wang, R. Wu, J. Pang, *et al.*, "A 39-GHz 64-Element Phased-Array Transceiver With Built-In Phase and Amplitude Calibrations for Large-Array 5G NR in 65-nm CMOS," *IEEE Journal of Solid-State Circuits*, vol. 55, no. 5, pp. 1249–1269, 2020. DOI: 10.1109/JSSC.2020.2980509.

[27] N. Hosseinzadeh and A. Medi, "Wideband 5 W Ka-Band GaAs Power Amplifier," *IEEE Microwave and Wireless Components Letters*, vol. 26, no. 8, pp. 622–624, 2016. DOI: 10.1109/LMWC.2016.2587834.

[28] H. Tao, J. Wang, Y. Wang, *et al.*, "High-Power Ka/Ku Dual-Wideband GaN Power Amplifier With High Input Isolation and Transformer-Combined Load Design," *IEEE Microwave and Wireless Components Letters*, vol. 31, no. 1, pp. 49–51, 2021. DOI: 10.1109/LMWC.2020.3032569.

[29] C. Ramella, C. Florian, M. Del Rocìo Garcìa, I. Davies, M. Pirola, and P. Colantonio, "Development of a Space-Grade Ka-Band MMIC Power Amplifier in GaN/Si Technology for SAR Applications," *IEEE Transactions on Microwave Theory and Techniques*, vol. 73, no. 2, pp. 977–987, 2025. DOI: 10.1109/TMTT.2024.3443607.

[30] K. K. W. Low, S. Zihir, T. Kanar, and G. M. Rebeiz, "A 27–31-GHz 1024-Element Ka-Band SATCOM Phased-Array Transmitter With 49.5-dBW Peak EIRP, 1-dB AR, and ±70° Beam Scanning," *IEEE Transactions on Microwave Theory and Techniques*, vol. 70, no. 3, pp. 1757–1768, 2022. DOI: 10.1109/TMTT.2021.3139911.

[31] K. K. Wei Low, A. Nafe, S. Zihir, T. Kanar, and G. M. Rebeiz, "A Scalable Circularly-Polarized 256-Element Ka-Band Phased-Array SATCOM Transmitter with ±60° Beam Scanning and 34.5 dBW EIRP," in *2019 IEEE MTT-S International Microwave Symposium (IMS)*, 2019, pp. 1064–1067. DOI: 10.1109/MWSYM.2019.8701112.

[32] G. Gültepe, S. Zihir, T. Kanar, and G. M. Rebeiz, "A Dual-Polarized 1024-Element Ku-band SATCOM Transmit Phased-Array with ±70° Scan and 43.5 dBW EIRP," in *2020 IEEE/MTT-S International Microwave Symposium (IMS)*, 2020, pp. 837–840. DOI: 10.1109/IMS30576.2020.9223977.

[33] S. Wang and G. M. Rebeiz, "A 32-Element 28/39 GHz Dual-Band Dual-Beam 5G Phased-Array with 40 dBm EIRP and Simultaneous 64 QAM Operation," in *2022 IEEE/MTT-S International Microwave Symposium - IMS 2022*, 2022, pp. 940–942. DOI: 10.1109/IMS37962.2022.9865316.

[34] 3GPP, *Release 15 Description; Summary of Rel-15 Work Items*, TR 21.915, v. 15.0.0, Oct. 2019.

[35] 3GPP, *Release 16 Description; Summary of Rel-16 Work Items*, TR 21.916, v. 16.2.0, Jun. 2022.

[36] 3GPP, *Release 17 Description; Summary of Rel-17 Work Items*, TR 21.917, v. 17.0.1, Jan. 2023.

[37] 3GPP, *Release 18 Description; Summary of Rel-18 Work Items*, TR 21.918, v. 15.0.0, Apr. 2025.

[38] "3GPP Portal: Releases list." (Apr. 2025), [Online]. Available: https://portal.3gpp.org/#/55934-releases.

[39] W. C. et al., "5G-Advanced Toward 6G: Past, Present, and Future," *IEEE Journal on Selected Areas in Communications*, vol. 41, no. 6, pp. 1592–1619, 2023. DOI: 10.1109/JSAC.2023.3274037.

[40] A. Ghosh, A. Maeder, M. Baker, and D. Chandramouli, "5G Evolution: A View on 5G Cellular Technology Beyond 3GPP Release 15," *IEEE Access*, vol. 7, pp. 127 639–127 651, 2019.

[41] 3GPP, *System architecture for the 5G System (5GS)*, TS 23.501, v. 18.9.0, Mar. 2025.

[42] 3GPP, *3rd Generation Partnership Project; Technical Specification Group Radio Access Network; NR; NR and NG-RAN Overall Description; Stage 2*, TS 38.300, v. 18.5.0, Mar. 2025.

[43] F. Z. Yousaf, M. Bredel, S. Schaller, and F. Schneider, "NFV and SDN—Key Technology Enablers for 5G Networks," *IEEE Journal on Selected Areas in Communications*, vol. 35, no. 11, pp. 2468–2478, 2017.

[44] 3GPP, *NR; Medium Access Control (MAC) protocol specification*, TS 38.321, 18.5.0, Mar. 2025.

[45] 3GPP, *NR; Radio Link Control (RLC) protocol specification*, TS 38.322, 18.2.0, Dec. 2024.

[46] 3GPP, *NR; Packet Data Convergence Protocol (PDCP) specification*, TS 38.323, 18.5.0, Mar. 2025.

[47] 3GPP, *Evolved Universal Terrestrial Radio Access (E-UTRA) and NR; Service Data Adaptation Protocol (SDAP) specification*, TS 38.324, 18.0.0, Apr. 2024.

[48] 3GPP, *Non-Access-Stratum (NAS) protocol for 5G System (5GS); Stage 3*, TS 38.331, 18.10.0, Mar. 2025.

[49] 3GPP, *NR; Physical channels and modulations*, TR 38.211, v. 18.5.1, Jan. 2025.

[50] M. S. J. G. Proakis, *Digital Communications*, McGraw-Hill, Ed. 2008.

[51] 3GPP, *NR; User Equipment (UE) radio transmission and reception; Part 1: Range 1 Standalone*, TS 38.101-1, 18.9.0, Apr. 2025.

[52] 3GPP, *NR; User Equipment (UE) radio transmission and reception; Part 5: Satellite access Radio Frequency (RF) and performance requirements*, TS 38.101-5, 18.9.0, Mar. 2025.

[53] 3GPP, *NR; Base Station (BS) radio transmission and reception*, TS 38.104, 18.9.0, Mar. 2025.

[54] 3GPP, *NR; Physical layer procedures for data*, TS 38.214, 18.6.0, Mar. 2025.

[55] 3GPP, *NR; Physical layer procedures for control*, TS 38.213, 18.6.0, Mar. 2025.

[56] 3GPP, *Study on New Radio (NR) to support non-terrestrial networks*, TR 38.811, V15.4.0, October 2020, 2020.

[57] X. Lin, S. Rommer, S. Euler, E. A. Yavuz, and R. S. Karlsson, "5G from Space: An Overview of 3GPP Non-Terrestrial Networks," *IEEE Communications Standards Magazine*, vol. 5, no. 4, pp. 147–153, 2021.

[58] T. Darwish, G. K. Kurt, H. Yanikomeroglu, M. Bellemare, and G. Lamontagne, "LEO Satellites in 5G and Beyond Networks: A Review From a Standardization Perspective," *IEEE Access*, vol. 10, pp. 35 040–35 060, 2022. DOI: 10.1109/ACCESS.2022.3162243.

[59] M. M. Azari, S. Solanki, S. Chatzinotas, *et al.*, "Evolution of Non-Terrestrial Networks From 5G to 6G: A Survey," *IEEE Communications Surveys & Tutorials*, vol. 24, no. 4, pp. 2633–2672, 2022.

[60] A. Guidotti, A. Vanelli-Coralli, M. Conti, *et al.*, "Architectures and Key Technical Challenges for 5G Systems Incorporating Satellites," *IEEE Transactions on Vehicular Technology*, vol. 68, no. 3, pp. 2624–2639, 2019.

[61] 3GPP, *NR; Radio Resource Control (RRC); Protocol specification*, TS 38.331, 18.5.1, Mar. 2025.

[62] A. Guidotti, A. Vanelli-Coralli, M. Caus, *et al.*, "Satellite-enabled LTE systems in LEO constellations," in *2017 IEEE International Conference on Communications Workshops (ICC Workshops)*, 2017, pp. 876–881.

[63] 3GPP, *Solutions for NR to support non-terrestrial networks (NTN)*, TR 38.821, V16.0.0, January 2020, 2020.

[64] P.-D. Arapoglou, S. Cioni, E. Re, and A. Ginesi, "Direct Access to 5G New Radio User Equipment from NGSO Satellites in Millimeter Waves," in *2020 10th Advanced Satellite Multimedia Systems Conference and the 16th Signal Processing for Space Communications Workshop (ASMS/SPSC)*, 2020, pp. 1–8.

[65] O. Kodheli, A. Guidotti, and A. Vanelli-Coralli, "Integration of Satellites in 5G through LEO Constellations," in *GLOBECOM 2017 - 2017 IEEE Global Communications Conference*, 2017, pp. 1–6.

[66] S. Kumar, C. K. Sheemar, J. Querol, *et al.*, "5G NTN LEO based demonstrator using OpenAirInterface5G," vol. 2023, pp. 69–75, 2023.

[67] F. Völk, R. T. Schwarz, and A. Knopp, "In-Lab Performance Analysis of a 5G Non-Terrestrial Network using OpenAirInterface," in *2023 IEEE International Conference on Wireless for Space and Extreme Environments (WiSEE)*, 2023, pp. 167–172.

[68] C. V. Nahum, L. De Nóvoa Martins Pinto, V. B. Tavares, *et al.*, "Testbed for 5G Connected Artificial Intelligence on Virtualized Networks," *IEEE Access*, vol. 8, pp. 223 202–223 213, 2020.

[69] M. Minardi, Y. Drif, T. X. Vu, I. Maity, C. Politis, and S. Chatzinotas, "SDN-based Testbed for Emerging Use Cases in Beyond 5G NTN-Terrestrial Networks," in *NOMS 2023-2023 IEEE/IFIP Network Operations and Management Symposium*, 2023, pp. 1–6.

[70] "ESA ARTES 5G: Demonstration of Direct 5G Broadband Access from LEO to Small Aperture Terminals." (Jan. 2025), [Online]. Available: `https://connectivity.esa.int/projects/esa-artes-5g`.

[71] "Satellite ready to test link for global 5G-broadband." (Jul. 2025), [Online]. Available: `https://www.esa.int/Applications/Connectivity_and_Secure_Communications/Satellite_ready_to_test_link_for_global_5G-broadband`.

[72] M. Hasna and M.-S. Alouini, "Performance analysis of two-hop relayed transmissions over Rayleigh fading channels," in *Proceedings IEEE 56th Vehicular Technology Conference*, vol. 4, 2002, 1992–1996 vol.4. DOI: `10.1109/VETECF.2002.1040567`.

[73] S. Gökceli, T. Levanen, T. Riihonen, M. Renfors, and M. Valkama, "Frequency-Selective PAPR Reduction for OFDM," *IEEE Transactions on Vehicular Technology*, vol. 68, no. 6, pp. 6167–6171, 2019. DOI: `10.1109/TVT.2019.2909643`.

[74] A. F. Almutairi, M. Al-Gharabally, and A. Krishna, "Performance Analysis of Hybrid Peak to Average Power Ratio Reduction Techniques in 5G UFMC Systems," *IEEE Access*, vol. 7, pp. 80 651–80 660, 2019. DOI: `10.1109/ACCESS.2019.2916937`.

[75] G. George, S. Roy, S. Raghunandan, C. Rohde, and T. Heyn, "5G New Radio in Nonlinear Satellite Downlink: A Physical Layer Comparison with DVB-S2X," in *2021 IEEE 4th 5G World Forum (5GWF)*, 2021, pp. 499–504.

[76] B. F. Beidas and R. Iyer Seshadri, "OFDM-Like Signaling for Broadband Satellite Applications: Analysis and Advanced Compensation," *IEEE Transactions on Communications*, vol. 65, no. 10, pp. 4433–4445, 2017.

[77] C. Ciochina, F. Buda, and H. Sari, "An Analysis of OFDM Peak Power Reduction Techniques for WiMAX Systems," in *2006 IEEE International Conference on Communications*, vol. 10, 2006, pp. 4676–4681.

[78] 3GPP, *NR; User Equipment (UE) conformance specification; Radio transmission and reception; Part 5: Satellite access Radio Frequency (RF) and performance*, TS 38.521-5, 18.6.0, Jul. 2025.

[79] P. Moose, "A technique for orthogonal frequency division multiplexing frequency offset correction," *IEEE Transactions on Communications*, vol. 42, no. 10, pp. 2908–2914, 1994. DOI: 10.1109/26.328961.

[80] J.-C. S. Chieh, E. Yeo, R. Farkouh, *et al.*, "Development of Flat Panel Active Phased Array Antennas Using 5G Silicon RFICs at Ku- and Ka-Bands," *IEEE Access*, vol. 8, pp. 192 669–192 681, 2020.

[81] J. Yoo and S. Hong, "A 28 GHz RF-DAC With Analog LO Leakage Cancellation," *IEEE Transactions on Circuits and Systems II: Express Briefs*, vol. 69, no. 11, pp. 4308–4312, 2022. DOI: 10.1109/TCSII.2022.3186013.

[82] M.-H. Wu, J.-H. Tsai, and T.-W. Huang, "Ka-Band Calibration-Free High Image-Rejection Up/Down Mixers With 117% Fractional IF Bandwidth for SATCOM Applications," *IEEE Access*, vol. 8, pp. 182 133–182 145, 2020. DOI: 10.1109/ACCESS.2020.3028238.

[83] L. Gao, Q. Ma, and G. M. Rebeiz, "A 20–44-GHz Image-Rejection Receiver With ¿75-dB Image-Rejection Ratio in 22-nm CMOS FD-SOI for 5G Applications," *IEEE Transactions on Microwave Theory and Techniques*, vol. 68, no. 7, pp. 2823–2832, 2020. DOI: 10.1109/TMTT.2020.2979441.

[84] ITU, *ITU Radio Regulations, APPENDIX 3 (REV.WRC-12), Maximum permitted power levels for unwanted emissions in the spurious domain*, 2020.

[85] ITU, *Rec. ITU-R SM.1541-6, Unwanted emissions in the out-of-band domain*, 2015.

[86] ITU, *Rec. ITU-R SM.329-12, Unwanted emissions in the spurious domain*, 2012.

[87] G. Orecchini, G. Schiavolini, P. Mezzanotte, *et al.*, "Low-Noise Block Downconverter based on COTS and SIW Filters for Ku-band Cubesat Transponders," in *2023 IEEE Space Hardware and Radio Conference*, 2023, pp. 1–4. DOI: 10.1109/SHaRC56958.2023.10046247.

[88] S. C. Cripps, *RF Power Amplifiers for Wireless Communication*, 2nd ed. Norwood, MA: Artech House, 2006.

[89] ECSS Secretariat, ESA-ESTEC, Requirements & Standards Division, *ECSS-E-HB-10-02A – Verification guidelines*, 2010.

[90] T. Kostulski and S. Reisenfeld, "Ka band Propagation Experiments on the Australian Low-Earth Orbit Microsatellite " FedSat "," in *2005 Australian Communications Theory Workshop*, 2005, pp. 102–106. DOI: 10.1109/AUSCTW.2005.1624234.

[91] F. Cuervo, A. M. Polegre, D. Vanhoenacker-Janvier, J. Flávio, and M. Schmidt, "The Q/W-band CubeSat LEO Propagation Experiment," in *2021 15th European Conference on Antennas and Propagation (EuCAP)*, 2021, pp. 1–5. DOI: 10.23919/EuCAP51087.2021.9411255.

La borsa di dottorato è stata cofinanziata con risorse dell'Unione europea-*NextGeneration EU*
Piano Nazionale di Ripresa e Resilienza (PNRR)